Radical Concentration and Temperature Measurements in Sooting Flames by Cavity Ring-Down Spectroscopy and Laser-Induced Fluorescence

A thesis submitted for the degree of Doctor of Philosophy

By

Yuxuan Hu

Department of Chemical and Process Engineering

Faculty of Engineering

University of Strathclyde, United Kingdom

May, 2015

DECLARATION OF ORIGINALITY

This thesis is the result of the author's original research. It has been composed by the author and has not been previously submitted for examination which has led to the award of a degree.

Name.....

Signed .....

Date.....

Abstract

Sooting laminar flames at atmospheric pressure present a very complex chemical environment with numerous sources of interference for optical measurement techniques. Absolute concentration profiles of $^1CH_2$ and HCO have been measured under a range of flame conditions in a sooting laminar premixed C_2H_4-air flat-flame by Cavity-Ring Down Spectroscopy performed at wavelengths in the range 615 to 625 nm. Also, concentration profiles of the OH radical have been detected via the band of $A^2\sum(v'=0) \leftarrow X^2\prod(v''=0)$ system by Laser-Induced Fluorescence and quantitatively calibrated by Cavity-Ring Down Spectroscopy. In situ measurements of these radicals in sooting flames have hitherto been lacking and are essential for validation of chemical kinetic models of aromatic hydrocarbon and soot formation in flames. The experimental results are compared to simulated concentration profiles generated using the Appel-Bockhorn-Frenklach mechanism. Temperature profiles obtained using OH LIF thermometry are used in interpreting the CRDS data and as input for flame simulation. Additionally, weak broadband absorption is observed by CRDS in the region between the reaction zone and the onset of soot formation; this may be attributable to low concentrations of large aromatic species.

Acknowledgments

I would like to express profound gratitude to my supervisor, Dr. Iain Burns, for his invaluable support, encouragement, supervision and useful suggestions during the production of this thesis. His moral support and continuous guidance enabled me to complete my study successfully. I am also highly thankful to Dr. Jaclyn Dunn who I have spent wonderful time with in the same research group for three years. I must also thank various members of staff who have contributed to this work. I wish them all the best.

I am as ever, indebted to my parents, Mr. Shengxiong Hu and Mrs. Fengjun Zhang for their love and support throughout my life.

Finally, special thanks go to my wife Ms. Zhi Jing who is supporting me to finish this thesis and taking care of me during these years. Also, this thesis is special for you my dear son Mr. Jingyi Hu.

Contents:

List of Figures:

List of Tables:

CHAPTER 1: INTRODUCTION

1.1 Background

The combustion of hydrocarbon fuels is still the globally dominating source of energy for industry and transportation. The conversion of chemical energy via combustion remains essential to modern civilization as a source of heat, light, and propulsion. However, with the development of human civilization and rapidly increasing of demand for energy, combustion is also the main source of anthropogenic air pollution: oxides of nitrogen and sulfur, carbon dioxide, incompletely burned hydrocarbons, and combustion-generated carbonaceous nanoparticulates (also called soot). In order to both satisfy the increasing energy demand and minimize the effects of man-made air pollutants, combustion technology has to be improved substantially. According to pragmatic engineering concepts, combustion pollutant emissions could be reduced by several methods such as adjusting the conditions of combustion, selecting low-nitrogen and low-sulfur fuels, pre-treating fuels, post-treating combustion gases and so on. However, the improvement by these methods is very limited. In addition, a purely empirical approach to engineering design is very costly. This cost can be reduced when

the consequences of different designs can be simulated by computer and for this purpose the simulation must be as accurate as possible. To achieve this the understanding has to be built up using experiments performed under simplified geometries with well-controlled boundary conditions. Modern combustion research is focusing on scientific basis, a better understanding of the chemical mechanisms of combustion would be the only way to fulfil this goal (Aldén et al., 2011, Glassman and Yetter, 2008, Warnatz et al., 2006).

Some knowledge of chemical mechanisms and kinetics concerning hydrocarbon combustion has existed for a number of decades and lots of studies have been performed to investigate them in detail. Due to the chemical complexity, very short timescale and inconvenient chemical analysis, the mechanisms underlying hydrocarbon combustion are still not fully understood. According to previous studies (Kohse-Höinghaus et al., 2005, Wang, 2011), correct prediction of pollutant formation is particularly dependent on the chemistry of minor species. For example, soot is considered as one of the main pollutants in combustion. Soot particle dynamics models which describe the evolution of particle ensemble are significantly influenced by the accuracy of the species profiles supplied by the gas-phase submodels. The chemistry of minor species plays a key role in these submodels. Therefore, it is necessary to measure

intermediate species concentration profiles to validate detailed combustion mechanisms by comparing model predictions to experimental data (Mehta et al., 2009, Miller et al., 2005, LAW, 2005, Appel et al., 2000).

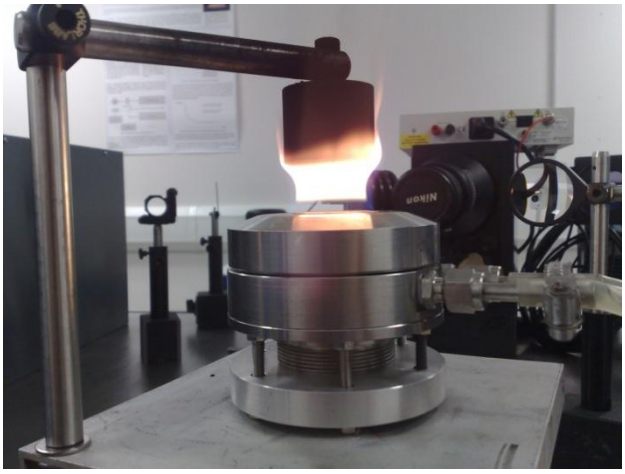

Figure 1.1: Photograph of the flame. (The soot emission (orange region) is clearly visible.)

Environmental considerations and combustion efficiency are currently the key motivations for most of combustion-related diagnostics research and development (Cheskis and Goldman, 2009). Specific diagnostic measurement strategies are required to meet the requirements of laboratory experiments as well as industrial test rigs. Laminar flames are widely used to study detailed chemical reaction mechanisms (Cheskis and Goldman, 2009). These flames are often considered to be at steady state

so that detection of important atomic, molecular species and carbonaceous soot can be performed sequentially (Cheskis and Goldman, 2009, Warnatz et al., 2006). Flat-flame burner produces an approximately flat reaction zone, and therefore can be considered as a one-dimensional process to a good approximation (Glassman and Yetter, 2008). The flame shown in Figure 1.1 that was used in this work is a premixed ethylene/air-flame on a flat flame burner consisting of a water-cooled porous plate. Detailed profiles of the flame temperature as well as species concentrations must be measured in flames in order to have a better understanding of the kinetics of this combustion process.

1.2 Laminar premixed sooting flames

1.2.1 Background of laminar premixed flame

In this sub-section, an introduction of premixed flat flame is presented, so that experimental research challenges and opportunities for the development of the laser based techniques can be estimated. The premixed laminar flat flame is widely employed by combustion scientists due to its simplest combustion type which can provide understanding of the fundamentals of combustion. Figure 1.2 provides a typical

sectional view of the flat flame burner while Figure 1.3 shows how some important physical parameters vary with height above the burner surface. As shown in the Figure 1.3, a thin flamefront is formed s short distance above the burner.

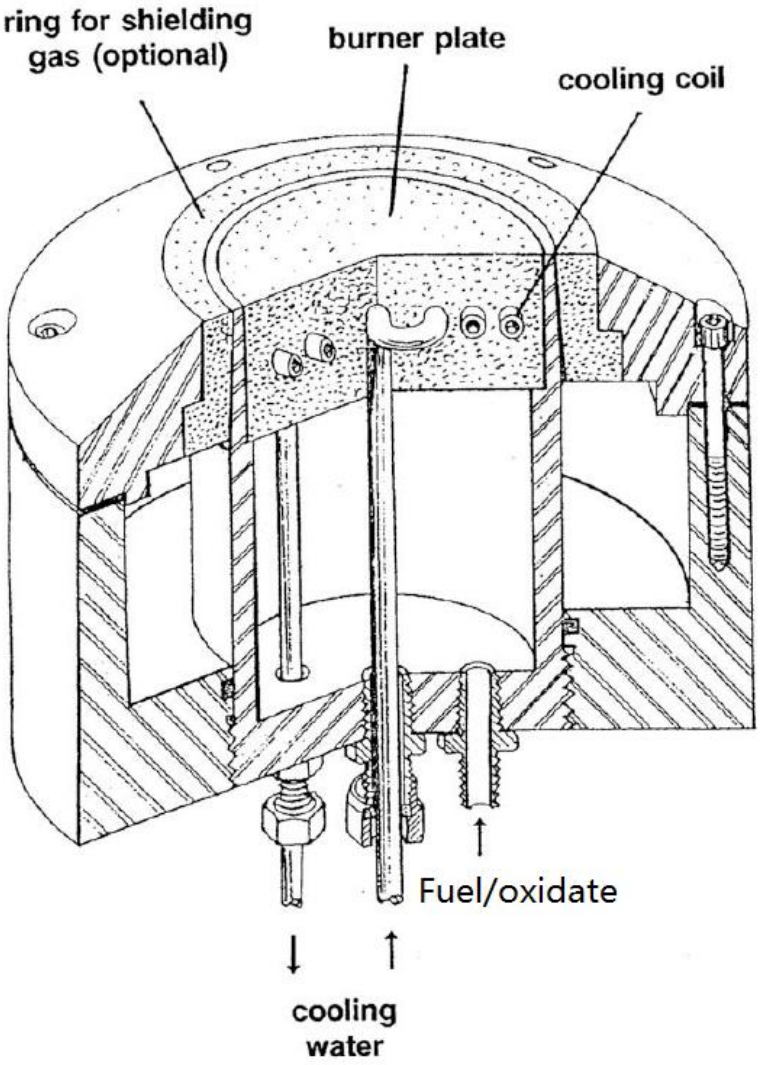

Figure 1.2: Sectional view of the flat flame burner (Mckenna Products). *(This figure has been copied from (Prucker et al., 1994)).*

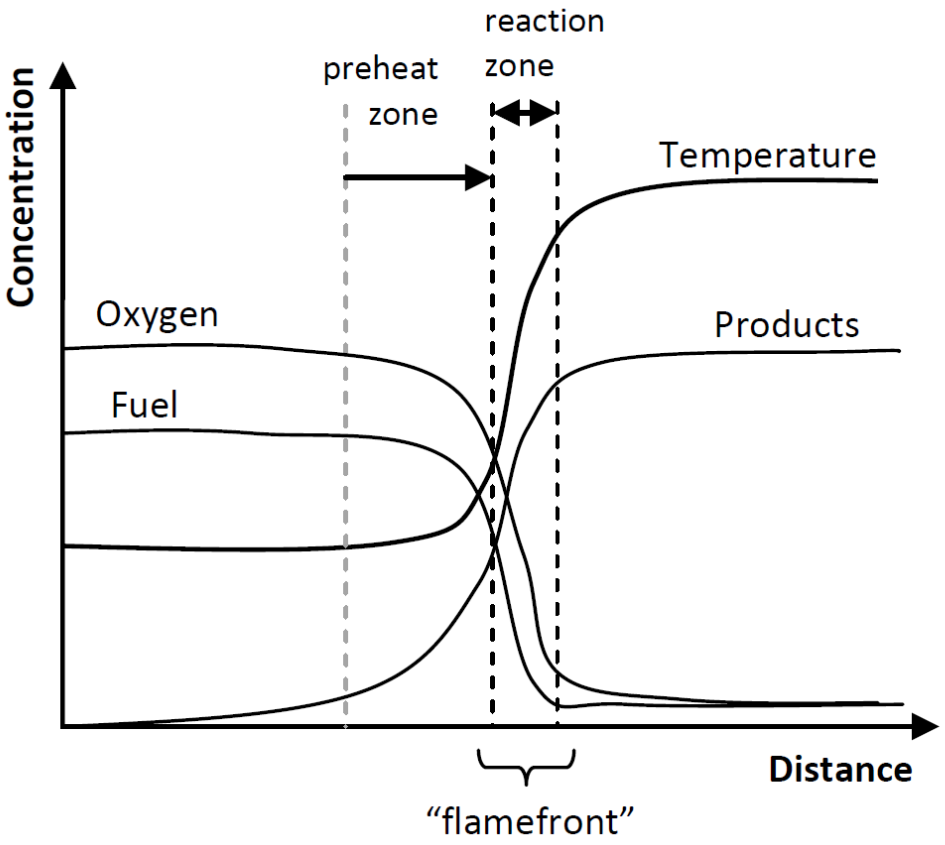

Figure 1.3: Profiles of temperature and concentration of major species across a flamefront for a typical premixed flame. *(This figure has been copied from (Warnatz et al., 2006)).*

Fuel and air are premixed and then supplied and burnt above the porous plug. There is a relatively cool zone immediately downstream of the water-cooled porous medium. This zone is called preheat zone. The endothermic pyrolysis of the hydrocarbon fuel to smaller intermediates occurs in this zone (Turns, 1996). The majority of the heat in

flames is released by the exothermic reactions of these intermediates a little further downstream in the reaction zone. This region is very narrow since the reactions are very rapid. This effect can be shown by the steep temperature gradient. Most of molecular reactions take place in preheat and reaction zones. There are no standard flame thickness and no clear distinction between these two zones. Different fuels and conditions of mixing alter the flamefront significantly (Warnatz et al., 2006). The chemical complexity of this region supplies lot of research interests and challenges, and it is believed that better simulations of pollutant formation can benefit from the better understanding of gas phase chemistry in this region.

1.2.2 Research interests of laminar premixed sooting flames

The main purpose of the experimental investigation in this type of flame is to achieve a more comprehensive and reliable description of the combustion process. The mathematical description of these flames is basis for numerical simulation. The simulation is an increasingly important tool for improving combustor design and performance, because it has the capability of prediction of combustion properties such as temperature, composition and flow velocities (Miller et al., 2005, Poinsot and

Veynante, 2001, Borman and Ragland, 1998). The greatest benefits of this ability are time- and cost-savings, because it can offer a powerful tool to design and manufacture combustion equipment without requirement of prototypes fabrication and tests (Borman and Ragland, 1998, Frenklach, 2002). However, the accuracy and reliability of the simulation have been limited by many factors till now. Hundreds of chemical reactions are occurring in flames at the same time. The complexity of computational modelling is magnified by these reactions, because they add much more degrees of freedom into the calculation (Spalding, 1956, Dixon-Lewis, 1970, Veynante and Vervisch, 2002, Fogler, 2006, Singh et al., 2006, Wang, 2011). Therefore, the requirement of improving combustion models and mechanisms gives us preliminarily experimental research guidelines. On one hand, combustion experiments can be designed to compare specific results with research hypothesis in order to test ideas about chemical reactions or combustion physics. On the other hand, validation of a detailed combustion simulation can also be achieved by the comparison between experimental and simulated results. Combustion simulations are often designed to obtain approximate solutions in an acceptable time. In order to achieve this purpose, some of factors have been neglected or replaced by simplified terms in the modelled equation sets. The factors which may be safely left out or replaced are based on how little they

contribute to the features of interest. This knowledge/experience is usually obtained by the validation procedure (Warnatz et al., 2006).

The models with chemical reaction mechanisms predict need to be critically tested against experimental results. These tests usually focus on the velocity, temperature and concentrations of species (Appel et al., 2000, Mehta et al., 2009, Hoyermann et al., 2004, D'Anna and Kent, 2003). The combustion models were improved by the technique of intrusive probe measurements in the past (Hirschfelder et al., 1953, Warnatz, 1978a, Warnatz, 1978b, Kee et al., 1980, Peters and Warnatz, 1982, Kee et al., 1985, Kee et al., 1989). However, with more improvement of the models, more detailed understanding of reaction mechanisms/fundamental combustion physics and chemistry is required, and thus more advanced experiments are essential to achieve this purpose. In order to explain how factors affect the models, let us consider the key equations.

As shown in Figure 1.3, the steep temperature gradients within the flame result from the strongly exothermic nature of the reactions. According to chemical reaction principles, lots of heat will be released if the molecules overcome their activation energies. The heat induces the rapid temperature increment. At the same time, the

chemical reaction rate coefficient shown in Equation 1.1 depends strongly on the flame temperature profile. Here, k is the rate coefficient of the reaction, E_a is activation energy, AT^b is a temperature dependent pre-exponential factor, R is the universal gas constant, T is the temperature. Therefore, the combination of the exothermic effect with exponential temperature dependence of reaction rate coefficient causes the temperature sensitivity of flame performance as well as simulations.

$$k = AT^b exp\ (-\frac{E_a}{RT}) \tag{1.1}$$

The concentrations of many species in flames are therefore extremely sensitive to the flame temperature profile. For example, the approximate percentages of NO_x production by the nitrous oxide, Zeldovich, and prompt mechanisms vary from 65:25:10 at 1650 K to 35:50:15 at 1850 K (Steele et al., 1995).

1.2.3 Laminar premixed flames modelling

Efforts in modelling laminar premixed flames with realistic reaction kinetics date back to the early 1950's. The first attempt to solve the governing equations of a laminar

premixed flame was offered by Hirschfelder et al (Hirschfelder et al., 1953) in order to obtain species and temperature profiles. Spalding (Spalding, 1956) introduced the use of finite difference methods. He solved the governing equations of a steady state adiabatic flame. Most subsequent treatments of the problem have used some variation of Spalding's method. A number of general purpose computer codes for modelling laminar premixed flames have been developed (Dixon-Lewis, 1967, Dixon-Lewis, 1970, Warnatz, 1984, Kee et al., 1985, Peters and Warnatz, 1982). The Sandia burner code (Peters and Warnatz, 1982, Kee et al., 1985) has been widely distributed and used. The program interfaces with the CHEMKIN subroutine library (Kee et al., 1980).

Laminar premixed flames are investigated through computer modelling. The Cantera (Goodwin) program is a widely use code for the modelling of the chemical kinetics. Cantera models the flame using similar physical principles as the earlier Sandia code. The program models the axial diffusion of heat and species as well as chemical kinetic processes. The NASA thermo-chemical polynomials (Burcat and McBride, 1993) are widely used to calculate the specific enthalpy (h), specific entropy (s), and specific heat (C_p) for the related species. These parameters are required for the laminar flame model which employs this thermo-chemical database together with multi-component transport libraries, measured temperatures, reactant molar flow rates, and a chemical

mechanism involving C-H-O-N reactions. The thermo-chemical and transport properties, required by the flame code for calculation of the species concentration profiles, are provided by a thermodynamic property database and a transport property database, both provided by GRI co-workers (Smith et al., 1999).

According to previous topical reviews (Wang, 2011, Miller et al., 2005), soot formation in flames is particularly related to polycyclic aromatic compounds (PAHs). And correct prediction of the PAHs is dependent on the chemistry of intermediate species. Therefore, it is necessary to obtain intermediate species profiles to process detailed combustion mechanisms in sooting flames. In this work, HCO and $^1CH_2$ were chosen as the targets because they are playing key roles in the process of PAHs formation which will be described in detail in Chapter 2. The hydroxyl radical (OH) was also chosen as a target species due to its sensitive-indicator and soot oxidation characters in combustion process (Wang, 2011, Smith et al., 1999). Moreover, OH fluorescence spectra can be used to obtain profiles of flame temperature in regions of the flame where it is sufficiently abundant.

1.3 Thermometry and Detection of Radical Intermediates

1.3.1 Thermometry

The determination of flame temperature profiles is important since it provides input data for analysis of data obtained by other optical diagnostic techniques and for flame simulation. Not only is temperature required as input data for flame simulation, but the quantitative evaluation of gas concentration from optical diagnostics also requires knowledge of temperature. The temperature profiles used as input for flame modelling affect the predicted species concentration distribution appreciably (Mehta et al., 2009, LAW, 2005). On the other hand, some temperature related properties like partition function and energy level distribution function influence the results of measurement quantification.

Physical temperature probes such as thermocouples are still the most widely applied methods (Kuo, 2005, Chigier, 1991). However, these techniques have many disadvantages that restrict their applications in combustion research. For example, the intrusive nature of probes can lead to flow perturbations and measurement errors, and

probes are subject to low spatial resolution due to its size limitation (Chigier, 1991). Therefore, the use of thermocouples in this study was considered to be inappropriate.

The hydroxyl (OH) radical is abundant in all hydrocarbon flames and is involved in many combustion reactions. It is often used for thermometry in flames. Owing to strong signals, the Laser-induced fluorescence (LIF) technique has been shown as a suitable method for OH measurements by Daily (Daily, 1976) and Cattolica (Cattolica, 1981). One of the most widely used non-intrusive techniques for accurate thermometry in flame studies is OH laser-induced fluorescence, as it has high accuracy (Comeau et al., 1989a) and uses the same laser system and similar exciting wavelength as the radical concentration measurement. Theoretically, OH LIF thermometry in flames is a well-developed technique—scanning excitation thermometry or also called Boltzmann plot method (Laurendeau, 1988) in this study. This method is on the basis of measurement of the population of lower lying energy levels. By calculating population distribution of these energy levels, local flames temperature can be deduced. According to this method, OH LIF signals are considered to simply depend on the local flame temperature and species concentrations. Examples can found in some studies (Cheskis and Goldman, 2009, Kohse-Höinghaus et al., 2005, Eckbreth, 1996, Kohse-Höinghaus, 1994). However,

most of these studies were done at sub-atmospheric pressure or lean flames. In this work, we demonstrated a detailed OH profiles measurement in highly sooting flames.

1.3.2 Radicals of Interest

Efforts to develop detailed kinetic mechanisms for prediction of PAHs have been intensively made in recent years (Wang and Frenklach, 1997b, Frenklach, 2002, Richter and Howard, 2000, Appel et al., 2000). Most of these work started from a detailed mechanism of Wang and Frenklach (Wang and Frenklach, 1997b). And then, ABF mechanism (Appel et al., 2000) provided an updated model especially for laminar premixed flames of C_2 hydrocarbons. Their description of the small hydrocarbon reactions is founded on GRI-Mech 1.2 (Frenklach et al., 1995). In addition, it includes revised gas-phase reactions, the formation of higher linear hydrocarbons up to C_6 species, and the formation of benzene and further reactions leading to pyrene. Moreover, it also consists of aromatic chemistry, soot particle coagulation, soot particle aggregation, and soot surface growth. Correctness of the model needs to be validated by experimental measurements in sooting flames.

Some important C_1 species concentration profiles (HCO and $^1CH_2$) play a key role in the gas-phase chemistry (Schocker et al., 2003) which will be described in detail in the next section and affect the formation of higher hydrocarbons. However, these gas-phase zone models were mostly validated in non-sooting flames, while the chemistry of richer flames in which soot is formed may be different from the non-sooting flames in which measurements have been made previously, and a relatively limited set of in situ measurements of these radicals is available even for non-sooting flames. Our focus radicals in sooting flames are HCO and $^1CH_2$ that will be described in details in Chapter 6. In general, studies of HCO (Lozovsky et al., 1997, Lozovsky et al., 1998b, Scherer and Rakestraw, 1997) were performed before in low and atmospheric pressure methane/oxygen flames to obtain its concentration profiles. More recently, Schocker et al (Schocker et al., 2005) have reported HCO detection in higher hydrocarbon fuel and rich flames under low pressure conditions. However, there is no measurement of HCO at sooting flames. As for $^1CH_2$, during the past decade, many studies have been focusing on the $^1CH_2$ measurement by absorption techniques. Cavity-Ring Down Spectroscopy (CRDS) was firstly applied in McIlroy work (McIlroy, 1999a, McIlroy, 1998) to quantitatively detect $^1CH_2$ concentration profile in low pressure flames. Later on, Evertsen et al (Evertsen et al., 2003a) utilized the absorption cross sections from Derzy et al (Derzy et al., 1999) to obtain the quantitatively concentration profile in

atmospheric flames by CRDS as well. More recently, Schocker et al (Schocker et al., 2005) made a further step to probe successfully in rich flames. However, there are neither HCO nor $^1CH_2$ study in sooting flame reported to date. Theretofore, our work is focusing on absolute concentration profiles of these two radicals at atmospheric laminar sooting flames in order to predict combustion behaviour in conjunction with simulations.

1.4 Laser Diagnostic Techniques

The previous sub-section discussed the interesting radicals briefly. There are many techniques to detect radicals in combustion. However, laser-based techniques have demonstrated lots of advantages over other experimental methods in combustion studies (Cheskis and Goldman, 2009, Schocker et al., 2005, Kohse-Höinghaus et al., 2005, Berden et al., 2000, Eckbreth, 1996, Kohse-Höinghaus, 1994, Aldén et al., 2011). Although well-developed physical probes are available for chemical reaction studies, few of them can be adapted to combustion processes. The most widely applied physical-probing methods are thermocouples and gas-sampling probes. These techniques have advantages, including simple implementation, well-developed

technology, and relatively low cost, but physical probes might critically influence combustion processes thermally, physically or catalytically (Kohse-Höinghaus, 1994, Aldén et al., 2011, Daily, 1997), because flames are gaseous and very easily perturbed. The sharp spatial gradients in temperature and concentration also present difficulties and the probe can conduct heat from the flame, quench radicals and influence the flow pattern. Reactions occurring in the sampling line are also a problem. These effects would make combustion behaviour totally different. Moreover, both spatial resolution and temporal response limit physical probes to practicability, spatial and temporal precision. Although thermocouples, when bare, can be extremely fine, their applicability is generally restricted to relatively benign flames. In the presence of particles e.g., fuel droplets and soot, they must be protected and, as a result, their spatial resolution is reduced, their temporal response diminished and their accuracy degraded (Chigier, 1991). In addition, physical probes cannot perform measurements in situ, and a correction process with introduced errors is necessary. This process makes physical probes more imprecision. A thermocouple, for example, measures its own temperature, not the charge temperature. Radiation, convection and conduction corrections have to be made to obtain accurate charge temperature measurement and these vary depending on the environment of the measurement (Vanmaaren et al., 1994). Another typical example is gas sampling probes which are used in combustion

studies sometimes. Great care must be taken to avoid chemical transformation at the sampling orifice and in the lines to the detection equipment because this method usually measure chemical composition far removed from the sampling location (Aldén et al., 2011, Eckbreth, 1996).

Optical diagnostic techniques involve the interaction of electromagnetic radiation with the atoms and molecules present in a flame and therefore avoid many of the disadvantages of physical probes. The techniques are remote so that they are almost always non-perturbing. Temperatures and species concentrations can be obtained by laser optical techniques with favourable spatial and temporal resolution. Furthermore, these methods can achieve in situ measurements at the exact point of interest within a very short timescale, so they can be employed to diagnose non-equilibrium phenomena. Nevertheless, laser techniques are not perfect. Due to physical diversity of atoms, molecules and particles, no one technique can perform all the required measurements. Several complicated experimental approaches might have to be combined together to measure concentrations of several species as well as temperature (Cheskis and Goldman, 2009, Kohse-Höinghaus et al., 2005, Kohse-Hoinghaus et al., 2005, Eckbreth, 1996). Fortunately, there are many techniques existing to meet different requirements including laser-induced fluorescence (LIF) (Daily, 1997), laser-induced incandescence

(LII) (Santoro and Shaddix, 2002), absorption, cavity ringdown spectroscopy (CRDS) (Berden and Engeln, 2009), intracavity laser absorption spectroscopy (ICLAS) (Pakhomycheva et al., 1970), degenerate four-wave mixing (DFWN) (Ewart and O'Leary, 1986), laser induced thermal grating spectroscopy (LITGS) (Williams et al., 1994), polarization spectroscopy (PS) (Nyholm et al., 1993) coherent anti-Stokes Raman scattering (CARS) (Tolles et al., 1977), Raman and Rayleigh scattering (Young, 1982, Long and Long, 1977, Bergmann et al., 1998). In this thesis, we concentrate on LIF and CRDS for measurement of radical concentration and temperature in sooting flames. The selection procedure of LIF and CRDS over other techniques for the purpose will be discussed in detail in the next chapter.

Laser-induced fluorescence (LIF) is regarded as one of the most sensitive non-intrusive detection techniques of all analytical methods (Eckbreth, 1996). This method has a number of attributes especially useful for providing concentrations and temperatures profiles (through the population distribution over internal energy levels) of identifiable molecular species in combustion studies. The successful examples cover many different applications, such as OH LIF thermometry (Daily, 1997). The laser is generally focused and pulsed in LIF application, so that high spatial and temporal resolutions are achievable. Sample volumes of $< 10^{-3}$ mm^3 are possible, although 1 mm^3 is a more

typically used value in many applications (Kohse-Höinghaus, 1994). Many of the lasers used have pulse lengths of 10 ns (Chigier, 1991), so that measurements average only over this interval. These characters may play important roles in atmospheric pressure flames, due to the exits of significant concentration and temperature gradients over spatial regions of the order of 1 mm (Mercier et al., 1999b). The technique is sensitive; for instance, OH can be detected in 1 mm^3 volume at sub-part-per-billion concentrations, producing some 100 detected photons on a single 10 ns laser shot (Dreyer et al., 2001). Selectivity is obtained through the narrow bandwidth of the laser, which provides high spectral resolution (Daily, 1997). A large number of reports are available about thermometry with LIF in lean or low-pressure combustion studies. However, in the presence of PAHs and soot, LIF becomes more challenging. The unknown quenching cross-sections, chemical complexity and signal interference make sooting flames a challenging environment for LIF measurement. Therefore, reference calibration of LIF measurements is necessary in sooting flames (Mercier et al., 1999b).

Cavity Ring Down Spectroscopy (CRDS) was developed by O'Keefe and Deacon (Okeefe and Deacon, 1988) and has been applied in combustion studies widely after that. According to previous studies (Schocker et al., 2005, Mercier et al., 2005, Schocker et al., 2003, Moreau et al., 2003, Evertsen et al., 2003b, Luque et al., 2002, Dreyer et al., 2001,

Mercier et al., 1999b, Scherer and Rakestraw, 1997, Scherer et al., 1997, Daily, 1997), it is a good method to obtain absolute concentration of species. Extremely sensitive measurements can be achieved using this method, allowing the measurement of very small differences in the amount of absorbed light. This technique is widely employed to measure the precursor species in order to model PAHs and particle formation in flames (Zalicki and Zare, 1995, Lozovsky et al., 1997, Scherer et al., 1997, Scherer and Rakestraw, 1997, McIlroy, 1998, Evertsen et al., 1999, McIlroy, 1999b, Mercier et al., 1999b, Berden et al., 2000, Atakan et al., 2003, Evertsen et al., 2003b, Moreau et al., 2003, Kohse-Höinghaus et al., 2005, Mercier et al., 2005). However, all of these investigations were performed in non-sooting flames, whereas the detection of intermediate species in more complex sooting environments is scare. In this work sooting, laminar, premixed, flat atmospheric flames were studied by LIF and CRDS in order to obtain temperature and concentration profiles of two key radicals (HCO and $^1CH_2$).

1.5 Motivations and Objectives

A major objective of the research described in this thesis has been to use Cavity Ring-Down Spectroscopy (CRDS) to measure concentration profiles of HCO and $^1CH_2$ under a range of flame conditions in a sooting laminar premixed C_2H_4-air flat-flame. Another component of the research involved the use of Laser Induced Fluorescence (LIF) to measure hydroxyl radical profiles as well as obtaining temperature measurements in regions where the signal-to-noise ratio was adequate. These are challenging objectives in sooting flames due to the intense luminosity, soot incandescence and PAHs fluorescence, low radical concentrations, attenuation of the incident beam and signal trapping. The results contribute to growing dataset recorded in this flame together with LII and PAHs LIF measurements being performed in our lab. The results presented here will support the development and validation of models to predict PAHs and particle formation in order to reduce combustion exhaust pollution.

1.6 Thesis overview

This thesis is organized as follows. Chapter 2 begins with a short background review of molecular spectroscopy and optical diagnostics in combustion research, and then introduces the theory of laser-induced fluorescence and cavity-ring down spectroscopy and analyses the required supplementary theory for the applications in atmospheric sooting laminar premixed flat flames. Also, the background of combustion modelling and requirement of the modelling validation illustrated the importance of this experimental work. Moreover, more specific topics related to this work are discussed in detailed including the both experimental and modelling literature review of premixed flat flames as well as their research interests and challenges.

Chapter 3 describes the experimental apparatus and operations procedures that should be observed when performing the measurements in sooting flames. Chapter 4 discusses the results of the OH LIF concentration and temperature measurements and the calibration procedures. Chapter 5 discusses the quantitative CRDS measurements and the calibration and quantitative calculation procedures including OH, $^{1}CH_2$ and HCO concentration measurements. Chapter 5 describes shortly how a numerical modelling

of premixed laminar flames is formed. This background is essential to lead to the discussion of the difference of chemical reaction mechanisms as well as the importance of their validation. And then, temperature profiles and the measured concentration profiles are compared with simulated results. The last chapter presents the most important conclusions and recommendations of this thesis.

CHAPTER 2: BACKGROUND KNOWLEDGE OF COMBUSTION AND LASER DIAGNOSTICS

2.1 Overview

This Chapter presents a relevant literature review in five sections. The first section describes a short background of what the combustion modelling is and the importance of experimental work in combustion modelling validation. The second and third sections review the background of molecular spectroscopy and the status and applications of optical diagnostics in combustion studies. The fourth and fifth sections are focused on the laser-induced fluorescence and cavity-ring down spectroscopy techniques, their past & current researches and the novelty of this experimental work.

2.2 Importance of experimental work in combustion research

2.2.1 Background

The importance of reducing particulate emissions has been established in the previous chapter. It is clear that laboratory experiments on combustion rig with simplified boundary conditions are essential to gain a better understanding of the mechanisms of soot formation and that laser diagnostics have unique advantages for probing such systems. Some aspects of combustion research (Glassman and Yetter, 2008, Warnatz et al., 2006, Kuo, 2005) focus on fluid mechanics and describe chemical reactions in terms of global heat release. In this way, the description does not take account of the reaction rate of the chemical phenomena in combustion, and assumes infinitely fast chemical reactions (Poinsot and Veynante, 2001, Lackner et al., 2010). This approach is widely used (Turns, 1996, Borman and Ragland, 1998) to design macroscopic combustion equipments such as furnaces and engines. This approach is insufficient to describe transient processes such as ignition, quenching and pollutant formation. It is because the reactions involved in pollutant formation are quite slow, so they are not infinitely fast compared to turbulence timescales and the assumption about Damköhler number is not valid (Fogler, 2006). However, we have established in the previous chapter that

understanding of pollutant formation mechanisms is essential to minimise harmful particulate emissions from combustion processes. To do this requires the coupling of detailed chemical reaction mechanisms with simulations of fluid flow. In order to better understand this research purpose, we review the fundamental description of combustion process with regards to the work presented in this thesis.

2.2.2 Fundamental knowledge of combustion modelling

An early mathematical description of flames was proposed by Hirschfelder et al (Hirschfelder et al., 1954) to treat combustion processes. The key variables to mathematically describe a combustion process consist of pressure, density, temperature, velocity of the flow and concentration of each species. These properties may be changing with positions and time. These changes are the result of fluid flow, chemical reaction, molecular transport and radiation (Hirschfelder et al., 1954). When forming the mathematical description of a flame, the changes of key conserved properties (energy, mass, and momentum) and chemical reactions in reacting flows are the general starting point.

The formation of mathematical description of combustion processes is the first step of the modelling. Three sets of conservation equations of momentum, energy and mass balances are often used as the starting point (Warnatz et al., 2006). The equation set of momentum balances is also known as Navier-Stokes. This time-dependent model describes the effect of the fluid motion, and need to calculate the three components of velocity over the entire spatial domain. Besides, Navier-Stokes is related to the equation set of energy balances due to its dependence on density and viscosity. The reason can be explained by temperature dependent factors. These factors are density, viscosity and thermal conductivity which determine the properties of the gaseous mixture. The output of the energy equation (temperature) significantly affects these factors above. Therefore, Navier-Stokes is coupled to the energy equation. As known in the brief of combustion chemistry, the temperature is also dependent on the rate of chemical reaction, which is contained in the conservation equation set of mass balance for all the species modelled participating in the chemical reactions. According to these equation sets and their relationship, it seems to be a perfect model to mathematically describe the combustion processes without any other assumptions. However, the requirement of a tremendous amount of computational power appears when solving this model, especially in the mass balance equations, because there are nearly 40 elementary reactions and hundreds of species for a satisfactory chemical mechanism

even in the simplest combustion process of hydrogen and oxygen (LAW, 2005, Smith et al., 1999). In many practical cases of hydrocarbons combustion processes, several thousands of reactions and tens of thousands species exist (Wang, 2011, UCSD, Babushok and Tsang, 2004).

2.2.3 Combustion modelling validation

Therefore, many efforts have been made to overcome the computational limitations. Nowadays, the widespread method is to simplify the physics and chemistry of combustion. In order to achieve the target, simplification of the set of chemical reactions was proposed (Miller et al., 2005). Modelling of some intermediates involved in the reaction pathways was neglected. The most benefit of this method is much less computation required for the conservation equation set of mass balance. In addition, another common simplification applied to the mass balances is the replacement of multi-component diffusion coefficients with binary ones. However, this assumption has to be carefully reviewed when apply to models, because the simplification of multi-component diffusion may neglect counter diffusion effects for light molecules (Kadowaki and Hasegawa, 2005). The typical example is hydrogen atoms in flames due

to the Soret effect (Kadowaki and Hasegawa, 2005). In addition, the Dufour effect is responsible for inducing diffusion of heat by the presence of concentration gradients. Both the Soret and Dufour effects are often neglected in practically computational models (Veynante and Vervisch, 2002).

In order to verify whether the modelling approach described above and the chemical reaction mechanisms presently available provide satisfactory predictions, a comparison between the outputs and experimental results needs to be performed. Therefore, accurate diagnostics is required in order to obtain necessarily experimental results. In the next section, the background knowledge of measurement methods will be discussed in detail with regards to the work presented in this thesis.

2.3 Molecular spectroscopy background

Molecular spectroscopy is defined as the use of the absorption, emission, or scattering of electromagnetic radiation by molecules to obtain qualitative or quantitative profiles of molecules, or to study physical processes (Workman and Springsteen, 1998). Figure

2.1 shows what can happen to a phonon injected into the system. The interaction of radiation with matter can cause redirection of the radiation and/or transitions between the energy levels of the molecules. According to different transition approach, molecular spectroscopy is divided to the three main sections. If a transition is from a lower level to a higher level with transfer of energy from the radiation field to the molecule, this process is called absorption spectroscopy. While if energy is transferred to the radiation field, or non-radiative decay if no radiation is emitted, the phenomena of a transition from a higher level to a lower level is called emission spectroscopy. As for scattering spectroscopy, it is defined as redirection of light due to its interaction with matter with or without transfer of energy. Both LIF and CRDS employed in this work are belonging to molecular spectroscopy. CRDS is a type of absorption spectroscopy while LIF is a combination of absorption and emission spectroscopy. The detailed of both techniques is discussed in the following sections. However, more detailed background knowledge of molecular spectroscopy relevant to statistical mechanics is informative for this work before step further into the more specific topics.

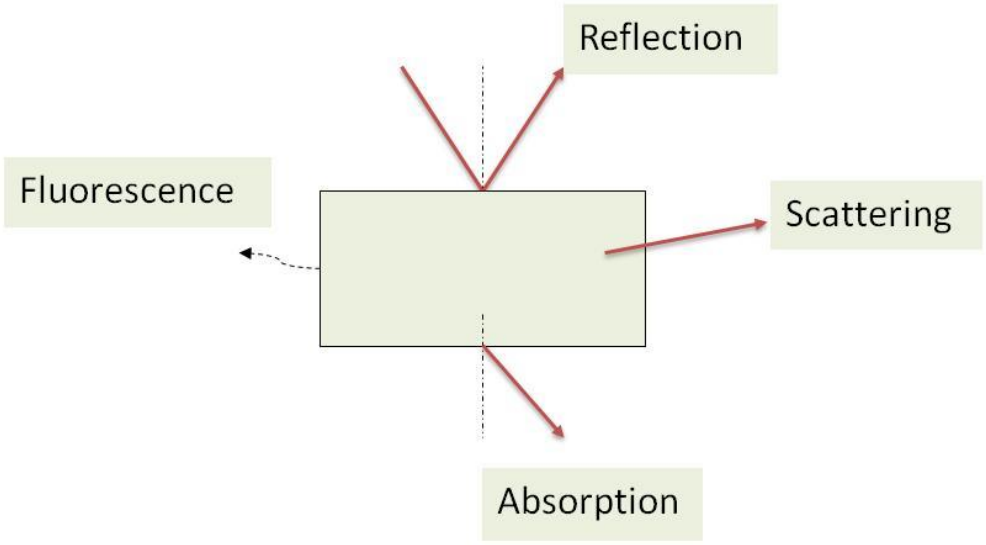

Figure 2.1: The phenomenon when a phonon injected into a system.

As known from many textbooks, the possible energy states a molecule could attain by vibration, rotation and electronic excitation. Of primary importance in diagnostics is how the molecules in any ensemble are distributed or partitioned over these states. The distribution derives from statistical mechanics and is prescribed by the Boltzmann equation (Vincenti and Kruger, 1967):

$$N_j = N \frac{g_i e^{-\epsilon_j / kT}}{\sum_j g_i e^{-\epsilon_j / kT}} \qquad (2.1)$$

where N_j is the number density of particles in the jth state of energy ε_j, N is the total number density, k is the Boltzmann's constant, T is the temperature and g_j is the degeneracy of the state. The degeneracy indicates the number of molecules which can occupy any given energy state. The denominator is termed the partition function and denoted by Q. In all of the diagnostic approaches to be considered in this work, the distribution of the molecules over the internal energy modes will be of primary interest rather than the distribution over the translational energy modes.

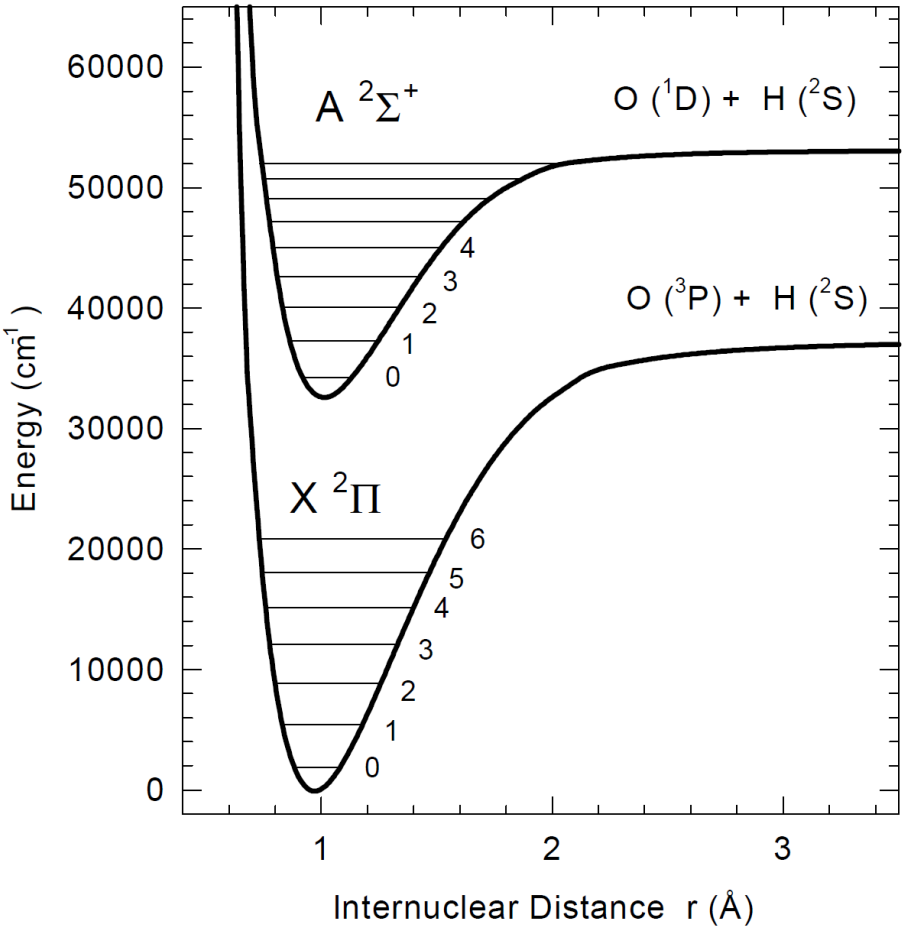

Figure 2.2: OH Energy level diagram.

As shown by the example of OH in Figure 2.2, the internal molecular energy distribution may be written, to a first approximation, as a sum of the electronic, vibrational and rotational energies:

$$E = E_{el} + E_{vib} + E_{rot} \tag{2.2}$$

Based on the definition of the partition function and the mathematical properties of the exponential, it is easy to see that the total partition function may be separated and expressed as the product of a partition function for each internal energy mode. In a similar manner, the total degeneracy can be written as the product of the degeneracies of the individual internal energy modes. Thus one can consider the distribution of population over the electronic energy states, the population distribution over vibrational levels within a given electronic state, and the population distribution over the rotational levels within a given vibrational state. For a set of allowable energy states, as prescribed by quantum mechanics, the distribution of the available population over the internal energy modes of vibration and rotation is quite temperature sensitive. The spectroscopic diagnostic techniques of interest here measure these population distributions and from them infer the temperature and concentration at the measurement location.

Consideration will now be given to the dependence of the population distribution over the vibrational and rotational states as the function of temperature. For the case of a harmonic oscillator, it is seen that the vibrational energy scales linearly with the

vibrational quantum number, v. in terms of vibrational population partitioning, the zero point energy can be neglected since it will divide out. The vibrational partition function can thus be written:

$$Q_{vib} = \sum_{v=0}^{\infty} \exp\left(-\frac{vhc}{kT}\tilde{V}\right) \quad (2.3)$$

The series is convergent and mathematically can be shown to be

$$Q_{vib} = \frac{1}{1-e^{-\frac{vhc}{kT}\tilde{V}}} \quad (2.4)$$

As for rotation, the allowable energy states are quantized in accordance with a level degeneracy given by *(2J+1)*. Thus the rotational partition function is

$$Q_{rot} = \sum_{J=0}^{\infty}(2J+1)exp(-hcBJ(J+1)/kT) \quad (2.5)$$

In the case of large *kT/hcB* the summation can be replaced by integration, and one obtains

$$Q_{rot} = kT/hcB \quad (2.6)$$

In examining rotational population distributions, the nuclear spin degeneracy, g_I, must be accounted for since it is dependent on J for nonzero nuclear spin. From this explanation of partition function and population distribution, the distributions can be noted to be quite temperature sensitive. On the other hand, this leads to laser diagnostic signatures which are quite temperature dependent and in the underlying basis for thermometry from spectroscopic approaches.

2.4 Optical diagnostics in combustion research

Optical diagnostic techniques rely on the interaction of electromagnetic radiation with the atoms, molecules, clusters, particles, and droplets present in flames. Variable properties in flames can be studied depending on the nature of this interaction. The application in combustion research includes temperature and concentration profiles of major or minor species, and their local gradients or spatial and temporal variations.

Many techniques have already introduced to fulfil these requirements, including cavity ringdown spectroscopy (CRDS), laser-induced fluorescence (LIF), laser-induced grating

spectroscopy (LIGS), laser-induced incandescence (LII), laser Doppler velocimetry (LDV), absorption, coherent anti-Stokes Raman scattering (CARS), laser-induced breakdown spectroscopy (LIBS), degenerate four-wave mixing (DFWM), extinction, phase Doppler anemometry (PDA), particle imaging velocimetry (PIV), Raman and Rayleigh scattering, and resonance enhanced multi-photon ionization (REMPI) (Kohse-Höinghaus, 2002, Eckbreth, 1996). As these acronyms indicate, this far-from-complete list of diagnostics relies on scattering, absorption, and emission techniques, on linear and non-linear approaches, and on one-photon or multi-photon schemes (Hanson, 1988, Wolfrum, 1998). As for distinguishing features of these techniques, they may vary from single-point detection to multi-dimensional imaging. Also the detections of emission may come from different methods including tracer molecules and seed particles, pump–probe and double-pulse approaches, and grating schemes (Daily, 1997, Rothe and Andresen, 1997, Kohse-Höinghaus, 1994, Laurendeau, 1988). Moreover, high-speed photography, tomography, and microscopy may be employed in combustion diagnostics. As for useful wavelength regimes and time scales in combustion diagnostics, it consists of an almost continuous spectrum from the X-ray to infrared regions and femtosecond pulses to continuous interrogation (Cheskis and Goldman, 2009, Chigier, 1991, Crosley and Chemistry, 1980). Therefore, it is informative to provide a short literature review of the achievements of optical diagnostics with their typical applications in combustion

research. This sub-section will concentrate on illustrating some avenues relevant to our experimental work. And some examples are selected to demonstrate the impact of combustion diagnostics. Optical diagnostics in combustion will be highlighted as a powerful instrument to validate and improve chemical reaction mechanisms.

First of all, temperature is regarded as one of the most important combustion parameters. It plays a key role and has a significant impact on flame chemistry. Many studies have shown that intrusive probes for temperature detection may be unreliable (Eckbreth, 1996), efforts has been devoted to the optical measurement of local temperature, spatial temperature distribution, and temperature fluctuation (Eckbreth, 1996, Laurendeau, 1988, Kohse-Höinghaus, 2002). Many laser diagnostic techniques have been developed to measure the local gas temperature. These methods cam be deduced the temperature profiles either from a thermal population of rotational, vibrational, or electronic levels or from lineshape information (Kohse-Höinghaus, 2002). In this experimental work, LIF is employed to detect temperature profiles in flames.

Secondly, optical diagnostics are considered as an instrument in resolving many aspects of combustion chemistry that is useful to predict pollutant emissions from combustion

devices. To achieve this target, detailed reaction mechanisms need to be constructed, typically assembling a consistent body of thermodynamic and kinetic data as the result of enormous collaborative effort (Miller et al., 2005). It is thus crucial to design suitable experiments in order to establish, validate, and reduce a complete reaction mechanism. Combustion optical diagnostics are widely employed to detect a large variety of species with their concentration profiles (Kohse-Höinghaus, 2002). To improve the understanding of reaction pathways, a few of experimental parameters may be carefully investigated in well-characterized flames (Kohse-Höinghaus, 2002). Many studies show the critical comparisons between simulated and experimental data including temperature as well as concentrations of several intermediates that are sensitively involving in the mechanism (Mercier et al., 2002, Gasnot et al., 1999, Berg et al., 2000, Juchmann et al., 1998).

During the last decade, models of fuel-rich flame chemistry have progressed significantly (Lindstedt and Rizos, 2002, Violi, 2004, Violi et al., 2005, Violi et al., 2002, Mehta et al., 2009). The formations of polycyclic aromatic hydrocarbons (PAHs) and soot are believed to be one of the chemically most complex processes in combustion. Moreover, the reduction of these emissions is associated with health considerations and strict regulations. Although considerable work during several decades has been

devoted to the study of soot formation, addressing the transition from gas phase molecules to clusters and particles, many details of this mechanism remain unclear. This fact leads to challenges of both the development of realistic reaction models and their validation with diagnostic measurements (Emelianov et al., 2002, Zhu et al., 2002, Basile et al., 2002). Sampling probe techniques are successful to sensitively detect larger molecular structures in fuel-rich flames (Keller et al., 2000), in spite of a potentially significant influence of the probe on flame temperature and chemistry (Hartlieb et al., 2000b). By this approach, stable compounds are often detected ex situ using chromatography and mass spectrometry (Apicella et al., 2007, Ciajolo et al., 1998), sometimes in combination with optical diagnostics (Ciajolo et al., 1998). However, this method is not feasible to measure small molecular radicals concentration profiles in sooting flames, which may be more suitable detected by in situ optical diagnostics (Griesheimer and Homann, 1998). Also, theoretical chemistry concepts and molecular dynamics are believed as contributions to the construction of these complex mechanisms (Moskaleva and Lin, 2002, Violi et al., 2005). The reaction pathways to form the first aromatic ring are considered as an important step (Lindstedt, 1998, Pope and Miller, 2000). To provide a consistent database for comparison with simulations, fuel-rich premixed low-pressure flames of different fuels have been investigated using

both a combination of laser diagnostics and in situ mass spectrometry (Kohse-Höinghaus, 2002) and laser diagnostics only (Schocker et al., 2005).

However, innovative diagnostic approaches are demanded to overcome the inherent difficulties of optical measurements due to complex environment in fuel-rich combustion (Hartlieb et al., 2000a, Kohse-Höinghaus, 2002, Kamphus et al., 2002, Yang et al., 2007, Blevins et al., 2002). The proposing approaches should have the abilities of unperturbed, isomer-specific and quantitative detection of intermediates (Roesler et al., 2003, Atakan et al., 2003).

2.5 Laser-induced fluorescence

2.5.1 LIF theoretical background

Laser-induced fluorescence (LIF) is regarded as one of the most sensitive and non-intrusive detection techniques of all analytical methods. Successful examples cover many different applications, such as exploration of the structure of molecules, species-selective detection and flow visualization and measurements (Daily, 1997, Kohse-Höinghaus, 1994). Recently, LIF is widely used in combination with other diagnostic techniques such as CRDS (Berden and Engeln, 2009, Mercier et al., 2005). These combinations are able to overcome inherent difficulties of LIF in some combustion environments. Also, it helps to enhance the abilities of other techniques such as the spatial resolution. More recently, LIF is developed to monitor PAHs generation in sooting flames (Desgroux et al., 2013, Bejaoui et al., 2014). The assistance of cooling based techniques such as jet cooled LIF or photoinisation followed by analysis by time-of-flight mass spectrometry is employed to measure individual PAHs. In order to understand the theoretical background of LIF and its application, we will review the important subjects of LIF which is relevant to this work including both species

concentration measurement and thermometry capacities for combustion research in this subsection.

Laser light is used in this method to selectively excite electronic states in molecules. In order to understand the theory of LIF, consider the simple 2-level system as shown in Figure 2.3. During the transition the electronic structure of the molecules is changed. The difference in energy between ground state (1) and excited states (2) usually is relatively large. Thus, energetic light has to be used. The excited states molecule returns from state (2) to state (1) with lower energy, accompanied by a radiation of light (fluorescence). Non-radiative transitions (vibrational and rotational energy transfer) within the excited electronic state cause the fluorescence to be red-shifted with respect to the incident light. For species with suitable transitions in the UV-Vis spectral region, LIF provides selective excitation of the analyte. The main advantages of fluorescence detection are the high sensitivity (sub-ppm levels are possible) and favourable spatial resolution achievable.

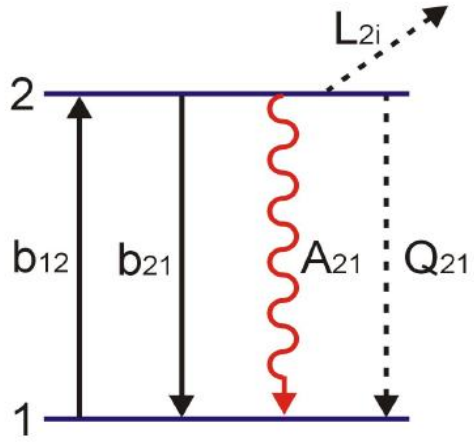

Figure 2.3: Principle of LIF in a 2-level system. *(b_{12} is the stimulated absorption rate constant, b_{21} is the stimulated emission rate constant, L_{2i} is the loss rate constant which could be due to photo dissociation or ionisation, Q_{21} is the quenching collisions, A_{21} is the rate constant for fluorescence.)*

LIF results are normally used to obtain radical concentration in flames in order to exam chemical-kinetic models. The concentration can be deduced from measured fluorescence signal. For the simplest case of a two level system in the linear laser intensity regime, the signal generated by LIF can be represented by:

$$I_{LIF} = A_{21} h\nu_{21} \left(\frac{\Omega}{4\pi}\right) V N_2 \qquad (2.7)$$

where I_{LIF} is the fluorescence intensity, $A_{21}$is the Einstein coefficient for spontaneous emission, h is Planck's constant, ν_{21} is the frequency of the emitted radiation, Ω is the detection solid angle, V is the observation volume, N_2 is the number density in the

excited state. However, it is difficult to propose a general equation to evaluate the radical density from multi-level systems in combustion processes, because lots of quantum states populated by collision processes will be involved in the generation of the observed fluorescence signal, and the relation is varying depending on experimental procedure, dynamic features of the molecule, and the spectroscopic.

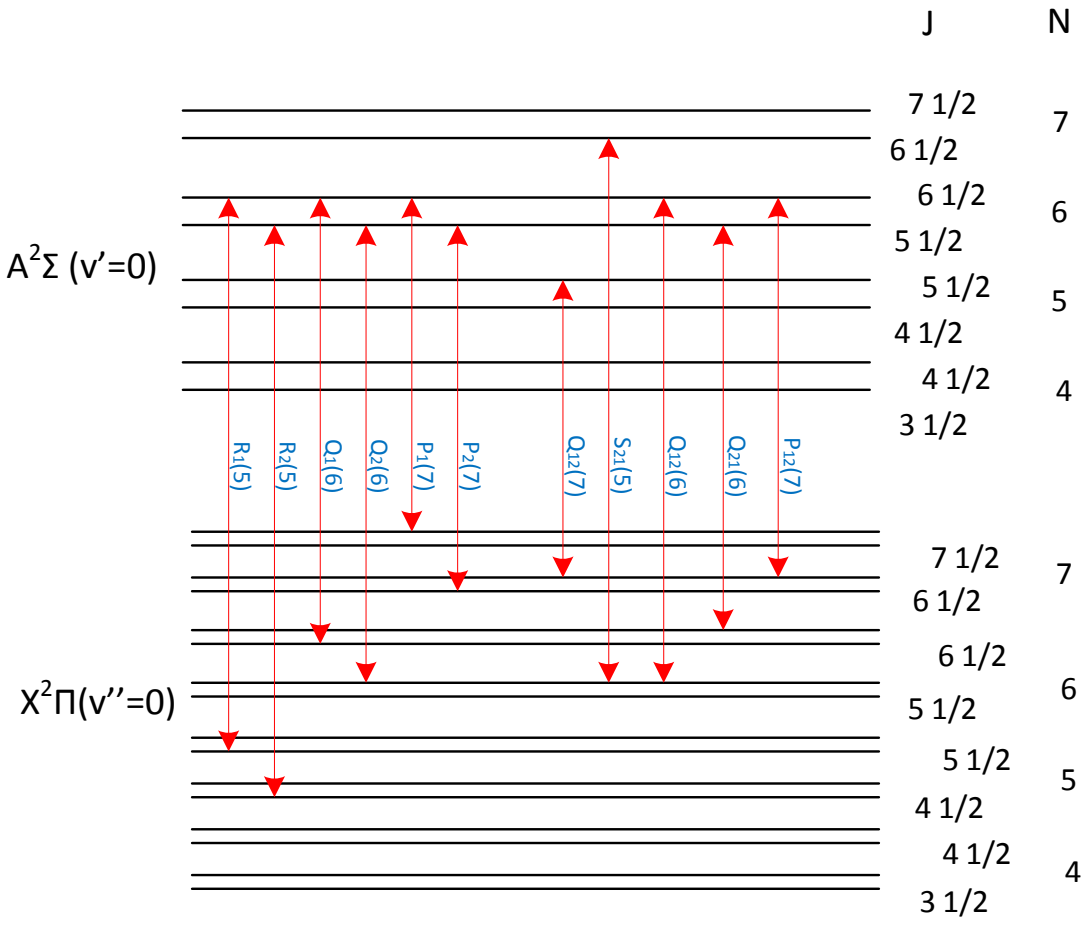

Figure 2.4: OH energy level diagram of rotational structure of the A-X (0-0) band.

The OH energy level diagram in Figure 2.4 is summarizing the important processes. By absorbing a photon of suitable energy, an excited energy level ($A^2\Sigma$ in Figure 2.4) is populated, and light is emitted at the same and different wavelengths according to selection rules for allowed transitions (such as $R_1(5)$, $Q_2(6)$, and $S_{21}(5)$ in Figure 2.4). As for typical LIF experiments, light emitted either from a single quantum state or broadband radiation is detected. The fluorescence intensity provides information on the concentration of the emitting species. For quantitative interpretation, all competing depopulation processes need to be considered. It is clear that a large number of experimental parameters that are important to evaluate LIF experiments. These include observation volume, pulse duration of the laser radiation, the power density, solid angle, detection efficiencies of optics and detectors (filters, monochromators, photomultipliers or cameras), and spectral profile. The evaluation of LIF experiments is also affected by transition probability, absorption lineshape and fluorescence quantum yield. Most of the required parameters can be obtained for a particular experimental situation when a suitable calibration technique is made. However, the main problem is on the determination of the fluorescence quantum yield. The fluorescence intensity and spectral distribution are affected by collision processes when excited with a pulsed laser. In addition, the local collision efficiency that affects the fluorescence quantum

yield is influenced by pressure, temperature and chemical composition at the observation volume. Therefore, the fluorescence quantum yield varies significantly with position, and it thus makes quantitative LIF measurements difficult in such environments. However, there are several strategies proposed to render LIF quantitative if the quantum yield is not precisely known. The most widely application is absorption calibration measurement under the same conditions.

The first step of LIF measurement is usually to obtain the species LIF spectra in order to find the excitation lines and determine which line(s) will be chosen for future probing. In this work, we obtained the OH LIF spectra and compared them with the simulated spectra by LIFbase (Luque and Crosley, 1999). In this stage, a brief description of LIFbase is necessary for theoretical understanding and informative. Spectral simulation in electronic systems can be done by LIFbase, including the possibility of modifying many parameters interactively. The spectral simulation by LIFbase permits the calculation of several kinds of spectra including emission, absorption and excitation LIF. In this work, we focus on the excitation LIF spectral simulation. The simulated excitation LIF spectra include two steps calculation processes: absorption firstly, and then emission from the populated level. The theoretical expression can be written as:

$$I_{v''J''} \propto N_{v''J''} B_{v'J'}^{v''J''} \sum_{v''J''} A_{v''J''}^{v'J'} \tau(1 - e^{-\frac{t}{\tau}}) \quad (2.8)$$

where $A_{v''J''}^{v'J'}$ and $B_{v'J'}^{v''J''}$ are the emission and absorption coefficients between upper levels v', J' and a lower levels v'', J'' respectively (Schadee, 1978), τ is the lifetime, and N is the population. There are some conditions if applying this expression: (1) the intensity of the laser field is low and there are no saturation effects; (2) the detection system is collecting the total fluorescence with the same detection efficiency for all the wavelengths; (3) polarization effects are negligible; (4) vibrational or rotational relaxation effects are not important, because the fluorescence is assumed to come from the laser-populated level in the excited state; (5) the pumping laser is shorter than the effective lifetime. According to the explanation of LIFbase, the LIFbase programme is designed to compile all the information available from transition probability calculations on the diatomic molecules including OH. The output of this program provides the data of Einstein emission and absorption coefficients, radiative lifetimes, transition probabilities, frequencies and Hönl-London factors for many bands including the OH (A-X) bands. Besides providing the spectral simulation, the variation of the absorption and emission coefficients with vibration and rotational quantum numbers plays a key role to obtain accurate rotational and temperatures in this work.

2.5.2 LIF thermometry capability

Besides the concentration measurement potential of LIF, the most interest character in this work is LIF thermometry. As for measurement of temperature with LIF, it also needs to consider the influencing parameters under different conditions on the one hand. These parameters are similar as the concentration measurement including polarization effects, absorption of the laser radiation, and collisional energy redistribution. On the other hand, unlike the measurement of concentration, relative values are sufficient for a temperature measurement, while several quantities need to be known in absolute units (including transition probabilities, size of the observation volume, detection solid angle and efficiency, and fluorescence quantum yield) for a concentration measurement. In addition, temperature is almost exclusively evaluated from population distributions in at least two levels so that information on the population in a single quantum state is sufficient. In short, the intensity of a fluorescence line is proportional to the population in the corresponding level. Temperature can be deduced by comparison of simulated spectra with measured ones. The diagnostic strategy in this work is to measure the OH radicals thermalized rotational population distribution function of a single vibrational level within the ground electronic state via resonant absorption resulting in the fluorescence signal. There are a few of sub-methods from

this principle. Here, we are focusing on the review of the extraction of rotational temperature from experimental OH LIF spectra using the linear Boltzmann plot due to the relevance to this work.

Because the Boltzmann plot method for calculating temperature needs to utilize a set of LIF excitation spectra covering a wide range of J'' values, we can write the expression of each spectral peak fluorescence signal as

$$I(J'',T) = AB(2J''+1)e^{-\frac{E_{v'',J''}}{kT}} \tag{2.9}$$

where *A* is a factor assumed to be independent of the excited ground state rotational level J''

By considering that we use the thermalized rotational population distribution function of a single vibrational level within the ground electronic state, we can take the logarithm of both sides as following:

$$\ln\left(\frac{I(J'',T)_{LIF}}{gB}\right) = -\frac{E_{v'',J''}}{kT} + constant \tag{2.10}$$

In the generalized form as

$$\ln(I_{LIF}/gB) = -(E/kT) + constant \quad (2.11)$$

Temperature can be obtained from the slope of this semi-logarithmic plot of the fluorescence intensity I_{LIF}, weighted by the Einstein *B* coefficient and degeneracy *g* also known as $(2J'' + 1)$, versus the energy *E* of the corresponding level. When considering fluorescence spectra, the values of *B* and *g* for the upper state have to be used. OH thermometry using fluorescence spectra are employed in this work due to the compatibility with other experiments. Spectrally-resolved detection is combined with single-lines excitation by pulse-laser in order to determine the temperature from fluorescence spectra. Principal advantages of this method include high spatial resolution and capability with unsteady flows. Successful application (Chan and Daily, 1980, Furuya et al., 1985, Eckbreth, 1996) of this technique can be found in many groups. In this work, OH LIF concentration measurement has been performed firstly to get OH fluorescence spectra in different flame condition. The qualitative OH concentration profiles in different position and condition were also obtained by this technique. The most important intention by employing this technique is to achieve the temperature profiles in the flames. These results are essential for all other results below.

2.6 Cavity-Ring Down Spectroscopy

2.6.1 CRDS theoretical background

Cavity Ring Down Spectroscopy (CRDS) is highly effective laser technique for measuring the transmission, or more accurately, the absorbance, of light through substances. Especially, the substances to be detected are in gaseous form. Extremely sensitive measurements can be achieved by using the methods of CRDS, allowing scientists to measure very small differences in the amount of absorbed light. CRDS was introduced by O'Keefe and Deacon (Okeefe and Deacon, 1988) in 1988, after that many developments and applications of the CRDS have been reported in combustion research (Kohse-Höinghaus et al., 2005, Evertsen et al., 1999, Evertsen et al., 2003a, McIlroy, 1998, Schocker et al., 2005). In order to understand the theoretical background of CRDS and its application, we will review the important subjects of CRDS which is relevant to this work, compare between the different experimental setups, and summarize its successful application in combustion research in this subsection.

The CRDS technique is based on the measurement of the decay rate of light trapped inside an optical cavity of particularly high-reflectivity. A small amount of the laser light

(typically, < 0.001%) leaks out of the cavity on each reflection. A detection system, which is composed of a photo-sensitive detector located behind the output mirror and data acquisition equipment, record the tiny intensity of light transmitted through it. Because of the losses of light on each reflection, the amount of light inside the cavity is slightly less after each bounce. Moreover, the light intensity is reduced by a given percentage on each round trip, so the amount of light measured also decreases with each reflection. In addition, if some substances that absorb light are placed in the cavity, the amount of light decreases faster. In the summary, the detector can measure and show an exponential decay which is related to losses that depend on the residual mirror transmission and on the absorbing medium between the mirrors. This is shown in Figure 2.5 and Figure 2.6.

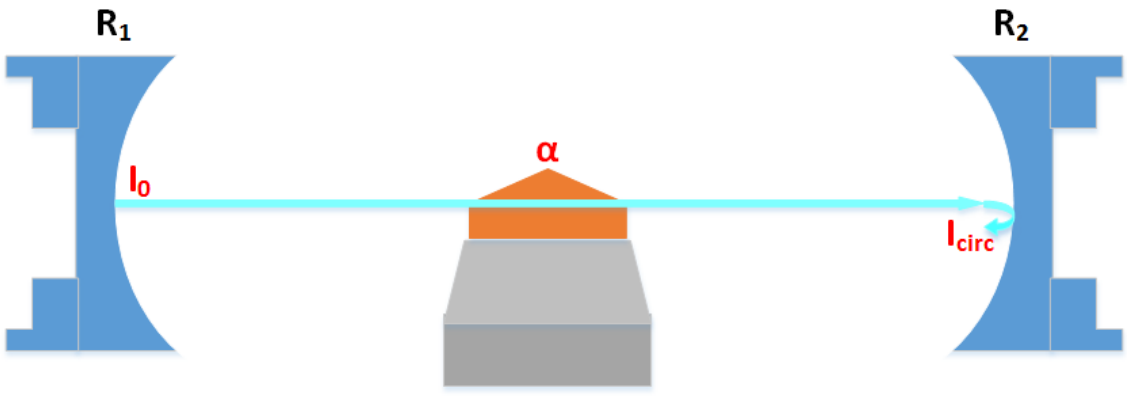

Figure 2.5: Schematic diagram of a cavity with trapped light. *The mirrors reflectivities are R1 and R2 (in this work, R1= R2); α the absorption coefficient of a medium inside the cavity, I0 initial light intensity, and Icirc circulating light intensity.*

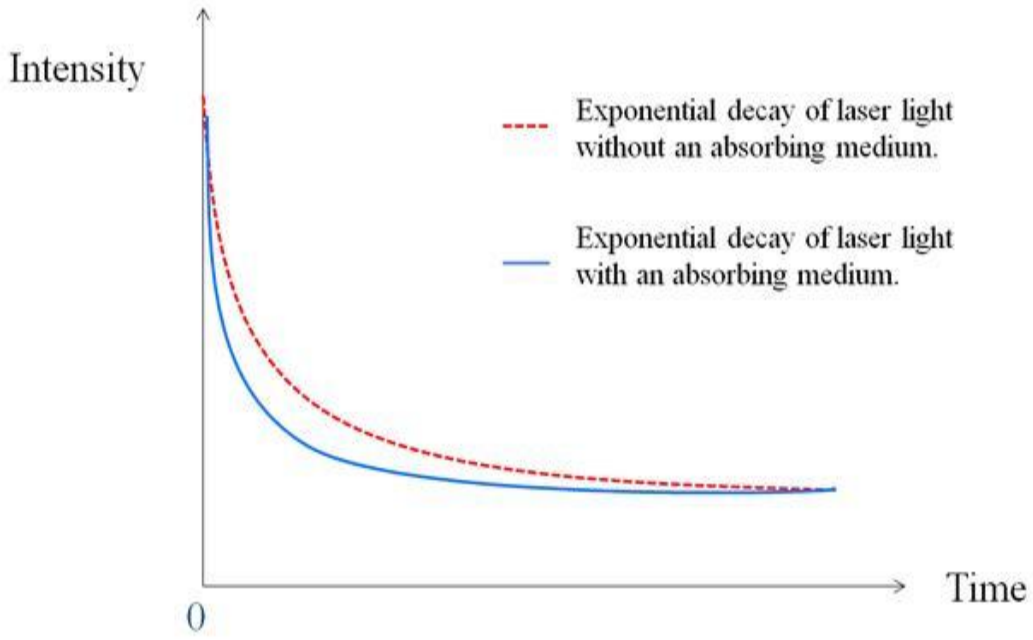

Figure 2.6: Exponential decay of laser light within the ring-down cavity.

The CRDS setup will measure how long it takes for the light to drop to a certain percentage of its original amount, and this "ring down time" can be used to calculate the concentration of the absorbing substance in the gas mixture in the cavity.

To understand the basis of the CRDS technique, suppose that an optical cavity of length L is excited by a laser pulse with intensity I_{in}. For the sake of clarity initially assume that the pulse duration is smaller than the round trip time in the cavity. A small fraction of the pulse enters the resonator through the mirror and becomes trapped inside, moving

back and forth between the mirrors. Then after the first pass through the cavity, the detector will measure intensity:

$$I_0 = T^2 e^{-\alpha d} I_{in} \tag{2.12}$$

where T is the mirror intensity transitivity, and α, which corresponds to the absorption coefficient, $\alpha=\sigma C$, is the frequency-dependent absorption coefficient of any substances (such as a gaseous, liquid or solid sample) occupying a region of length d inside the cavity. So the factor $e^{-\alpha d}$ is known as the single pass intensity attenuation for absorption by a homogeneous sample according to the Beer–Lambert law. Note that this term might also correspond to a scattering loss. For each following round trip, the intensity will decrease by an additional factor of $R^2 e^{-2\alpha d}$, where R is the mirror intensity reflectivity. Thus, after n round trips, the light intensity at the detector will be

$$I_n = (Re^{-\alpha d})^{2n} I_0 = I_0 e^{-2n(-lnR+\alpha d)} \tag{2.13}$$

The recorded signal from the detector would consist of a train of pulses with intensity decreasing exponentially according to Equation 2.13. However, the duration of the laser pulse is actually much longer than the time for a single round trip in most experiments, and the pulse train would be smoothed to an envelope of pulse amplitudes that decrease continuously by time. The number of cavity round trips, n, can therefore be

transformed to a continuous time variable, *t=2Ln/c* corresponding to the time which the light pulse has taken inside the cavity to pass a distance of *2Ln*:

$$I(t) = I_0 e^{-\frac{ct}{L}(-lnR+\alpha d)} \tag{2.14}$$

The decay time constant, corresponding to the time taken for the initial intensity to decrease by factor of *e*:

$$\tau = \frac{L}{c(-lnR+\alpha d)} \tag{2.15}$$

is called a ring down time (RDT) of the cavity.

Since the mirrors of the cavity are highly reflective, *R≈1*, we may approximate *ln R ≈ -(1-R)* and rewrite Equation 2.15 as

$$\tau = \frac{L}{c((1-R)+\alpha d)} \tag{2.16}$$

Therefore, it is known that the RDT depends on the reflectivity of the cavity mirrors, the cavity length and the absorption by the medium enclosed by the cavity. Note that it

does not depend on the intensity of the laser pulse and, as a result, is not affected by intensity fluctuations. Thus the RDT for an empty cavity is simply:

$$\tau_0 = \frac{L}{c(1-R)} \tag{2.17}$$

The CRDS technique is highly sensitive. For typical values for modern mirror coatings of $R = 0.9999$ and $L = 1\ m$, we calculate from Equation 2.17 that $\tau_0 = 33\ \mu s$ and the light pulse travels 10 km in this time. Therefore the cavity ring down spectrometer is the analogue of an absorption cell with effective path length of about 10 km. However, the required volume of the instrument and experimental samples for this technique can be much smaller than the direct absorption cells. Moreover, another advantage of the method is its immunity from pulse-to-pulse fluctuation of the laser light because the measured decay rates are independent of the pulse intensity.

Written in terms of the absorption coefficient, $\alpha=\sigma C$. If τ and τ_0 are experimentally recorded as functions of the laser frequency, the absorption spectrum of a sample within the cavity can be calculated using Equation 2.18

$$\alpha = \sigma C = \frac{\Delta\tau}{\tau_0 \tau}\frac{\mathrm{L}}{\mathrm{cd}} = \frac{\Delta \mathrm{kL}}{\mathrm{cd}} \quad (2.18)$$

where $\Delta\tau=\tau_0-\tau$, and $\Delta k=(1/\tau)-(1/\tau_0)$ is the change in the ring-down rate coefficient (in s^{-1}).

From analyzing Equation 2.18, the concentration of a sample can be directly calculated from measured changes in the RDT or rate coefficient in the presence and absence of the sample if the absorption cross-section of the sample is known at a particular frequency *v*.

2.6.2 General consideration of CRDS application in combustion studies

In order to successfully apply CRDS technique in combustion processes, we also need to fulfil the stability condition of a cavity. This condition is based on the ratio of the cavity length to mirror curvature radius. The *g*-parameters for mirrors in a cavity are expressed as

$$g_n = (1 - \frac{L}{r_n}) \quad (2.19)$$

where *r* is the mirror curvature radius, *L* the cavity length and *n* the mirror index. The stability condition for a cavity is achieved if

$$0 \leq g_1 g_2 \leq 1 \tag{2.20}$$

In most CRDS application, two identical mirrors are used to form the cavity; therefore, the criteria to form a stable symmetric cavity should have the following condition.

$$L \leq 2r \tag{2.21}$$

According to this expression, the mirror curvature radius has to be longer than half of the length of a stable cavity. In our case, a curvature radius of *r = 6 m* and cavity length of *L = 0.64 m* fulfil the stable cavity condition.

In this work, we inject pulsed monochromatic laser beam into the cavity so that the cavity spot size at the waist (ω_0) and at the mirrors ($\omega_{1,2}$) can be expressed respectively as

$$\omega_0 = \sqrt{\frac{L\lambda}{\pi}} \left[\frac{g_1 g_2 (1 - g_1 g_2)}{(g_1 + g_2 - 2 g_1 g_2)^2}\right]^{0.25} \tag{2.22}$$

$$\omega_{1,2} = \sqrt{\frac{L\lambda}{\pi}}\left[\frac{g_{2,1}}{g_{1,2}(1-g_1 g_2)}\right]^{0.25} \quad (2.23)$$

where λ is the wavelength of the monochromatic light.

As for CRDS application in flame studies, mode matching of the laser beam to the cavity should be considered carefully in order to construct a proper experimental setup. Usually, it can be achieved by placing a lens-pinhole-lens combination in front of the cavity (Berden and Engeln, 2009). This technique is useful to design the experimental setup for flame studies. The positions of the optical components can be determined by following this rule in order to allow the spatial coupling of an incident Gaussian beam to the TEM_{00} mode of the cavity. The greatest benefit of this design is the preservation of the transverse spatial resolution in flame studies.

According to this method, the laser beam is focused by the first lens and then passed a pinhole at the focusing point. The beam passes to the second lens in order to focus into the cavity. A numerical application of the ABCD law was proposed to help the calculation. The features of the incident beam at the pinhole position and the resulting beam after propagation through the lens at the centre of the cavity can be expressed by

their q parameters in accordance with the *ABCD* law (Berden et al., 2000, Berden and Engeln, 2009, Yariv, 1967):

$$q_{out} = \frac{Aq_{in}+B}{Cq_{out}+D} \tag{2.24}$$

where

$$\frac{1}{q_{in}} = \frac{1}{r_{in}} - i\frac{\lambda}{\pi\omega_{in}^2} \tag{2.25}$$

and

$$\frac{1}{q_{out}} = \frac{1}{r_{out}} - i\frac{\lambda}{\pi\omega_0^2} \tag{2.26}$$

with $r_{in} = r_{out} = \infty$ (radius of curvature of the wave) at both beam waist positions.

A, B, C, D parameters define all the optic components positions including the focusing lenses and pinhole positions. The matrix can be calculated as

$$\begin{bmatrix} A & B \\ C & D \end{bmatrix} = \begin{bmatrix} 1 & \frac{d}{2} \\ 0 & 1 \end{bmatrix} \begin{bmatrix} 1 & \frac{n_1}{n_2}e \\ \frac{n_2-n_1}{n_1 r_m} & 1 \end{bmatrix} \begin{bmatrix} 1 & d_2 \\ 0 & 1 \end{bmatrix} \begin{bmatrix} 1 & 0 \\ -\frac{1}{f} & 1 \end{bmatrix} \begin{bmatrix} 1 & d_1 \\ 0 & 1 \end{bmatrix} \tag{2.27}$$

where *d* is the cavity length, *e* the mirror thickness, n_1 and n_2 respectively the outside and inside refractive indices of the mirrors, r_m the reflectivity of the cavity mirrors, *f* the

focal length of the second lens, d_1 the distance from the pinhole to the second lens, and d_2 the distance from the second lens to the first cavity mirror. Therefore, d_1 and d_2 can be determined by resolving equation, which results in only on real solution if and only if

$$A - (\frac{\omega_0}{\omega_{in}})^2 D = 0 \quad (2.28)$$

and

$$B + \frac{\pi^2 \omega_0 \omega_{in}}{\lambda^2} C = 0 \quad (2.29)$$

Values of d_1 and d_2 can be iteratively calculated with the computational software aid of Mathcad or Matlab.

2.6.3 Comparison of CRDS configurations

After O'Keefe's invention of pulsed CRDS, many variants of this technique have been developed such as continuous wave CRDS (Romanini et al., 1997a, Romanini et al., 1997b, Paldus et al., 1997), phase shift CRDS (Engeln et al., 1996) and cavity enhanced absorption spectroscopy (Peeters et al., 2001). The different devices required for each technique are shown in Figure 2.7, and the advantages and disadvantages of pulsed-

and continuous-wave- CRDS are listed in Table 2.1. These four techniques have a similar implementation in generally. Light source that usually comes from a laser, whereas pulsed- and continuous-wave- CRDS (including phase shift CRDS and CEAS) use single mode pulsed and narrowband cw lasers respectively. A cavity is constructed by two mirrors of high reflectivities and the detector systems are the necessary components for all of them. However, as for the approaches of cw CRDS and CEAS, a piezoelectric transducer is demanded for being mounted on the end of a mirror, and as for cw CRDS and PS CRDS measurements, extra devices, which are a fast optical switch for cw CRDS and an electro optical modulator for PS CRDS respectively, is necessary for applications. Due to the requirement of relative large tuning range as well as the experimental setup simplicity and compatibility with LIF, pulsed CRDS have been selected in this work to detect absolute concentration profiles of HCO and $^{1}CH_2$ in different flame condition and position.

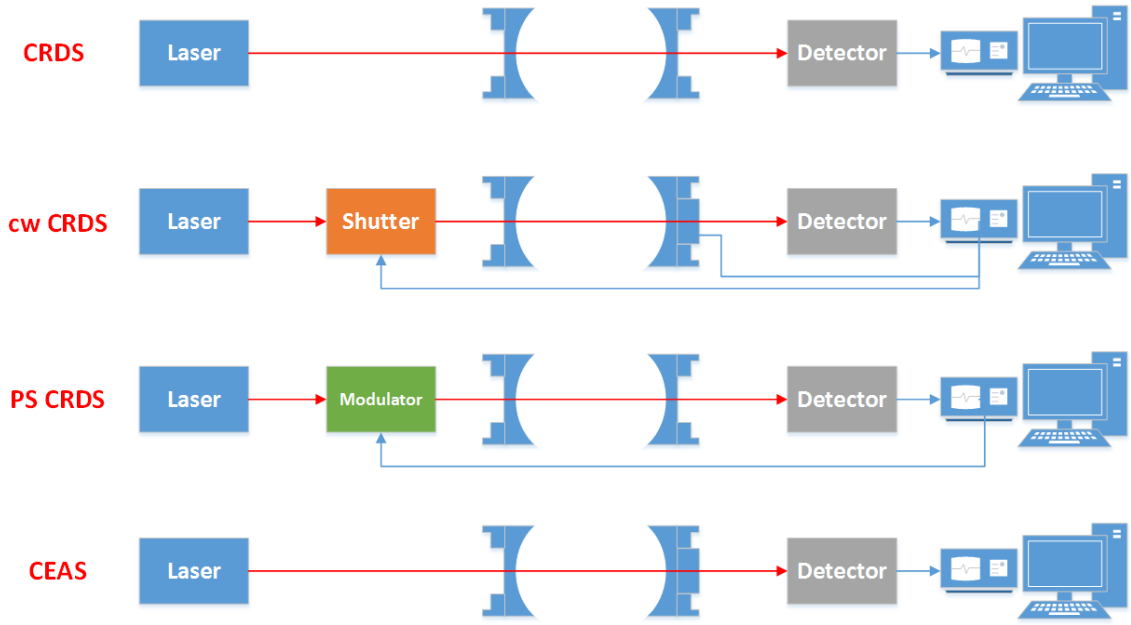

Figure 2.7: Generalized schematics of pulsed CRDS, cw CRDS, PS CRDS and CEAS implementations.

Cavity ringdown technique	
Pulsed	Continuous-wave
Simplicity of experimental setup	Acousto- or electro-optical modulator and cavity or laser frequency modulation requried
Broadband: 1 Multimode excitation; 2 Multiexponential decay	Monochromatic: 1 Single-mode excitation; 2 High spectral resolution
Large tuning range of pulsed lasers	Small tunning range of cw lasers
Short cavity: Reduced multimode excitation	Long cavity: High sensitivity
Pulse repetition rate of laser	High repetition rate possible: High Sensitivity
Short energy build-up time in cavity	Long energy build-up time in cavity: Improved signal-to-noise

Table 2.1: Overview of pulsed and cw cavity ringdown spectroscopy techniques.

2.6.4 Literature review of CRDS application in combustion processes

After the introduction of CRDS technique by O'Keefe and Deacon (Okeefe and Deacon, 1988) in 1988, this technique has been developed and applied spectacularly in many

kinds of fields including analytical chemistry, molecular transients of astrophysical interest, atmospheric chemistry, medical applications and combustion studies. There are thousands of studies reported on CRDS and its applications to date. Our focus in this work is to obtain intermediate species profiles in order to test and validate combustion models. Such data is required to be high fidelity for combustion, both from a spatial- and temporal-resolution perspective. LIF as the most widely-used method has been applied to study flame structure for many decades, because it can provide nonintrusive, instantaneous, spatially resolved and highly sensitive measurements of reactive species. However, LIF also has many limits including the well-known difficulty of calibrating relative signals and the capability of a relatively small number of species (mostly diatomic or triatomic radicals). Especially, LIF is not capable to detect non- or weakly fluorescing species such as $^{1}CH_2$. Therefore, since end of 1990s, CRDS has started to be employed in flame studies to fulfil the modelling requirements and other diagnostic techniques restrictions. There are not many studies reported on CRDS application in combustion studies to date. An overview of the relevant species to this work tabulated in Table 2.2 that were successfully detected by CRDS in combustion processes can be very informative in this thesis. Besides the CRDS studies in combustion tabulated above, there are many other intermediate radicals that have been successfully detected by CRDS in atmospheric combustion environments. These studies are informative to this

thesis and the future work as well. CH has been studied at diffusion flame (Mercier et al., 1999a), premixed flame (Evertsen et al., 2003b) and counterflow flame (Naik and Laurendeau, 2004). Sepman et al (Sepman et al., 2003) reported the first NO CRDS detection in a premixed atmospheric flame. OH is also studied by CRDS in non-sooting premixed atmospheric flames (Dreyer et al., 2001, Mercier et al., 1999b, Schocker et al., 2003). More recently, lots of CRDS application in combustion is focusing on larger molecules and soot. Moreau et al have reported soot and PAHs detection by CRDS in a atmospheric diffusion flame (Moreau et al., 2004). After that, more studies of PAH and soot detection by CRDS can be found in atmospheric diffusion and premixed jet flames (Bouvier et al., 2007, Therssen et al., 2007) and premixed flame (Desgroux et al., 2008). Moreover, this technique has already applied to detect useful species in surface chemical interactions in catalytic combustion (Badra et al., 2013) and nanoparticle-generating flame reactors (Rahinov et al., 2014).

Species	Flame conditions	Excitation wavelength (nm)	Reference
HCO	Premixed, low pressure, rich, non-sooting flame	615	(Schocker et al., 2005)
HCO	Premixed, atmospheric pressure, non-sooting flame	615	(Evertsen et al., 2003a)
HCO	Premixed, low pressure, non-sooting flame	615	(Scherer and Rakestraw, 1997)
$^1CH_2$	Premixed, atmospheric pressure, non-sooting flame	622	(Evertsen et al., 2003a)
$^1CH_2$	Premixed, low pressure, non-sooting flame	622	(McIlroy, 1998)
$^1CH_2$	Premixed, low pressure, rich, non-sooting flame	622	(Schocker et al., 2005)

Table 2.2: Relevant species to this work detected in flames by CRDS including the excitation wavelengths and flame conditions.

As shown in the table above, both of $^1CH_2$ and HCO were only studied and compared with the combustion models in non-sooting flames, though their important roles in flame structure and PAHs formation mechanisms in sooting flames have already been discussed. There is no validation between experimental results of both species and the

combustion model (Appel et al., 2000) that consists of both gas phase and soot dynamic model in sooting flame.

CHAPTER3: EXPERIMENTAL SETUP

3.1 Overview

In this study, free radicals diagnostic and temperature profiles determination experiments in flames were performed in various flame conditions (fuel equivalent ratio between 1.7 and 2.1) at atmospheric pressure. Laser-Induced Fluorescence (LIF) and Cavity Ring-Down Spectroscopy (CRDS) techniques were employed in these experiments by using a high-power Nd:YAG laser (Surelite continuum SLII-10) pumping a dye laser (Sirah Cobra). A flat flame burner produces an approximately planer reaction zone, and therefore can be considered as a one-dimensional process to a good approximation. The flame that was used in this work is premixed ethylene/air-flame on a flat flame burner with a porous plate of diameter 33 mm. The burner was efficiently cooled by a water-cooling jacket. The flame are stabilized by a steel cylinder located 21 mm above the burner surface (Bladh et al., 2009). A photomultiplier tube (Hamamatsu R636-10) with appropriate collection lens and filters or monochromator (Oriel cornerstone 130) was used to acquire experimental signals. These signals were digitized and saved by an oscilloscope (Tektronix DPO2024). A LabView program written by the present author was used to control the laser, monochromator and oscilloscope as well

as collect data automatically during these experiments. All of the optics is mounted on an all-steel construction, excellent stability, and broadband damping optimized optical table. In addition, the optical table legs are all mounted on the solid floor in order to isolate vibrations. The excitation, combustion and detection subsystems will be discussed more detailed in this chapter.

3.2 Excitation system

Many laser systems used in combustion studies were discussed by Eckbreth (Eckbreth, 1996). In most LIF applications, a pulsed laser is considered to be a preferred illumination source (Daily, 1997), because fluorescence lifetime of small gas-phase molecule are often much shorter than nanoseconds. Picoseconds are used to measure fluorescence lifetime. A significant advantage of short pulse is the discrimination against background radiation. Thus, the most common illumination systems employed in LIF projects are Nd:YAG laser pumping dye lasers or excimer lasers (Daily, 1997). The Nd:YAG laser produces pulses at the wavelength of 1064 nm, and is doubled by optic devices to 532 nm in order to pump a dye laser. The excimer lasers are usually used with different lasing medium depending on frequency requirements. The available

commercial options include ArF-193 nm, KrCl-222 nm, KrF-248 nm, XeCl-308 nm, XeF-353. These kinds of excitation system can provide pulse energies of more than1 J at low repetition rates (low to 0.03Hz) and lower energies at higher repetition rates (up to hundreds of Hz). Because excimer lasers are only available at narrower range of wavelengths and cannot be tuned wide range, therefore, in this study, a Nd:YAG laser (Surelite continuum SLII-10) was used to generate 532 nm pulses with energy of 280 mJ delivered in 4-6 nanoseconds at repetition rates of 10 Hz. A dye laser (Sirah Cobra) was pumped by the pulsed laser in order to produce tuneable wavelengths around 308 nm (with doubling crystal) and 610 (without doubling crystal) with the dye of Rhodamine 640. The maximum pulse energies were about 6 mJ at these wavelengths.

Flexibility and compatibility for the CRDS are another important motivation to choose this excitation system. At the beginning of this study, flame temperature and OH concentration profiles have been probed by LIF at the wavelength of 308 nm. And then CH and $^{1}CH_{2}$ concentration profiles need to be considered at the absorption wavelength by CRDS around 610 nm which is almost double of the OH LIF required wavelength. Thus, without any major modification, LIF measurement, thermometry and CRDS measurement in this study can be performed by using the same excitation system.

Many essential lenses and optics were also used in the system before laser beam was injected into flames. As for LIF measurement and thermometry, a focusing lens (diameter 1 inch, focal length 750 mm) was used to focus the UV laser beam into the central of flames. As for CRDS, the laser beam was focused into the centre of the cavity by a telescope system consisting of an aperture of 50 microns diameter and two identical convex (diameter 1 inch, focal length 75 mm). The focusing system was adopted and adjusted in order to obtain a Gaussian beam and match approximately the TEM_{00} transverse mode of the optical cavity. Two different sets of cavity mirrors have been adopted depending on the investigated species. For UV measurements (OH and CH radicals), cavity mirrors with a radius of curvature of R = 6 m (HR 308 nm, Reflectivity 99.5%, CRD Optics Inc.) were used. For visible light measurements (HCO and $^1CH_2$ radicals), two identical 0.8 inch diameter plano-concave mirrors with radius of curvature of R = 6 m (HR 610 nm, Reflectivity 99.995%, CRD Optics Inc.) were employed. The distance between each set CRD mirrors was 640 mm while the burner was fixed in the centre of optical cavity. All of the optics is mounted on special mirror mounts and posts provided by ThorLabs Polaris Line, and then securely fixed on the optical table in order to obtain long-term alignment stability. The CRD mirrors are cleaned every three

hours following by the cleaning instruction from CRD Optics Inc. in order to achieve the optimized reflectivity.

3.3 Combustion systems

Combustion processes can be classified based on whether the fuel and oxidizer are mixed before burning or mixed during burning. The first category is known as ‘premixed flames’ and the latter one ‘nonpremixed flames’. Each of these categories can be subdivided into turbulent and laminar flames based on the fluid flow. The simplest and most widely researched case is laminar premixed flames: reactants are premixed before combustion and flow is laminar. Examples are flat flames (Mckenna burner or Meker burner) and conical flames (Bunsen burner) (Kuo, 2005, Lackner et al., 2013). The flat flame burner is widely used in experimental studies due to its one dimensional structure which is favourable for modelling. A large body of research also considers non-premixed flames (Turns, 1995, Adkins et al., 2013, Kiran and Mishra, 2007). This is because the most practical combustion devices are non-premixed, partly for safety reasons.

Flat laminar premixed flames are usually employed to study flame-species concentration and temperature profiles. These profiles are usefully used for flame reaction mechanisms research in order to achieve better efficiency and lower pollution. A flat flame burner produces an approximately flat front, and therefore can be considered as a one-dimensional process to a good approximation. The flame that is used in this work is premixed ethylene/air-flame on a flat flame burner with a porous plate of diameter 33 mm. The burner is efficiently cooled by a water-cooling jacket. The flame are stabilized by a steel cylinder (diameter 33 mm) located 21 mm above the burner surface (Bladh et al., 2009). A translation mechanism is used for fine and reproducible displacement of the burner. This configuration allows the burner to move vertically on a translation stage, relative to the optical probing and detection axes, with an accuracy and reproducibility of 0.1 mm which is measured by a digital vernier calliper.

Laboratory-grade ethylene of 99.96% purity is used as the gaseous fuel and synthetic air (20% oxygen and 80% nitrogen) from BOC 287478-L-C as oxidizer. Both of the gases are stored in pressurized gas cylinders and regulated by suitable regulators. The flow rates are controlled by rotameters. Mixtures of C_2H_4 and air with different fuel equivalence ratios between 1.7 and 2.1 are chosen in order to produce sooting flames on this flat burner. Figure 3.1 illustrates the gases supply system. These flames are at the total flow

rate of 3.02 litres/minute. The sooting flames are stabilized on a flat flame burner at atmospheric pressure. The detailed conditions of the flames used in the experiment are tabulated in the Table 3.1. A series of flames horizontal check experiments have been done firstly for confirming the flame behaviour.

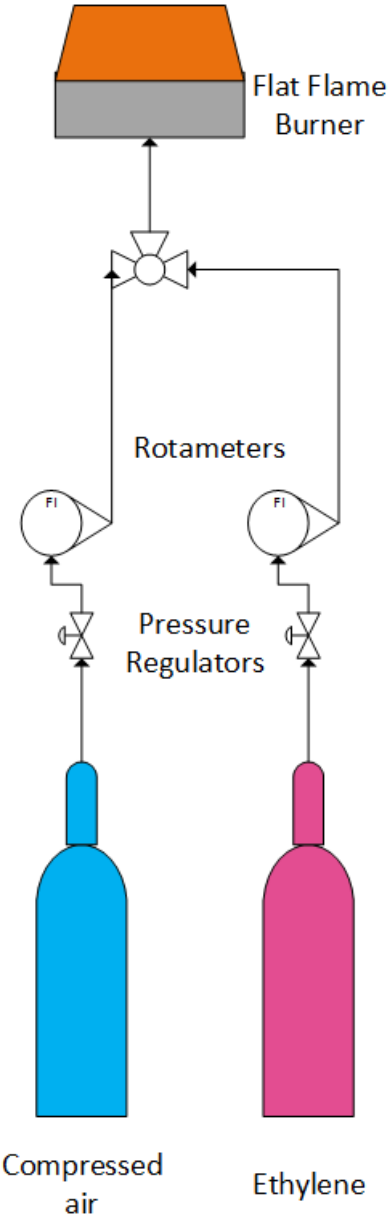

Figure 3.1: Schematic gases supply system to the flat flame burner.

Fuel equivalence ration	O_2 mole fraction	N_2 mole fraction	C_2H_4 mole fraction	Total flow rate (l/min) at 20 C	Total mass flow ($kg/m^2/s$)
1.72	0.197	0.697	0.106	3.02	0.07
1.84	0.196	0.693	0.111	3.02	0.07
1.90	0.194	0.689	0.117	3.02	0.07
2.03	0.193	0.684	0.123	3.02	0.07
2.15	0.192	0.680	0.128	3.02	0.07

Table 3.1: Experimental parameters for the flames.

3.4 Fluorescence Detection

To detect OH radicals using LIF measurement has been reported by Ketterle et al (Ketterle et al., 1992), Daily (Daily, 1997), Hanson (Hanson, 1977) and Kohse-Hoinghaus et al (Kohse-Höinghaus et al., 2005). They discussed the advantages and disadvantages in their reports. There are two bands of $A^2\sum(v^{'}=0)\leftarrow X^2\prod(v^{''}=0)$ and $A^2\sum(v^{'}=1)\leftarrow X^2\prod(v^{''}=0)$ usually used for OH LIF measurement. Both of bands were investigated and compared in this study. In order to eliminate problems with fluorescence trapping and stray light and get strong and well-isolated rotational lines to measure (Andresen et al., 1988), the $A^2\sum(v^{'}=0)\leftarrow X^2\prod(v^{''}=0)$ excitation is

preferred in this experiment to the others. The exciting UV light (wavelengths between 282 nm and 284 nm for $A^2\sum(v^{'}=1)\leftarrow X^2\prod(v^{''}=0)$ band, and 304 nm and 308 nm for $A^2\sum(v^{'}=0)\leftarrow X^2\prod(v^{''}=0)$ band) was provided by the laser system. In order to get a LIF spectrum and find the strongest absorption line in these ranges, data points were measured at every 0.002 nm firstly.

The major concerns are always the spatial response and light-gathering capability when designing a suitable signal-collecting system in flames studies. At the beginning of this project, the $A^2\sum(v'=1)\leftarrow X^2\prod(v''=0)$ band excitation fluorescence were collected by a signal collection lens (diameter 2 inch, focal length 300 mm) onto a detector (photomultiplier Hamamatsu R636-10) equipped with a two-glass filters (WG 305, UG 11) and connected with an oscilloscope (Tektronix DPO2024). As for the $A^2\sum(v'=0)\leftarrow X^2\prod(v''=0)$ band excitation experiment, a system used to collect laser-induced fluorescence signal consists of the same convex lens with the focal length of 300 mm, a monochromator (Oriel cornerstone 130) with the entrance slit size of 3 mm and exit slit size of 280 μm, the same photomultiplier tube and digital oscilloscope. The fluorescence signal was collected by this lens and focused at the entrance slit of monochromator. The photomultiplier tube was mounted at the exit of the monochromator, and the signal was processed and recorded by the oscilloscope. Both

of oscilloscope acquisitions were communicated to a personal computer via a general-purpose interface bus (GPIB) by a LabView program written by the present author. The screenshot of this LabView program is showed below.

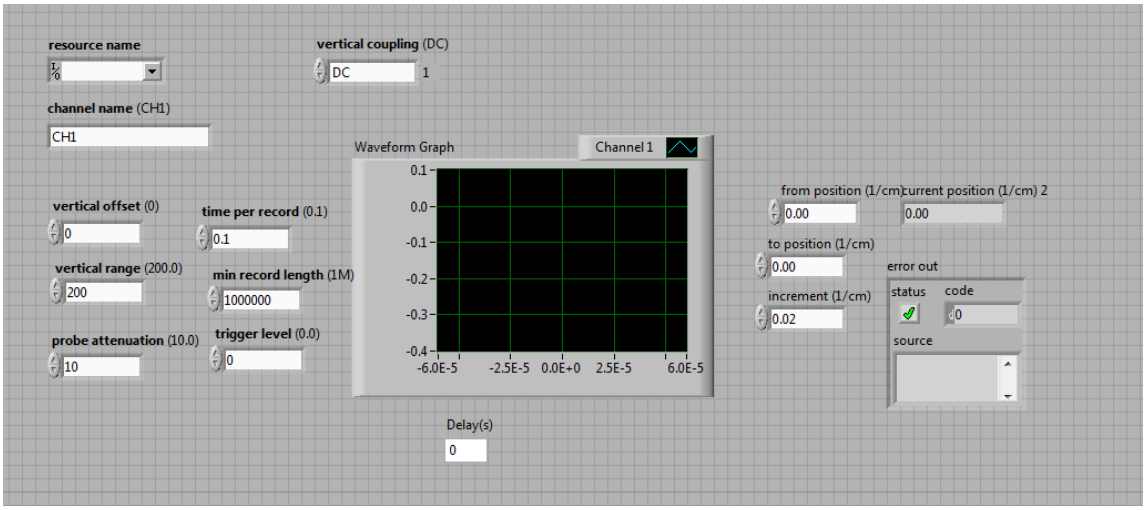

Figure 3.2: Screenshot of the LabView programme written by the author.

For each performance in LabView, the range of wavelength and the scanning increment were chosen firstly. In addition, several values for detection such as vertical offset and range, time per record, min record length, probe attenuation and trigger level were pre-set according to the experimental requirements. After an auto-measurement by the programme, a set of raw data was recorded and plotted in an Excel file.

The laser beam for LIF measurement was measured by laser beam thermal paper to be about 5 mm in diameter at the exit of the dye laser. The maximum pulse energy at 308 nm was measured to be 6 mJ by a laser power meter. A convex lens of 750 mm focal length was used to focus the laser beam directing to centre of the burner. LIF measurements of signal against laser power were firstly performed to show the experimental laser power was below the fluorescence saturation irradiance. This procedure was to ensure the measurements were performed in a linear regime in order to avoid problems arising from partial saturation effect. A system consisting of two identical 75 mm convex lenses and a pinhole 0.5 mm in diameter was employed before entering into the focusing lens in order to obtain better beam profile. The pinhole was placed between these lenses, and the distance to either side was 75 mm. The LIF experimental set-up is schematically shown in Figure 3.3.

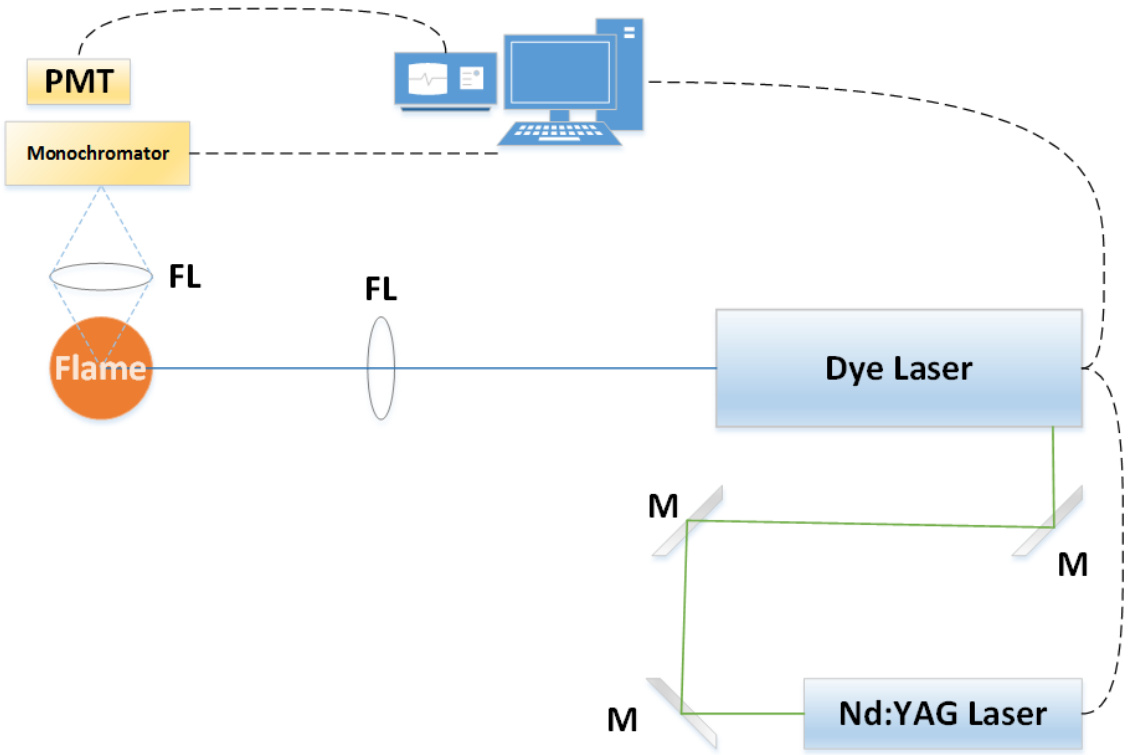

Figure 3.3: Experimental setup of LIF measurement. *PMT: photomultiplier. FL: focusing lens. M: reflecting mirror.*

Firstly, OH LIF spectra were obtained in lean flames by scanning the laser frequency at lean flames. These spectra were compared with the spectra which generated by LIFbase (Luque and Crosley, 1999) software in order to determine the different excitation lines and choose a suitable line for the following experiments. Due to the intense luminosity, soot incandescence and PAHs fluorescence, low OH concentration, attenuation of the incident beam and signal trapping, various interferences can occur in sooting flames

when employing laser diagnostics such as LIF. A series of reference measurements has also been performed in order to compensate for these interferes. The broadband absorption of soot and PAHs may significantly result to attenuation of the incident beam. Since, the intensity of laser beam is actually reduced at the detection point. Therefore, this effect reduces the fluorescence signals at that point. In addition, broadband signals due to PAHs fluorescence and LII can be rejected by performing measurements both on-resonance with the OH absorption lines and off-resonance at wavelengths 0.08 nm away from each determined excitation. Net OH LIF signals in sooting flames were thus obtained by subtracting reference (off-resonance) measurements from the at-resonance ones. The first set of reference measurement was designed by considering Beer-Lambet law. Intensity of the transmitted light is logarithmically depend on the absorption coefficient of the substance, intensity of the incident light and the distance the incident light travels through the material. The law can be written as Equation 3.1:

$$-ln\left(\frac{I}{I_0}\right) = \alpha l \qquad (3.1)$$

where I_0 is intensity of the incident light, I is intensity of the transmitted light, α is the absorption coefficient of the substance and l is the path length. In the presence of soot and PAHs, the value of α is great and not negligible. For the OH LIF measurements, the

fluorescence signal must be normalized through division by the incident laser power at the measurement point. It is thus necessary to obtain flame absorption profiles in order to calibrate the intensity of detected LIF signal at each measurement point. At the reaction zone of the flames, this is a faintly minor correction due to very weak absorption (less than 1%) observed. As the flames are symmetric and the excited points are at the middle of flame, the intensity of laser light at the centre of the flame, I_1, can be deduced from Equation 3.2 to

$$-ln\left(\frac{I}{I_0}\right) = -2ln\left(\frac{I_1}{I_0}\right) \text{ Or } I_1=\sqrt{II_0} \tag{3.2}$$

In the same way, based on assumption of similar absorption coefficient for the fluorescence and the incident light, the intensity of detected LIF signal can be calibrated to

$$I_{LIF} = \sqrt{\frac{I_{detected}^2 I_0}{I}} \tag{3.3}$$

where $\sqrt{I/I_0}$ is the fractional transmission to centre of the flame, I_{LIF} is the calibrated intensity of LIF signal, $I_{detected}$ is the intensity reading from the oscilloscope. Owing to all LIF measurements performed in linear region that will shown in the result chapter, the total calibrated LIF signal is $I_{detected}I_0/I$. Net OH LIF profiles in sooting flames were thus

obtained by subtracting reference (off-resonance) measurements from the at-resonance ones. Detailed results and discussion of this method will be shown in the next chapter.

3.5 Thermometry by LIF

Theoretically, OH LIF thermometry in flames is a well-developed technique—scanning excitation thermometry or also called Boltzmann plot method (Laurendeau, 1988). This method is on the basis of measurement of the population of lower lying energy levels. By calculating population distribution of these energy levels, local flames temperature can be deduced. According to this method, OH LIF signals are considered to simply depend on the local flame temperature and species concentrations. The laser was scanned in wavelength between 302 nm and 304 nm, while the resulting fluorescence signals were collected to deduce OH energy level populations. OH LIF spectra were firstly obtained in lean flames by scanning the laser wavelength within the (0, 0) excitation range between 302.5 nm and 304.5 nm. These spectra were compared with the spectra which generated by LIFbase (Luque and Crosley, 1999) software in order to determine the different excitation lines and choose a suitable lines for the OH LIF

thermometry. Due to the intense luminosity, soot incandescence and PAH fluorescence, low OH concentration, attenuation of the incident beam and signal trapping, various interferences can occur in sooting flames when employing laser diagnostics such as LIF. Therefore, a series of reference measurements has also been performed in order to compensate for these interferes. The first set of reference measurement was designed by considering Beer-Lambet law. Intensity of the transmitted light is logarithmically depend on the absorption coefficient of the substance, intensity of the incident light and the distance the incident light travels through the material. For the OH LIF measurements, the fluorescence signal must be normalized through division by the incident laser power at the measurement point. It is thus necessary to obtain flame absorption profiles in order to calibrate the intensity of detected LIF signal at each measurement point. As the flames are symmetric and the excitated points are at the middle of flame, the intensity of laser light at the centre of the flame can be deduced. In the same way, based on assumption of similar absorption coefficient for the fluorescence and the incident light, the intensity of detected LIF signal can be calibrated. Then, the other set of reference measurement was designed by considering PAH fluorescence and LII signals in the measurement. There are negligible signals when the laser scanned within off-resonance wavelengths range. However, due to the present of soot and PAH in sooting flames, the broadband signals of PAH fluorescence and LII are

collected both at-resonance and off-resonance wavelengths. Therefore, the off-resonance measurements were performed at the wavelength of 0.08 nm away from each determined excitation line in order to obtain all detected signals (most are PAH LIF and LII) except OH LIF. Finally, net OH LIF profiles in sooting flames were thus obtained by subtracting reference (off-resonance) measurements from the at-resonance ones. By employing this calibration method, net signals of OH fluorescence were recorded at the peak of each excitation lines between 302.5 nm and 304.5 nm in different flame conditions and location. The temperature profiles from the fluorescence signals were deduced by using Boltzmann plot method (Laurendeau, 1988)

3.6 Cavity-ring down signal detection

The CRDS experimental setup is very similar to the LIF setup. It consists of the same tunable laser source, a stable optical cavity as described in section 3.2 and a detection system, as illustrated in Figure 3.11. A Nd:YAG laser (Surelite continuum SLII-10) was used to generate 532 nm pulses with energy of 280 mJ and pulse-length of 5 ns at a repetition rate of 10 Hz. A dye laser (Sirah Cobra) was pumped by the Nd:YAG laser in order to generate tuneable radiation near 620 nm using Rhodamine 640 dye. To

perform cavity ring-down measurements an aperture of 50 microns diameter and two identical convex (diameter 1 inch, focal length 75 mm) were obtain a Gaussian beam and match approximately the TEM_{00} transverse mode of the optical cavity. The second lens focused the laser beam was focused at the centre of the optical cavity. For UV measurements (OH radical), cavity mirrors with a radius of curvature of R = 6 m ('HR 308 nm', Reflectivity 99.5%, CRD Optics Inc.) were used, while for HCO and $^1CH_2$ radicals measurements, two identical 0.8 inch diameter plano-concave mirrors with radius of curvature of R = 6 m ('HR 610 nm', Reflectivity 99.995%, CRD Optics Inc.) were employed. The distance between the mirrors was 640 mm while the burner was positioned at the centre of optical cavity. The beam waist at the centre of cavity was calculated to be 600 μm (full width at half-maximum).

Alignment of the detection system was the first step and very critical to the success of CRDS. A empirical alignment method was developed during the experimental experience with the help of Mercier and Desgroux's experience (Berden and Engeln, 2009). The alignment procedure of this CRDS application is shown step by step in Figure 3.4 - 3.9.

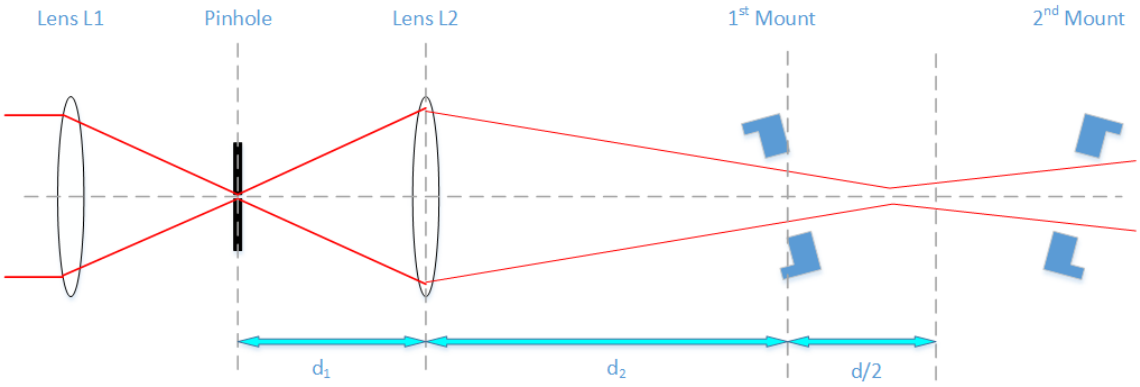

Figure 3.4: Step 1 of alignment procedure for a CRDS.

Firstly, cavity mirrors mounts are placed without the mirrors in order to enable the laser beam passing into the cavity. The mode matching optic components are placed and adjusted to the positions by following the ABCD laws discussed in detail in Section 2.6.2. The laser beam is expected to be focused before the cavity centre without the mirrors at this step. An assisting round plane that has the same diameter of the cavity mirrors and a clear mark at the centre is placed in 2nd mount. This tool can make sure the laser beam focuses at the centre of the mount and mirror later.

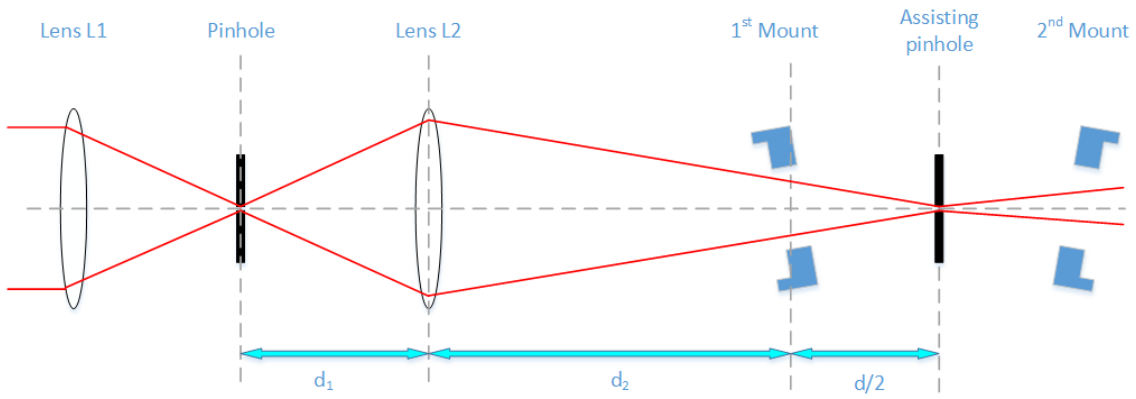

Figure 3.5: Step 2 of alignment procedure for a CRDS.

At the second step, another assisting round plane with 2 mm diameters pinhole at the centre of it is placed at the 1st mount, and an assisting pinhole with the diameters of 2 mm is placed at the centre of the cavity. Adjusting the 1st mount to make sure the laser beam passes both the first and second pinholes.

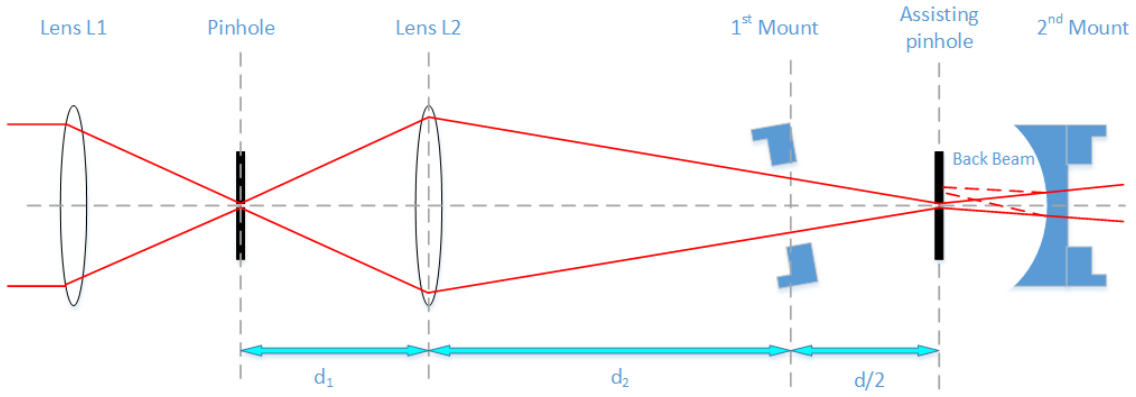

Figure 3.6: Step 3 of alignment procedure for a CRDS.

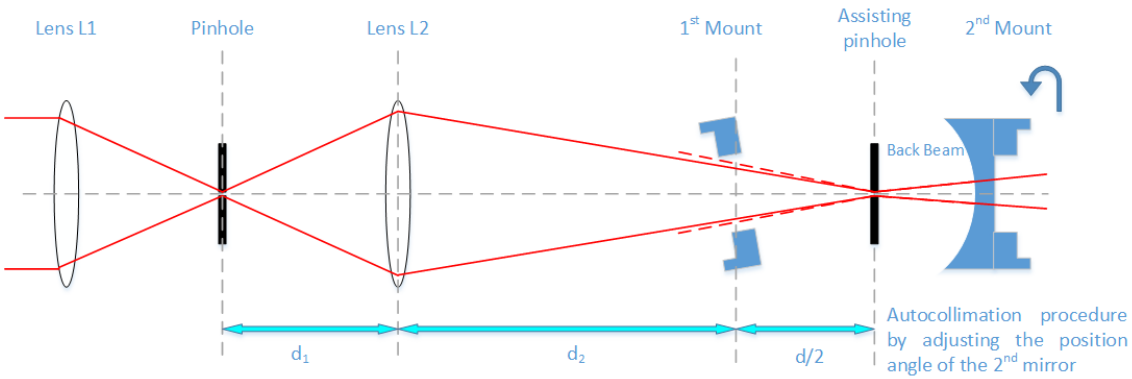

Figure 3.7: Step 4 of alignment procedure for a CRDS.

And then at the step 3 and 4, the assisting plane in the 2nd mount is replaced by the cavity mirror. Precisely adjust the 2nd mount in order to let the reflected laser beam passing the assisting pinhole at the centre of the cavity.

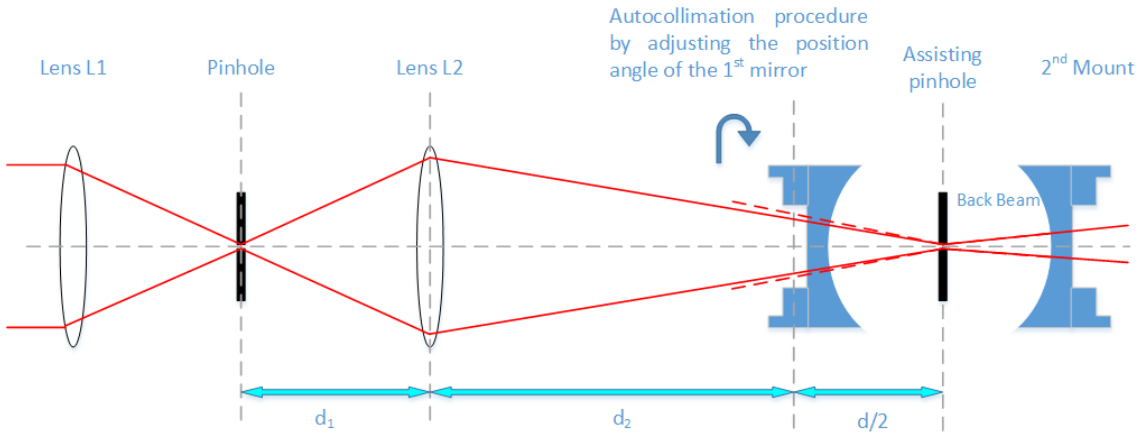

Figure 3.8: Step 5 of alignment procedure for a CRDS.

At the step 5, the assisting plane inside the 1st mirror is replaced by the cavity mirror. Precisely adjust the 1st mount in order to let both the incident and reflected laser beams passing the assisting pinhole at the centre of the cavity.

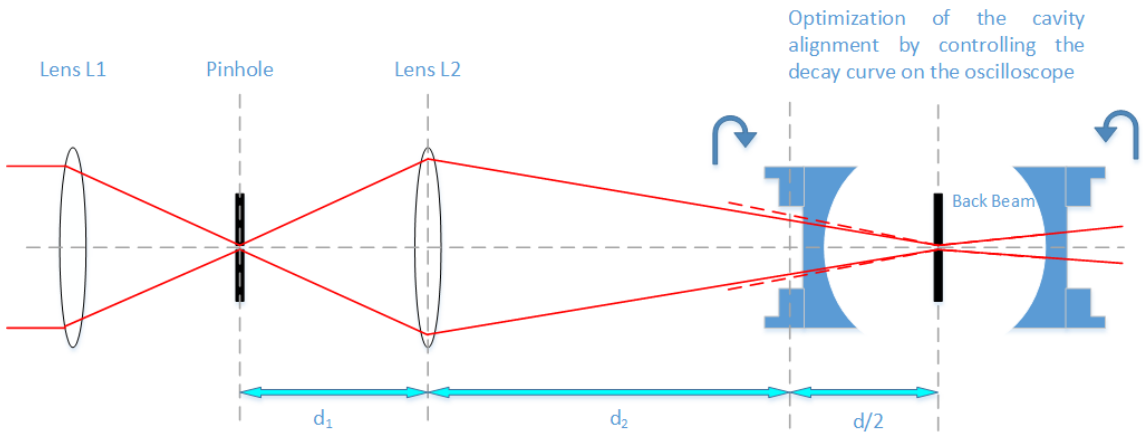

Figure 3.9: Step 6 of alignment procedure for a CRDS.

Finally, the decay time of the cavity is monitored on a digital oscilloscope and optimized in quality as well as in length. The assisting pinhole at the centre of cavity is removed for flames on. An example of the CRDS signals after the alignment is shown in Figure 3.9.

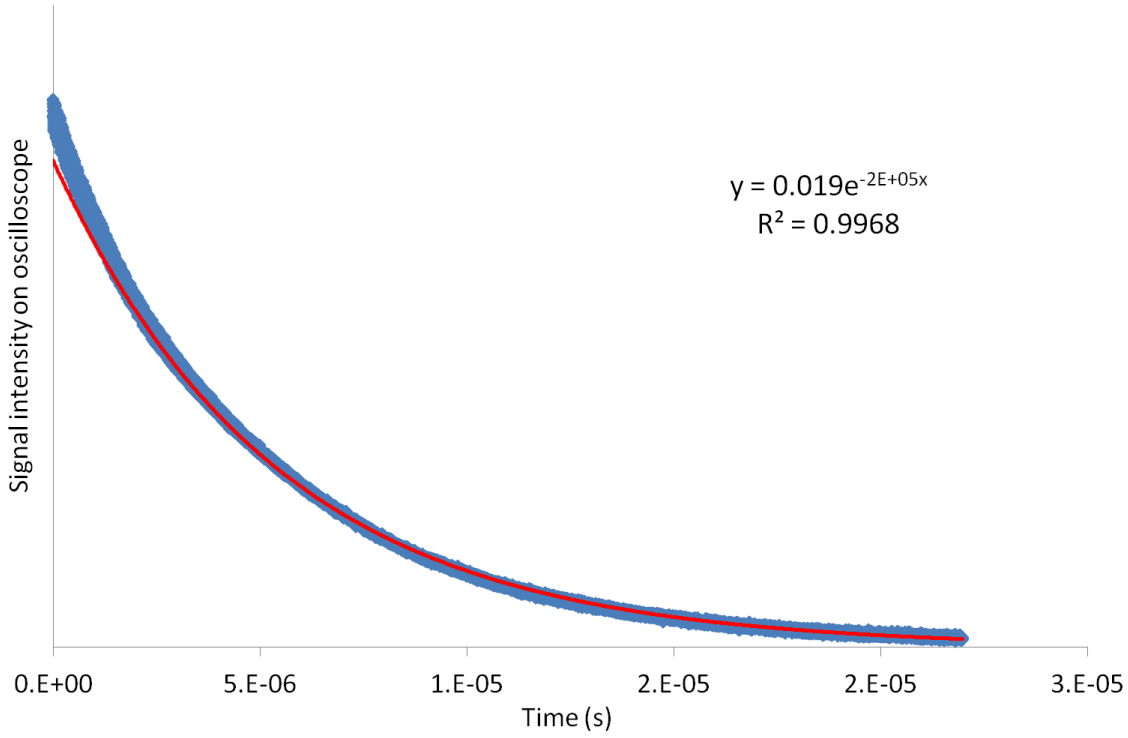

Figure 3.10: CRDS signals recorded on the digital oscilloscope after the alignment procedure with an empty cavity. *The decay signal is clear without mode beating, and the exponential fit proves the quality of the CRDS signal.*

At the detection stage, the laser beam from cavity output was passed through an aperture of 2 mm in diameter before reaching the photomultiplier tube. This aperture was fitted at the entrance of a shroud which was attached in the front of the photomultiplier tube. The use of this aperture was an aid for the alignment while the aperture-shroud device also reduced scattered laser light reaching to the photomultiplier tube. Moreover, this aid device did not degrade the CRD signals. The photomultiplier tube was also connected to the same digital oscilloscope and recorded by the personal computer. And then, averages of 128 individual ring-down events were acquired and processed to fit to exponential decays by the self-write LabView program.

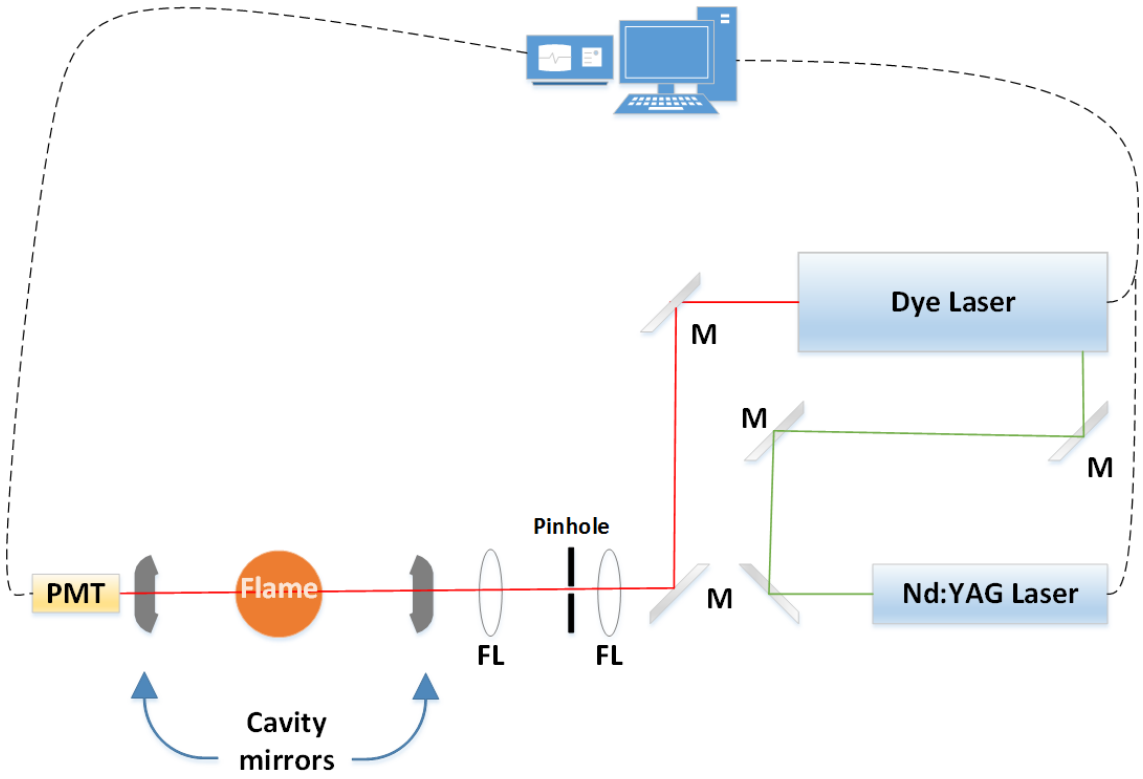

Figure 3.11: Experimental setup of CRDS measurement. *PMT: photomultiplier. FL: focusing lens. M: reflecting mirror.*

Before each series experiment, a good alignment was achieved by recording ringdown time in an empty cavity. According to the principle of CRDS technique (Okeefe and Deacon, 1988), the radical concentration is determined from the measured decay times. Written in terms of the absorption coefficient, $\alpha=\sigma C$. If τ and τ_0 (ring-down time) are experimentally recorded as functions of the laser frequency, the absorption spectrum of a sample within the cavity can be calculated using Equation 3.4.

$$\alpha = \sigma C = \frac{\Delta\tau}{\tau_0 \tau}\frac{L}{cd} = \frac{\Delta k L}{cd} \quad (3.4)$$

where $\Delta\tau=\tau_0-\tau$, and $\Delta k=(1/\tau)-(1/\tau_0)$ is the change in the ring-down rate coefficient (in s^{-1}), L is the optical cavity of length (in m), c is the light speed (in m/s), d is the burner diameter (in m), C is the radical concentration (m^{-3}) and σ is the absorption cross-section (m^2). As the result of analyzing the Equation 3.4, the concentration of a sample can be directly calculated from measured changes in the decay time in the presence and absence of the sample if the absorption cross-section of the sample is known at a particular frequency v.

The absorption cross-section for a transition $i \rightarrow k$ can be calculated by using the Equation 3.5 (Derzy et al., 1999, Hilborn, 2002)

$$B_{ik} = \frac{1}{h\nu_0}\int_0^\infty \sigma_{ik}(\nu - \nu_0)d\nu \quad (3.5)$$

which B_{ik} is given by ICLAS measurements (Derzy et al., 1999).

Following this method, CRDS absorption spectra were firstly obtained by scanning laser wavelength in increments of every 0.002 nm between 615.6 and 616.5 for HCO, and

622.1 and 622.8 for $^1CH_2$. These spectra were used to find out species excitation lines and choose suitable lines for further investigation in different flames conditions and positions. This study was focusing on sooting flames, so reference measurements should also be performed off-resonance with the excitation line in order to compensate for interference due to PAHs absorption and soot extinction. Net species concentration profiles in sooting flames were thus obtained by subtracting reference (off-resonance) measurements from the at-resonance ones. Detailed results and discussion of different species concentration profiles will be shown in the next chapter.

3.7 Chapter summary

A flat flame burner produces an approximately flat front, and therefore can be considered as a one-dimensional process to a first approximation. Mixtures of C_2H_4 and air with different fuel equivalence ratios have been chosen in order to produce sooting flame on this flat burner. The sooting flames are stablised on a flat flame burner at atmospheric pressure. The laser system consists of a Nd:YAG laser pumping a dye laser. The fluorescence was collected by a signal collection lens onto a detector (photomultiplier) equipped with a two-glass filter or a monochromator. The CRDS

experimental setup was very similar with LIF setup. It consists of a tunable laser source, a stable optical cavity and a detection system. Two different sets of cavity mirrors have been adopted depending on the investigated species. As for studying sooting flames, quantitative laser measurement was made difficult by the presence of soot particles and PAHs, which can also absorb or scatter the incident laser light. Therefore, reference measurements have been performed in order to compensate for these interferes in both LIF and CRDS techniques. Results obtaining by the described laser diagnostic techniques here will support the development and validation of models to predict PAHs and particle formation in order to reduce combustion exhaust pollution.

CHAPTER 4: LIF EXPERIMENTAL RESULTS, CALIBRATIONS AND DISCUSSION

This chapter reports on the results obtained from LIF experiments. At first, OH LIF linear regime has been confirmed to ensure all of the LIF experimental work not saturated. And then, spectra have been obtained by exciting bands in the ranges 282.8 - 284 nm and 302.5 - 304.5 nm respectively. Low OH concentration, attenuation of the incident beam and signal trapping, various interferences were occurring in sooting flames when employing laser diagnostics. Because there is much more intense luminosity, and broadband soot incandescence and PAH fluorescence signals when soot present in flames. In sooting flames, quantitative laser measurements of OH is made difficult by the presence of soot particles and PAHs, which can also absorb or scatter the broadband incident laser light. Therefore, reference measurements have been performed in order to compensate for these interferences. Moreover, efforts have been made to get a detailed flame horizontal profile in order to check how flat the flames are. The OH spectrum was measured by scanning a dye laser along rotational transitions. I_{LIF} are the relative OH fluorescence signals collected by at each peak line of S_{21} (*N = 5, 6, 7, 8, 9, 10, 11*). In order to obtain detailed temperature profiles in these sooting flames, the on- and off- resonance measurement procedure was followed. The net OH LIF

profiles in sooting flames were thus obtained by subtracting reference (off-resonance) measurements from the on-resonance ones. The temperature profiles from the fluorescence signals were determined for different flame conditions.

4.1 OH LIF spectra

OH LIF spectra we firstly obtained in lean flames of fuel equivalence ratio 0.7 at 2 mm above the burner surface by scanning the laser frequency. This was intended for laser wavelength calibration and selecting which excitation lines to probe. Each point of the measurements is averaged from 64 laser shots, and the experimental spectra are reproducible (± 10%) from 3 repetitions measurement. These spectra are compared with the spectra which generated by LIFbase (Luque and Crosley, 1999) software in order to determine the different excitation lines and choose a suitable lines for the following experiments. Both $A^2\sum(v^{'}=0) \leftarrow X^2\prod(v^{''}=0)$ and $A^2\sum(v^{'}=1) \leftarrow X^2\prod(v^{''}=0)$ bands are probed by LIF using excitation wavelengths in the ranges 282.8 - 284 nm and 302.5 - 304.5 nm respectively.

Shown in Figure 4.1 is an experimental spectrum of the (1, 0) OH band recorded at 2 mm above the burner in a C_2H_4-air flame with fuel equivalence ratio of 0.7. Also shown is a spectrum generated by the LIFbase software for OH at a temperature of 1700 K. The temperature as the key input in LIFbase has been varied to obtain good agreement with the relative linestrengths in the experimental spectrum. The experimental spectra have been shifted by 0.194 nm with respect to the theoretical one to compensate for an offset in the wavelength calibration of the laser. Both simulated and experimental spectra are on a relative intensity scale and are normalized to have the same maximum. A good agreement (line positions and relative linestrengths and location) can be found between the experimental and simulated spectra. The spacing of the experimental measurements was that a data point will not usually coincide precisely with the peak of each spectral line. There are several strong lines (such as Q_1 (6), Q_2 (5) and Q_1 (9)) in this region of the (1, 0) band. The strongest absorption line at 282.93 nm was defined by LIFBASE to be Q_1 (6) excitation.

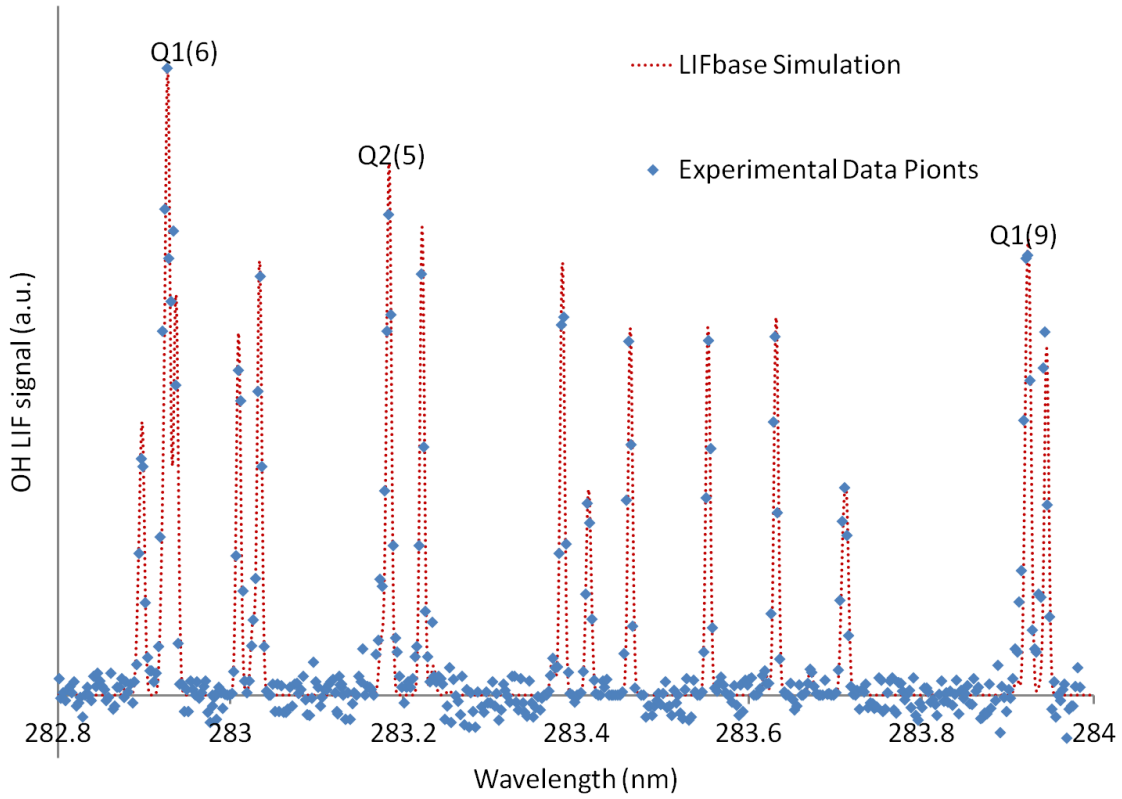

Figure 4.1: Comparison of experimental OH LIF spectra for (1-0) excitation and LIFBASE-simulations. *The theoretical spectrum has been normalized to have the same maximum as the experimental one.*

The dye laser was pumped by the pulsed laser in order to produce tuneable wavelengths around 283 with doubling crystal with the dye of Rhodamine 610. However, for probing the (0, 0) OH band, the wavelength range of this dye is not suitable. Therefore, we replaced Rhodamine 610 by Rhodamine 640 in order to access the suitable wavelength range in the following experiments. Shown in Figure 4.2 is an

experimental spectrum of the (0, 0) OH band at 2 mm above the burner under the same flame conditions. Also shown is a spectrum generated by the LIFbase software for OH at a temperature of 1700 K. The experimental spectra have been shifted by 0.186 nm with respect to the theoretical one to compensate for an offset in the wavelength calibration of the laser. The shifted distance is different as the last one due to the new dye as well as the different wavelength range. Again the spectra have been normalised. A very good agreement (linepositions and relative linestrengths and location) also can be found between the experimental and simulated spectra. The excitation lines of S_{21} defined by LIFbase are also shown in the Figure 4.2. It is clear that (0, 0) band of OH has better isolated rotational lines than the (1, 0) band. The (0-0) excitation is preferred in this experiment to the others in order to get strong and well-isolated rotational lines (Andresen et al., 1988) (which is very important for OH LIF thermometry purpose) to measure.

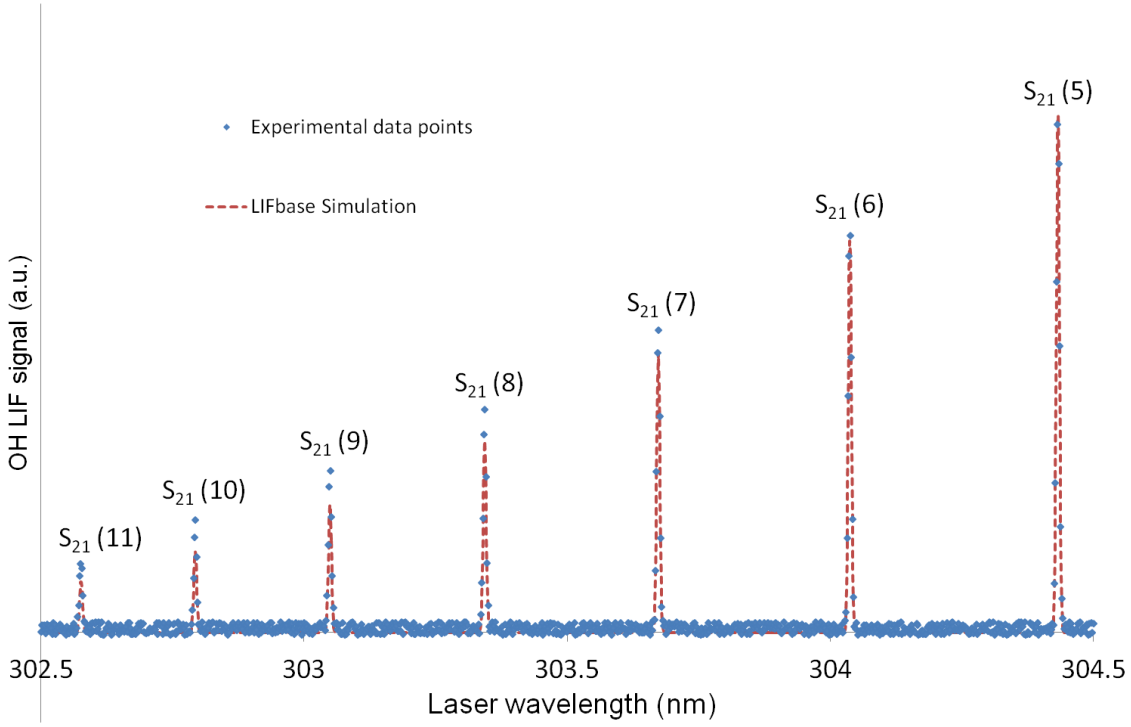

Figure 4.2: Comparison of experimental OH LIF spectra for (0-0) excitation and LIFBASE-simulations. *The theoretical spectrum has been normalized to have the same maximum as the experimental one.*

4.2 OH LIF measurement and their calibration in sooting flames

Firstly, efforts should be made to check the linearity of the OH LIF signal with respect to laser irradiance in order to make sure that the measurements are performed within the

linear regime. The Nd:YAG laser (Surelite continuum SLII-10) is used to generate 532 nm pulses with energy of 280 mJ delivered in 6 nanoseconds at repetition rates of 10 Hz and the linewidth of 1 cm^{-1} (Surelite continuum SLII-10 Manual). The dye laser (Sirah Cobra) is pumped by the pulsed laser in order to produce tuneable wavelengths around 308 nm and the linewidth of 0.1 cm^{-1}. Figure 4.3 shows the dependence of the relative fluorescence intensity by exciting the $S_{21}(5)$ and $Q_1(6)$ lines on the laser power for the flame of fuel equivalence ratio = 0.7 and at 2 mm above the burner surface. The diameters of the laser beams at the measurement volumes were 5 mm and 0.015 mm for (1-0) and (0-0) excitation. The laser beam energy is measured by a thermal laser power meter. The linear regime is demonstrated to extend at least up to at least 6.7 mJ/pulse. Therefore, all the following experiments were performed at the power of 4.5 mJ/pulse since laser dye solution decomposition would tend to weaken the maximum laser power during the experiment period. Before every measurement, the laser power has been checked by the laser power meter. The measurements were normalised by the simultaneously recorded laser power. This chosen power can make sure that all of the following experiments were performed at the same laser power during the experiment period.

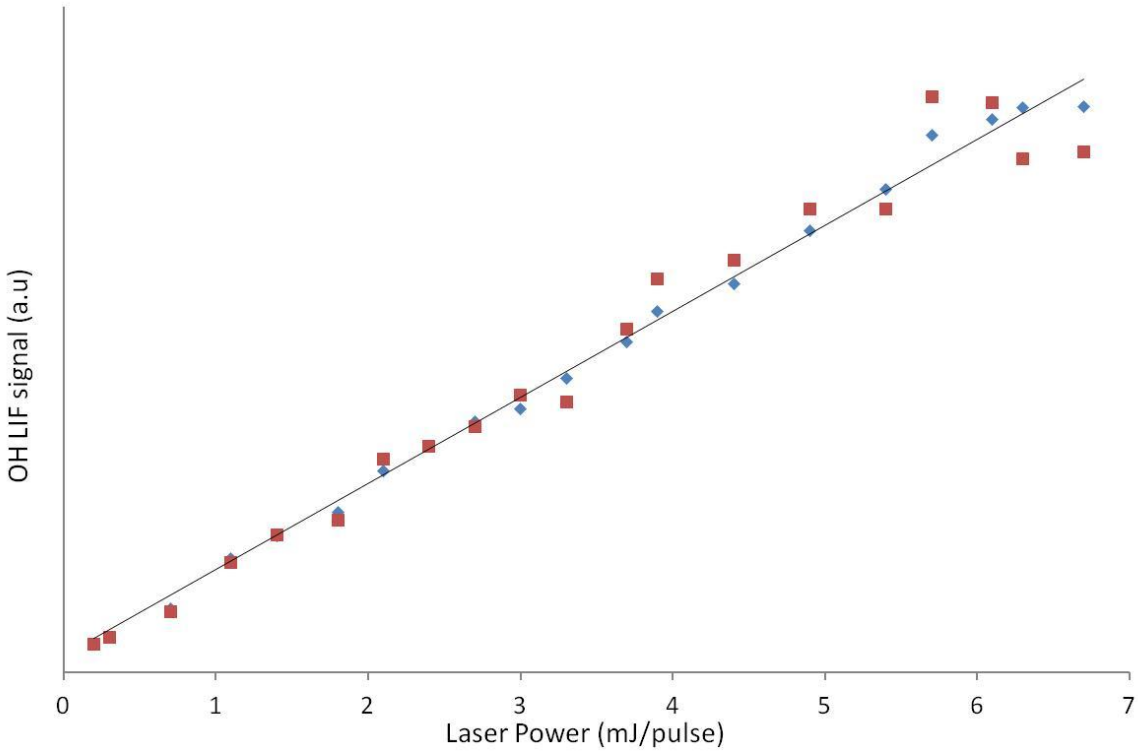

Figure 4.3: Fluorescence intensity with three individual measurements VS the laser power.

Attenuation of the incident beam, signal trapping and various other interferences can occur in sooting flames when employing laser diagnostics such as LIF. Interference due to intense broadband soot incandescence and PAH fluorescence signals are significant in rich flames, which are also characterised as low OH concentration. A lot of studies have reported OH LIF measurements in non-sooting flames; however relatively few e.g. (Nygren et al., 2001, Burns et al., 2011, Chan et al., 2011) have involved OH florescence

measurement in sooting flames. In two separate experiments, spatially-resolved profiles of OH LIF were obtained by exciting both the $S_{21}(5)$ and $Q_1(6)$ resonance lines. In sooting flames, quantitative laser measurements of OH is made difficult by the presence of soot particles and PAHs, which can also absorb or scatter the incident laser light. Therefore, reference measurements have been performed in order to compensate for these interferences.

According to Beer–Lambert law, intensity of the transmitted light is related to the absorption coefficient of the sample, the intensity of the incident light and the distance the incident light travels through the material. The law can be written as Equation 4.1:

$$-ln\left(\frac{I}{I_0}\right) = \alpha l \qquad (4.1)$$

where I_0 is intensity of the incident light, I is intensity of the transmitted light, α is the absorption coefficient of the substance and l is the path length. Both I_0 and I are measured by the laser power meter. In the presence of soot and PAH, the value of α is not negligible. Because this LIF is a point measurement technique, the fluorescence signal must be normalized through division by the incident laser power. It is thus necessary to obtain flame absorption profiles (as shown in Figure 4.4) in order to calibrate the intensity of detected LIF signal at each measurement point.

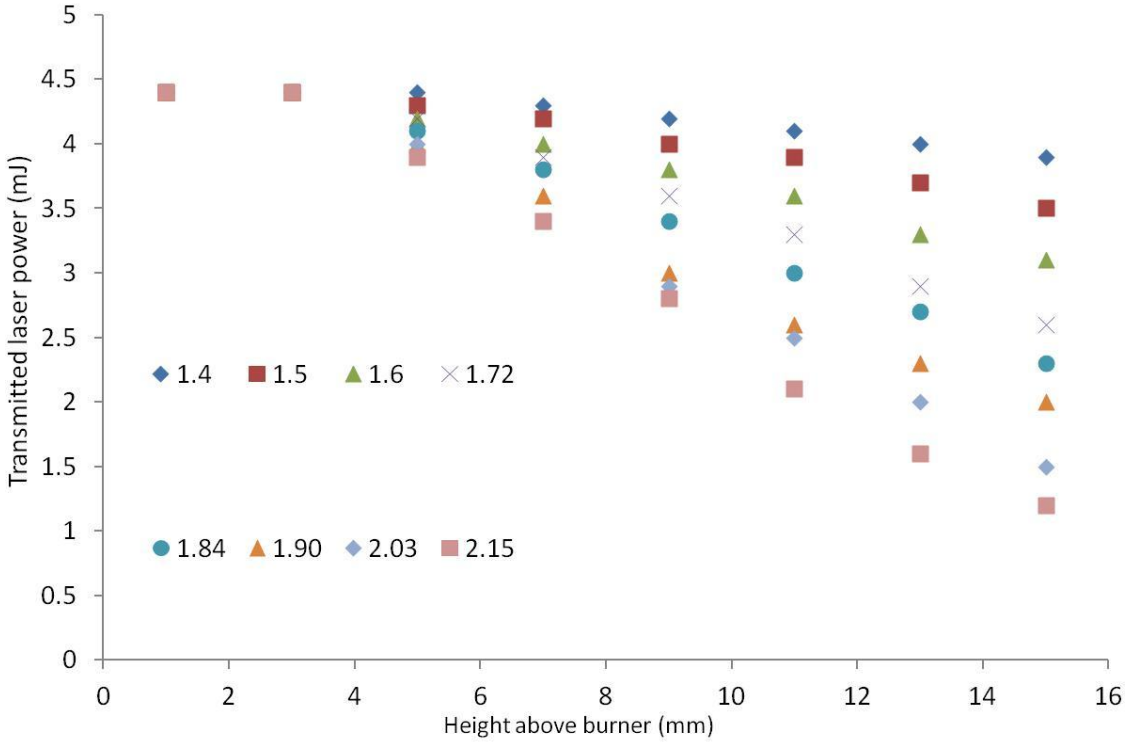

Figure 4.4: Laser absorption profiles VS height above the burner surface and fuel equivalence ratios at $Q_1(6)$ line.

As the flames are symmetric and the excited points are at the middle of flame, the intensity of laser light at the measurement volume, I_1, can be deduced from Equation 4.1.

$$-ln\left(\frac{I}{I_0}\right)\frac{l}{2} = \alpha\frac{l}{2} = -ln\left(\frac{I_1}{I_0}\right) \quad (4.2)$$

This applies to measurements recorded at the centre line of the burner.

Or written as

$$I_I = \sqrt{I I_0} \tag{4.3}$$

The detected signal must also be corrected for the effects of broadband absorption by soot and PAH. Since the detection wavelength is similar to the excitation wavelength, we assume that the fractional attenuation of the signal at a given height above the burner is equal to the fractional absorption of the incident laser light. On this basis, the intensity of detected LIF signal can be corrected in the following way:

$$-ln\left(\frac{I_{detected}}{I_{LIF}}\right) = \alpha\frac{l}{2} = -\frac{1}{2}ln\left(\frac{I}{I_0}\right) \tag{4.4}$$

$$\text{So } I_{LIF} = \sqrt{\frac{I_{detected}^2 I_0}{I}} \tag{4.5}$$

where I_{LIF} is the signal that would be recorded in the absence of signal trapping and $I_{detected}$ is the true signal. Since all the LIF measurements were performed in linear regime, the intensity of fluorescence is proportional to the intensity of laser light at the measurement volume. Thus the normalised LIF signal after alimentation of the absorption interference can be deduced as:

$$\frac{I_t}{I_{LIF}} = \frac{I_0}{I_1} = \frac{I_0}{\sqrt{II_0}} \quad (4.6)$$

Therefore,

$$I_t = \frac{I_{detected} I_0}{I} \quad (4.7)$$

Thus, the normalised LIF signal is calculated through division of the raw (background subtracted) signal by the laser energy transmitted through the flame and multiplied by the intensity of the laser beam.

As well as background subtraction and correction for laser absorption and signal trapping, interference due to PAH fluorescence and LII must also be corrected for. This was done by performing measurements on-resonance with the narrow OH line and off-resonance. Figure 4.5 shows the on-resonance signal generated by exciting the $Q_1(6)$ line. Off-resonance profiles (Figure 4.6) were subtracted from the corrected on-resonance ones in order to get the net LIF profiles demonstrated in Figure 4.7. It should be noted that these LIF measurements on the $Q_1(6)$ line have somewhat limited spatial resolution, since they were performed using an unfocused dye laser beam with a

Gaussian spatial profile and width of about 5 mm. The signal was collected by imaging onto a pinhole with a diameter of 0.6 mm.

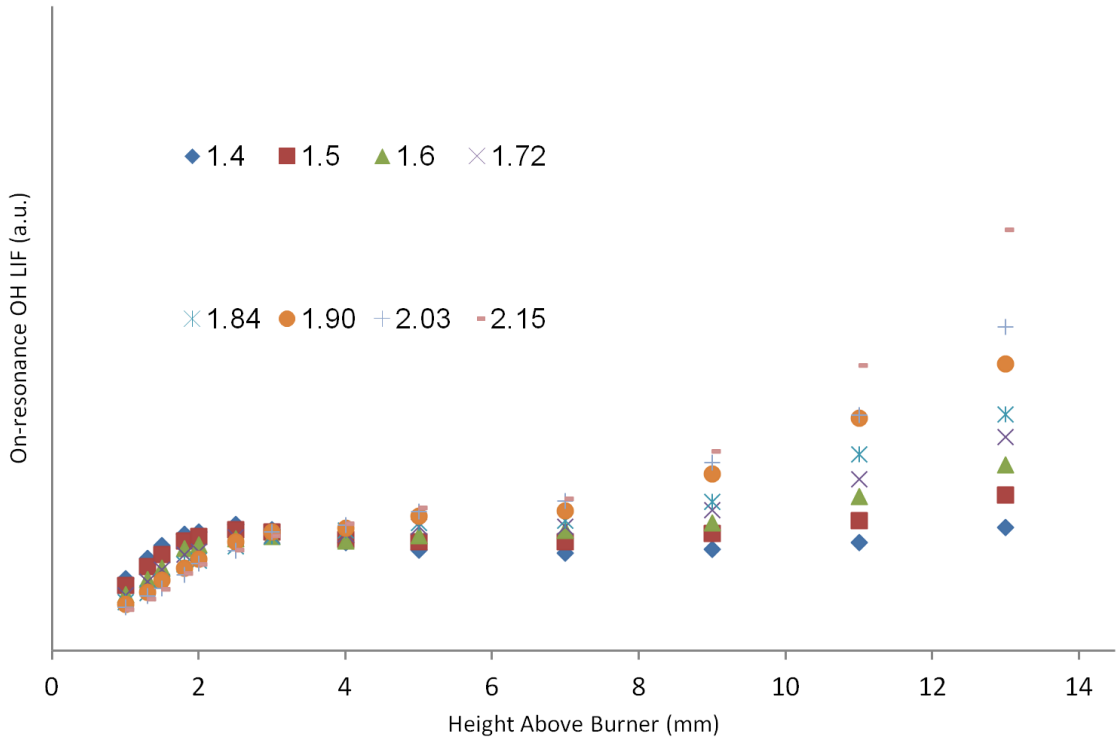

Figure 4.5: Fluorescence intensity upon excitation of the $Q_1(6)$ line for on-resonance excitation line against height above the burner surface for a range of fuel equivalence ratios.

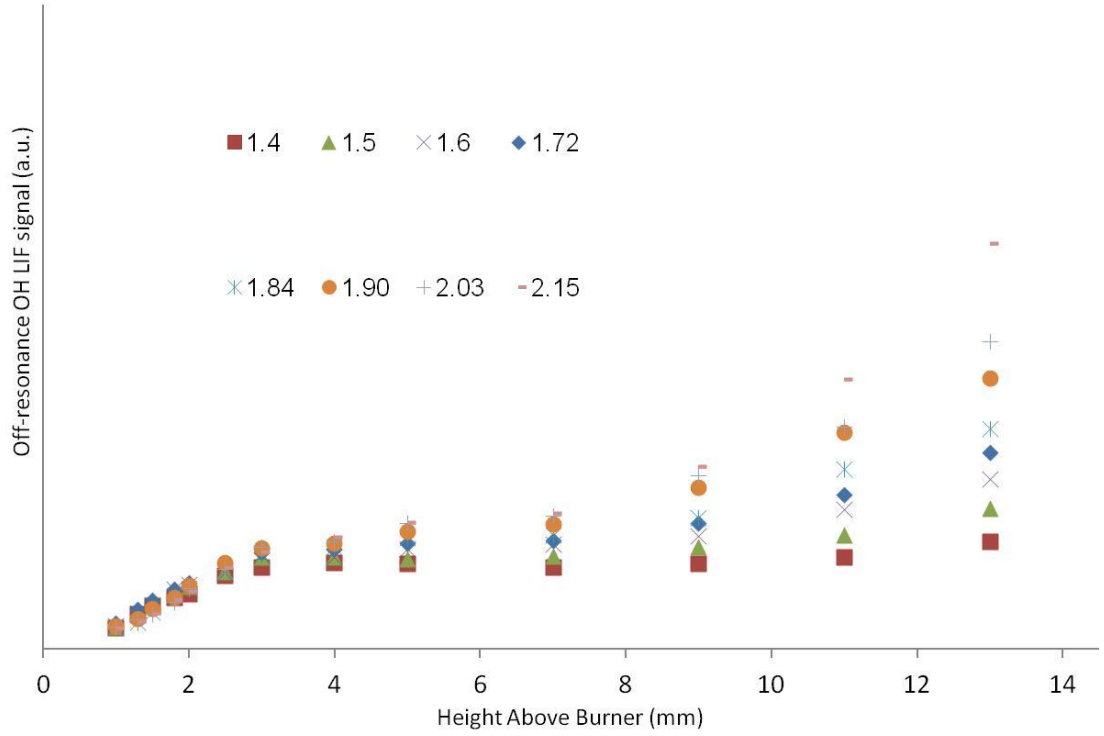

Figure 4.6: Fluorescence intensity for off-resonance excitation line ($Q_1(6)$) VS height above the burner surface and fuel equivalence ratios.

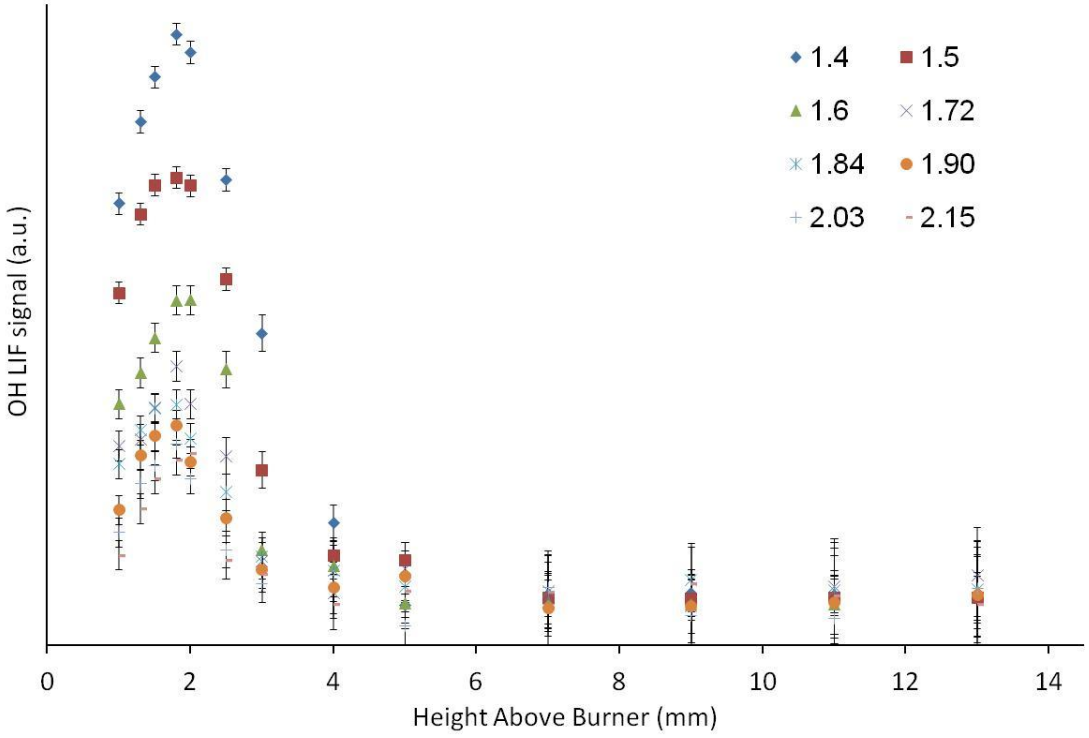

Figure 4.7: Net OH LIF profiles VS height above the burner surface for a range of fuel equivalence ratios by exciting $Q_1(6)$ line.

Figure 4.7 represents the dependence of the net OH fluorescence intensity on the height above the burner surface with different fuel equivalence ratios. The error bars are based on 3 repetitions measurement. The net OH fluorescence intensity increases and then decreases to a stable value with increasing height. Such behaviour would be expected, as there are hundreds of chemical reactions in a flame while these reactions take place in different zones. This steep rise in OH radical concentration is well-known to be a marker of flame front location. The OH is consumed downstream of the reaction

zero and the decrease in concentration is most pronounced in fuel-rich flames. From this experiment, we can explain that the more OH radical is formed than consumed in the zone between 0 mm and 2 mm while less OH radical is formed than consumed in the zone after 2 mm, and the highest OH concentration in sooting flames is at about 2 mm above the burner surface. However, as the first experiment during this work, these figures also indicate that the laser beam spatial resolution may not be sufficient to fully resolve the steep gradients due to unfocused laser beam.

Thus, later experiments employed a focusing lens to improve the spatial resolution which has already have described in the experimental setup chapter. Due to the lack of 283 nm CRDS mirrors and access to 308 nm CRDS mirrors, the focused OH measurements were adjusted to the probe of S_{21} excitation line around 308 nm. Background substraction and normalization was done as described previously. Another important reason for this adjustment is due to the flexibility and compatibility for 622 nm CRDS measurements of HCO and $^{1}CH_2$.

Shown in Figure 4.8 are on-resonance signals recorded at the $S_{21}(6)$ line. Background subtraction and normalisation were done as described previously Off-resonance

profiles (Figure 4.9) were subtracted from the corrected on-resonance ones in order to get the net LIF profiles demonstrated in Figure 4.10.

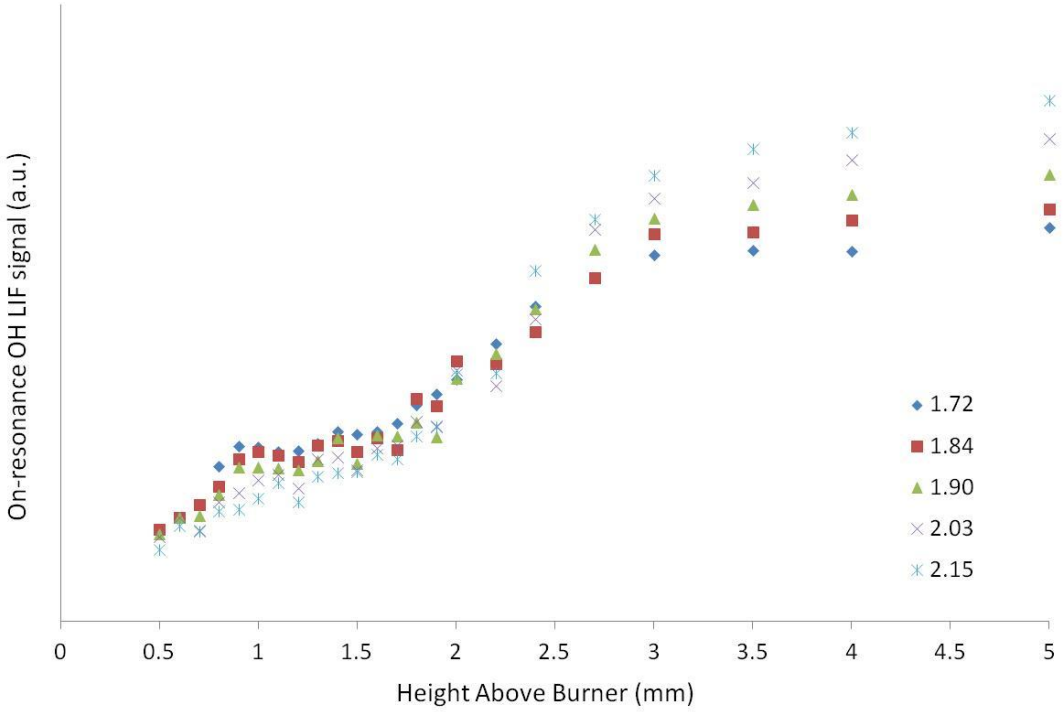

Figure 4.8: Fluorescence intensity upon excitation of the $S_{21}(6)$ line for on-resonance excitation line against height above the burner surface for a range of fuel equivalence ratios.

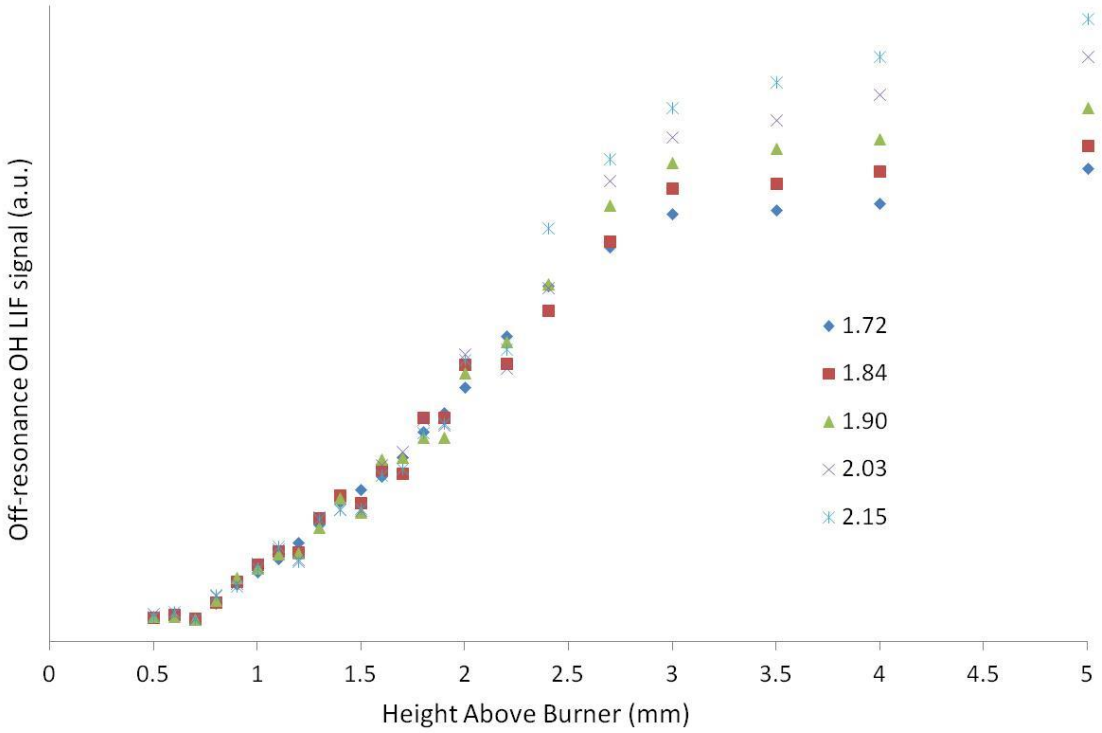

Figure 4.9: Fluorescence intensity for off-resonance excitation line VS height above the burner surface for a range of fuel equivalence ratios.

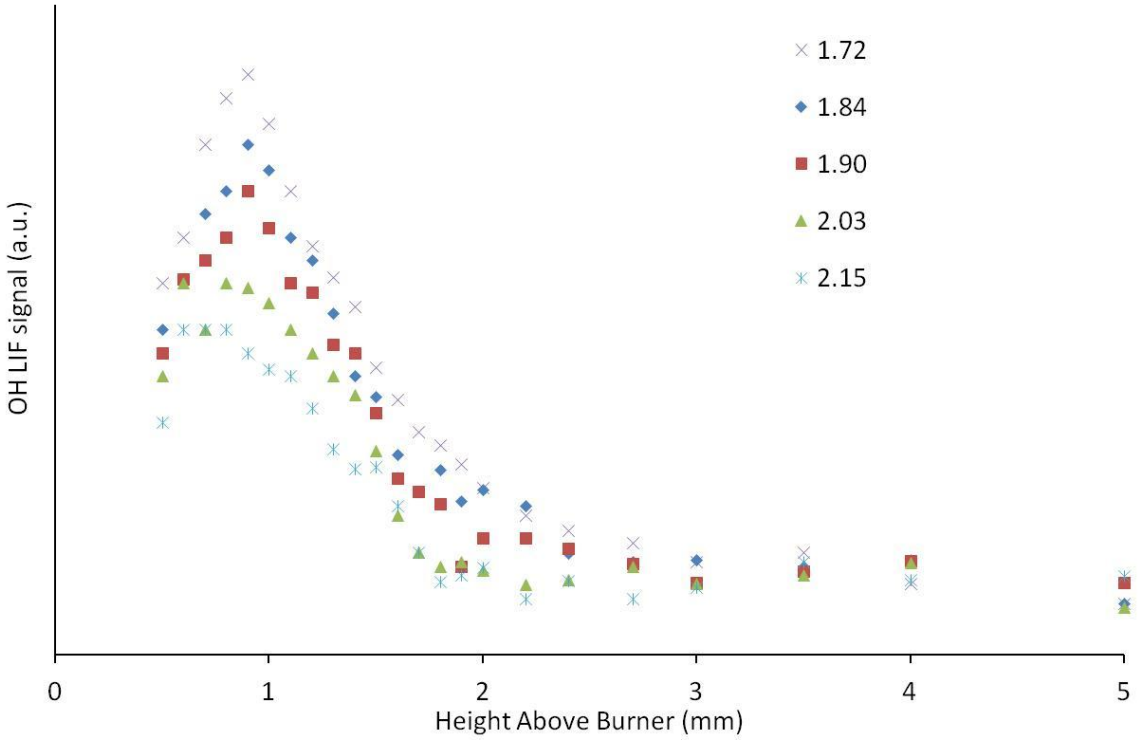

Figure 4.10: Net OH LIF profiles VS height above the burner surface and fuel equivalence ratios by exciting $S_{21}(6)$ line.

Figure 4.10 represents the dependence of the net OH fluorescence intensity on the height above the burner surface with different fuel equivalence ratios. These graphs show that better spatial resolution was achieved and the closest measurement position is down to 0.5 mm above the burner surface with the narrower beam waist. The width (FWHM) of the OH profile also seems to be about half of what is obtained from the preliminary data recorded for $Q_1(6)$ line. The profiles are similar as the ones detected by $Q_1(6)$ excitation lines. The net OH fluorescence intensity increases to its maximum at

1.1 mm and then decreases to a stable value with the height increases. These relative profiles will be calibrated to the absolute values by CRDS below, as well as being compared to model prediction

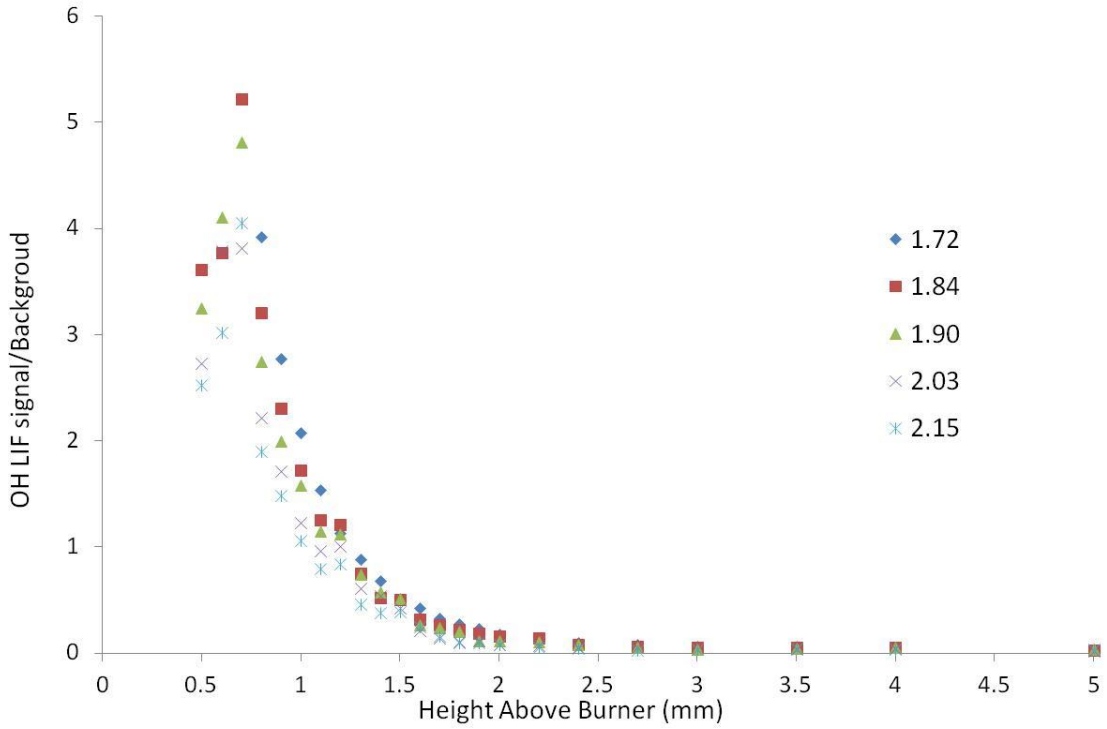

Figure 4.11: Ratio of intensity of net OH LIF over total off-resonance signals VS the height above burner surface and fuel equivalence ratio.

Figure 4.11 represents the dependence of ratio of intensity of net OH LIF over total off-resonance signals on the height above burner surface and fuel equivalence ratio. It is obvious that the ratio decreases with increasing of fuel equivalence ratio and height

above burner surface. Due to this reason of low proportional OH LIF against background signals, longer time average detection of 64 laser shots has been performed in order to reduce measurement errors.

A flat flame burner can be approximated as a one-dimensional process. The flame velocity decreases when it moves closer to the burner, because there is a steeper temperature gradient and therefore greater heat loss to the burner surface. It therefore stabilizes at the distance where the gas flow velocity and the flame propagation velocity are equal. In order to check how flat the flames are, efforts have been made to get a detailed flame horizontal profile. Due to the same reasons of low OH concentration, and various interferences occurring in sooting flames, on- and off- measurement procedures are followed as well in these horizontal profile measurements. As shown in Figure 4.12, LIF experiments were performed at $Q_1(6)$ excitation line, fuel equivalence ratio = 2.15 and different positions of height above burner. Off-resonance profiles shown in Figure 4.13 were subtracted from the corrected on-resonance ones in order to get the net LIF profiles demonstrated in Figure 4.14. The net OH LIF signal increases at the edges of the flame from 2.2 mm above the burner surface. This can be explained by the idea that unburned fuel reacts with the ambient air at the edges of flame, which causes increased OH concentration. However, it also proves that flame horizontal region

remains to be about 16 mm radius up to 2.1 mm above the burner surface which agrees with our burner surface dimensions.

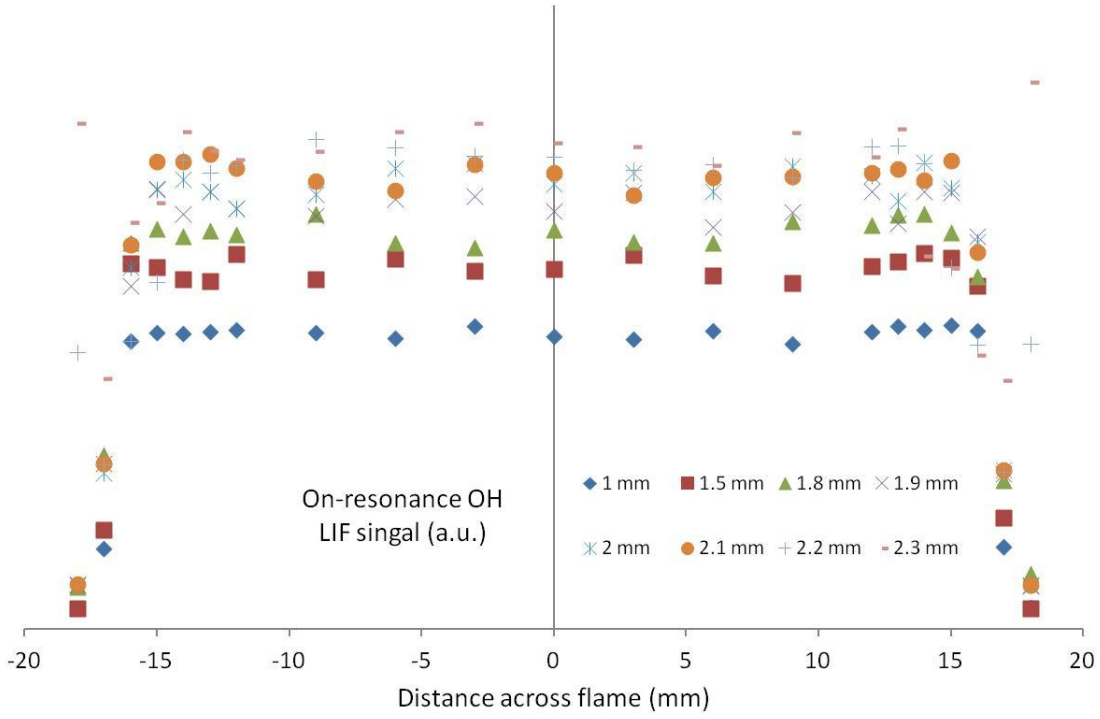

Figure 4.12: Horizontal fluorescence intensity upon excitation of the $S_{21}(6)$ line for on-resonance excitation line against distance across flame at different heights above the burner surface at the fuel equivalence ratio = 2.15.

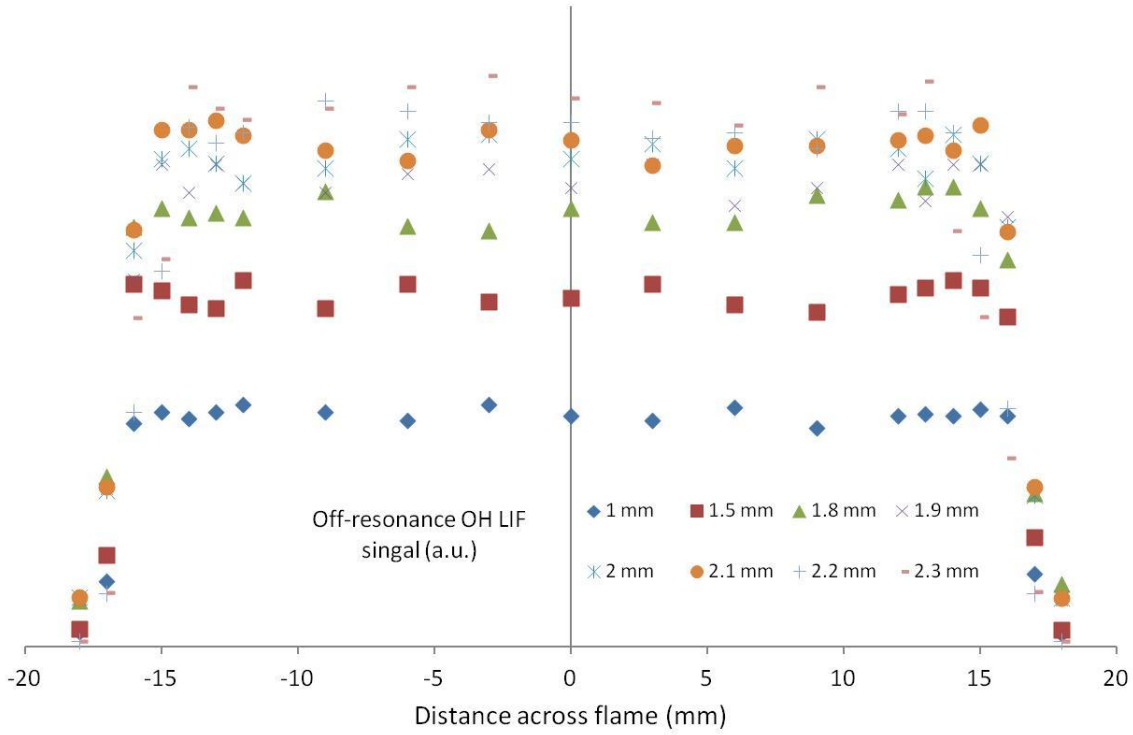

Figure 4.13: Horizontal fluorescence intensity off excitation of the $S_{21}(6)$ line for off-resonance excitation line against distance across flame at different heights above the burner surface at the fuel equivalence ratio = 2.15.

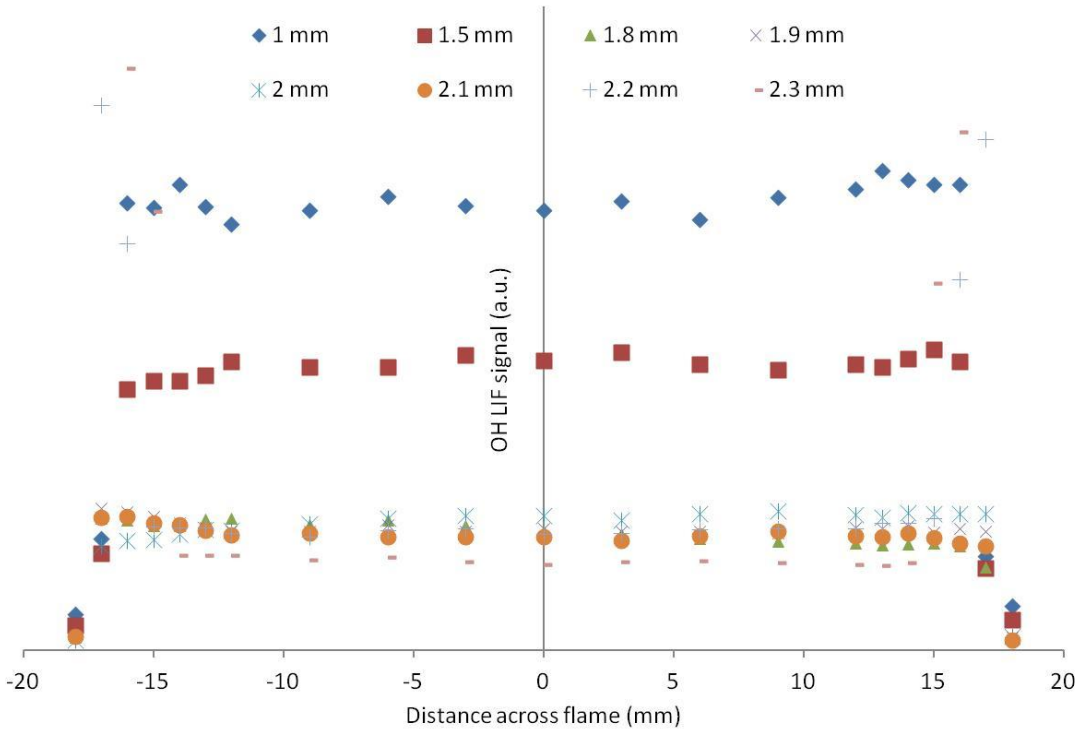

Figure 4.14: Horizontal net fluorescence intensity of OH LIF against distance across flame at different heights above the burner surface at the fuel equivalence ratio = 2.15.

4.3 OH LIF Thermometry

As discussed in Chapter 2, flame temperature is a critical flame parameter due to its crucial influence on chemical reaction rates. Moreover, absolute values of all measured concentration profiles will be directly influenced by uncertainties of their temperature determination. In this work, absolute number densities in the ground state of the

probed transitions are determined by CRDS, and then these values need to be converted to total mole fractions in order to compare with the results of flame modelling. The temperature determination is linearly affecting this procedure by the ideal-gas law. Moreover, the population of a certain rotational level in a molecule is influenced by temperature. This is also the main reason to choose temperature insensitive lines when considering the concentration measurements of $^{1}CH_2$ and HCO reported below. In addition, the temperature affects on the population of a molecule can be compensated if the temperature profile for the flames is known. Even if the temperature profile is off by 100 K, the error introduced over the partition function would sometimes be negligible (Schocker et al., 2005).

Due to the nature of OH LIF thermometry as reviewed in Chapter 2, the technique is only practical when sufficient OH fluorescence signals can be detected. In this case, due to lower OH fluorescence signal, it was not possible to perform the measurements below 0.6 mm above the burner surface.

The principle of OH LIF thermometry by Boltzmann plotting method has already been discussed in Chapter 2. In the case of LIF the spectrum is measured by scanning a dye

laser along rotational transitions. The fluorescence signal is a broadband signal. LIF is a two-step process: first a photon is absorbed, followed by emission from the excited level. The intensity I_{LIF} of a line of transition *i* can be written as (Santoro and Shaddix, 2002),

$$I_{LIF} \propto \frac{A_{v'}^{v''}}{Q+\sum_{v''} A_{v'}^{v''}} B_i(2J_i+1)e^{-\frac{E_i}{kT}} \quad (4.8)$$

where B_i is the Einstein absorption coefficient for transition *i*, induced by the laser. $A_{v'}^{v''}$ is the Einstein emission coefficient for the detected vibrational transition, divided by the sum over all vibrational states, plus the quenching coefficient *Q*. Since this *A* coefficient is independent of the transition *i*, the equation can be reduced to,

$$I_{LIF} \propto B_i(2J_i+1)e^{-\frac{E_i}{kT}} \quad (4.9)$$

This equation is valid if: 1. The laser intensity is low and there is no saturation, i.e. stimulated emission can be neglected; 2. Vibrational energy transfer is negligible, or at least independent of the rotational state; 3. Rotational energy transfer is faster than the lifetime of the excited state, such that there is a redistribution of the rotational levels of the excited state; 4. Quenching is independent of the rotational state.

Finally, the equation can be written in this work as

$$\ln \frac{I_{LIF}}{B_i g_i} = -\frac{1}{T}\frac{E_i}{k} + constant \quad (4.10)$$

Discuss of this method in our situation:

1. By taking many lines, the accuracy can be increased and the influence of an occasional bad line (blends or otherwise defective) eliminated. 7 lines of S_{21} (*N = 5, 6, 7, 8, 9, 10, 11*) were included in this work to obtain the slope.

2. A check is obtained in each case on whether rotational temperature equilibrium exists. This is so if actually a straight line is obtained. If the plot is not a straight line, this may be due to no equilibrium in source, influence of self-absorption or continuous background or temperature gradients at the measured point.

3. The species properties are necessary to this method. As for OH in this work, it has been well-studied for several decades, and all necessary properties can be found in LIFbase (Luque and Crosley, 1999) and in the works of Dieke and Crosswhite (Dieke and Crosswhite, 1962).

Figure 4.2 shows an example of a LIF spectrum of OH. To determine the rotational temperature we applied the fitting method described above. I_{LIF} are the relative OH fluorescence signals collected by the same detection system at each peak line of S_{21} (*N = 5, 6, 7, 8, 9, 10, 11*). *E (N)* (Dieke and Crosswhite, 1962) are excitated energies of each peak line of S_{21}. After the fitting as shown in Figure 4.15, the temperature can be determined from the slope.

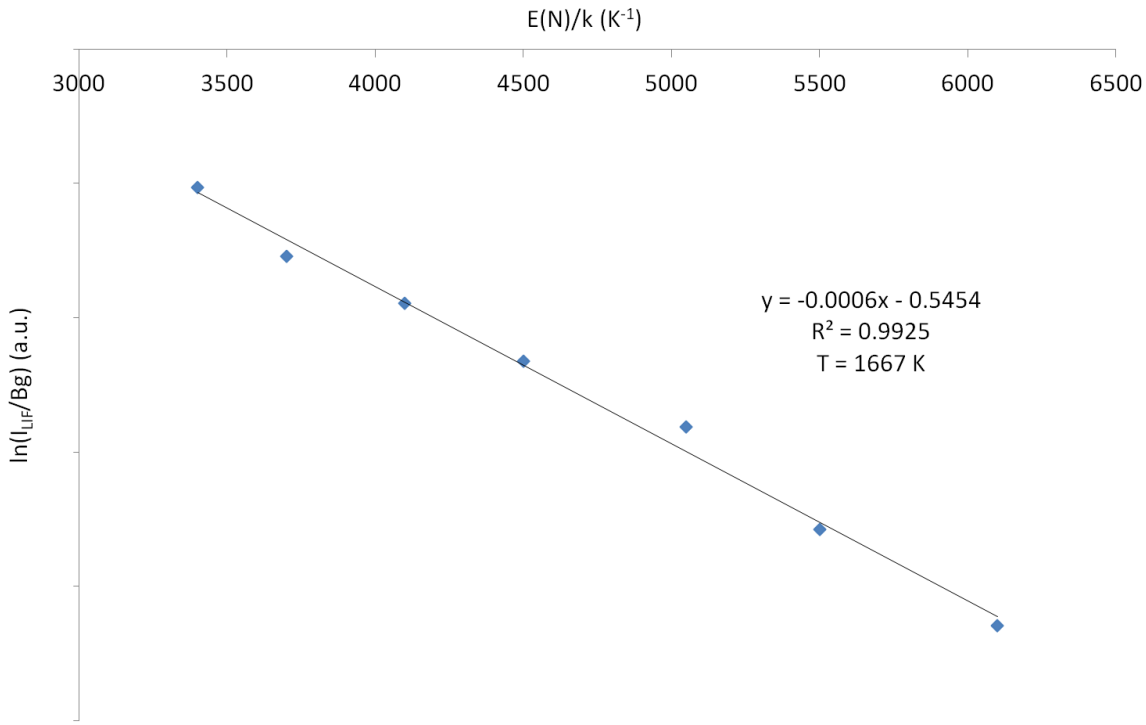

Figure 4.15: Boltzmann plotting at the fuel equivalent ratio = 2.1 and 1.8 mm height above the burner surface.

In order to obtain detailed temperature profiles in these sooting flames, OH LIF scans were performed at different flame conditions and positions. The relative fluorescence intensities and wavelengths of each peak line of S_{21} (*N = 5, 6, 7, 8, 9, 10, 11*) were recorded by the detection system described in the experimental setup chapter. As described in Section 4.2, the off-resonance measurements were performed at the wavelength of 0.08 nm away from each determined excitation lines in order to obtain all detected signals (most are PAH LIF and LII) except OH LIF. Net OH LIF profiles in sooting flames were thus obtained by subtracting reference (off-resonance) measurements from the on-resonance ones. By employing this calibration method, net signals of OH fluorescence were recorded at the peak of each S_{21} line between 302.5 nm and 304.5 nm in different flame conditions and locations. The temperature profiles from the fluorescence signals were deduced by using Boltzmann plot method discussed above shown in Fig. 4.16.

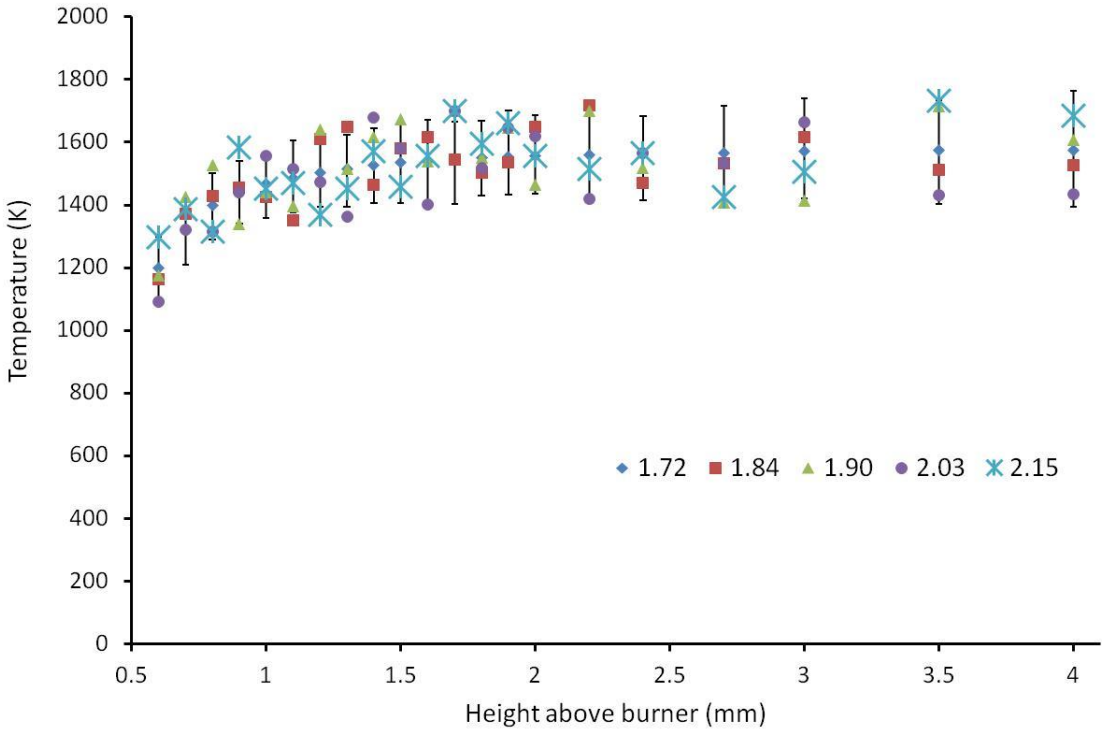

Figure 4.16: Experimental OH LIF thermometry profiles vs height above the burner surface and fuel equivalence ratios.

As shown in Figure 4.16 above, no significant difference of the temperature profiles is observed between different sooting flame conditions within the detectable range. The average temperature can be found at around 1600 K in the plateau region. The statistical error increases with increasing height above burner. This can be explained by the low OH concentration. The net OH fluorescence intensity increases to its maximum at 1.8 mm and then decreases to a stable as the height increases. However, the background signal intensity increases continually with the height above burner in

sooting flames. This representation can also explain the importance and difficulty to obtain the flame temperature profiles in these highly sooting flames. This temperature profiles were used in the following experiments and calibration of CRDS measurement.

CHAPTER 5: CRDS EXPERIMENTAL RESULTS, CALIBRATIONS, AND DISCUSSION

This chapter reports on the results obtained from CRDS experiments. First of all, CRDS calibration and quantitative calculation methods have been reviewed, and then summarised into a four-step experimental procedure and an equation to calculate the total density of a molecule. The total losses of the cavity were examined both at-resonance and off-resonance in order to obtain the absolute concentration of a radical from this chemical-complex environment which have many non-negligible interferes, such as PAH absorption and soot extinction. $^{1}CH_2$ has been spectroscopically reviewed and the spectrum was obtained by CRDS in the range between 622.1 nm and 622.8 nm. The resulting absolute concentration profiles of $^{1}CH_2$ were obtained in sooting flame. HCO was also spectroscopically reviewed and the spectrum was achieved in the range between 615.6 nm and 616.5 nm. The resulting absolute concentration profiles of HCO were obtained in sooting flame by probing the P(9) excitation line. OH qualitative concentration profiles have been obtained by LIF. The OH CRDS measurement here was used to quantify the profiles obtained from OH LIF measurements.

5.1 CRDS Calibration and Quantitative Calculation

This study is focusing on CRDS application in sooting flames which have many non-negligible interferes, such as PAH absorption and soot extinction. In order to deduce the absolute concentration of a radical from this chemical-complex environment, the total losses of the cavity should be examined both at-resonance and off-resonance. Thus, a concentration profile determination can be achieved by a four steps procedure described below.

1. The loss of the intensity in cavity caused by a specific radical is represented as a function of path length (*d*) and absorption coefficient ($\alpha_i(\lambda)$), for a single pass, can be expressed as

$$L_i(\lambda) = \alpha_i(\lambda) \times d \tag{5.1}$$

The absorption coefficient is the product of the number density in the ground state of the absorption transition and the absorption cross-section. So the total losses can be expressed as a function of laser wavelength (Mercier et al., 1999a):

$$L_T(\lambda)_{on} = L_{mirror} + L_{flame} + L_i(\lambda) + \sum_j L_j \tag{5.2}$$

In this formula, the first term of L_{mirror} due to the cavity ring-down mirrors is assumed to be a constant value *(1-R)*. The term of L_{flame} is also assumed to be constant in the same flame conditions, because L_{flame} is caused by Rayleigh scattering and beam deflections (Mercier et al., 1999b, Xie et al., 1998). The third term of $L_i(\lambda)$ is the radical of interest (OH, HCO and $^1CH_2$ in this study). The last one of $\sum_j L_j$ is caused by the broadband absorbance of species such as PAH and soot. This value was assumed to be constant within a short wavelength range (within 0.05 nm). When the laser wavelength was at resonance ($S_{21}(6)$, $^rQ_{0,7}$ and P(9) excitation line for OH, $^1CH_2$ and HCO respectively), the total losses of the cavity is $L_{mirror} + L_{flame} + L_i$ *(304.038 nm, 622.32 nm or 615.95 nm)* $+\sum_j L_j$.

2. Measurements of the profile of the total losses per pass with the laser detuned off resonance. The expression can be written as:

$$L_T(\lambda)_{off} = L_{mirror} + L_{flame} + \sum_j L_j \qquad (5.3)$$

As known above, the value of $\sum_j L_j$ was assumed to be constant within a short wavelength range (within 0.05 nm). When the reference measurements were performed off resonance of 304.038 nm, 622.35 nm or 615.9 nm, there was no absorbance of OH, $^1CH_2$ or HCO. The wavelengths for recording off-resonance measurements were selected by recording from CRDS spectra of all the probed spectrum.

3. Determination of profiles of the losses due to OH, $^1CH_2$ or HCO absorption can be obtained by subtracting off-resonance profiles from on-resonance ones:

$$L_i(\lambda) = \alpha_i(\lambda) \times d = L_T(\lambda)_{on} - L_T(\lambda)_{off} \quad (5.4)$$

4. The quantitative calculation of absolute species concentration profiles is described in detail below from the profiles of the net losses per pass.

As discussed above, the determination of species concentrations in flames using CRDS relies on the measurement of light intensity losses per pass. From these losses, the background losses have to be subtracted. Thus, the losses per pass measured by CRDS are directly proportional to the initial rotational population present in the lower state.

First of all, we need get the absorption cross-section to correct the losses per pass into absolute concentration.

The absorption cross-section of a species for a transition $i \rightarrow k$ can be calculated by using the equation (Derzy et al., 1999, Hilborn, 2002)

$$B_{ik} = \frac{1}{h\nu_0}\int_0^\infty \sigma_{ik}(\nu - \nu_0)d\nu \qquad (5.5)$$

where ν_0 is the centre of the excitation line in wavenumbers, σ_{ik} is the absorption cross-section. B_{ik} is given as 8.6×10^8 $m^2J^{-1}s^{-1}$ for the (0, 13, 0) $7_{17} \leftarrow$ (0, 0, 0) 7_{07} ro-vibrational line of $^1CH_2$ with a statistical error ≤ 20% (Derzy et al., 1999). σ_{ik} is given as 1.1×10^{-18} cm^{-2} for (0, 9^0, 0 – 0, 0^1, 0) P(9) line of HCO with an uncertainty of 60% (Lozovsky et al., 1998b).

The equation can be used to deduce the equation shown below by considering a Gaussian shape for the experimental absorption lines in this work.

$$B_{ik} = \frac{1}{h\nu_0}\frac{\sqrt{\pi}}{2\sqrt{ln\,2}}\sigma(\nu_0)\delta\nu \qquad (5.6)$$

The temperature-dependent absorption cross-section of the excited transition can be written as

$$\sigma(v_0) = \frac{B_{ik} h v_0 2\sqrt{ln\,2}}{\sqrt{\pi}\delta v} f_B \tag{5.7}$$

where δv is the linewidth (the full width at half maximum) of the laser beams, f_B is the temperature dependent Boltzmann factor. It plays a key role to link to the total population as:

$$f_B = \frac{N_i}{N_T} = \frac{g_i exp\,(\frac{-E_i}{kT})}{Q_i} \tag{5.8}$$

where N_i is the initial rotational population, N_T is the total population, Q_i is the partition function, E_i is the energy of a molecule which can be obtained by relevant literatures, g_i is the degeneracy. So the main issue for this equation is on the partition function calculation which will be discussed in detail below.

The energy of a molecule is the sum of contributions from its different modes of motion. In this work, we are considering the population distribution with a single electronic state:

$$\varepsilon_i = \varepsilon_i^R + \varepsilon_i^V \tag{5.9}$$

where *T* denotes translation, *R* rotation and V vibration.

Given that the energy is sum of independent contributions, the partition function factorizes into a product of contributions:

$$Q_i(T) = \sum_i exp\left(-\frac{\varepsilon_i}{kT}\right) = Q_R(T)Q_V(T) \quad (5.10)$$

This factorization means that we can investigate each contribution separately. $Q_R(T)$ and $Q_V(T)$ are defined as the partition functions of rotation and vibration respectively, and the function of temperature.

The rotational partition function is dependent on whether the molecule is a linear rotor or a nonlinear rotor. In this work, both $^1CH_2$ and HCO are the latter situation. The partition function of a nonlinear molecule can be defined as (Atkins and de Paula, 2010)

$$Q_R(T) = \frac{1}{\sigma}\left(\frac{kT}{hc}\right)^{\frac{3}{2}}\left(\frac{\pi}{ABC}\right)^{\frac{1}{2}} \quad (5.11)$$

where *k* is the Boltzmann constant, *A*, *B* and *C* are the rotational constants of the molecule, *c* is the speed of light, *h* is the Planck constant, *σ* is the symmetry number of

the molecule. As for $^1CH_2$, the transition is a linear-bent transition with an antisymmetric stretch vibration. The $^1CH_2$ in the ground state is slightly bent and is an asymmetric prolate rotor with asymmetry parameter κ = -0.36. However, for calculating the rotational partition function, it can be approximated using the symmetric top formula (Herzberg, 1971, Hollas, 1998). The necessarily spectroscopic data of A = 20.157 cm^{-1}, B = 11.194 cm^{-1}, C = 7.062 cm^{-1} can be found in the work of Petek et al (Petek et al., 1987b). As for HCO, although HCO is an asymmetric rotor, with an asymmetry parameter κ = -0.992, it behaves as a nearly symmetric prolate top. The necessary spectroscopic data of A = 24.294 cm^{-1}, B = 1.494 cm^{-1}, C = 1.399 cm^{-1} can be found in the literature (Serrano-Andres et al., 1998). By using these spectroscopic constants, rotational partition functions for both $^1CH_2$ and HCO can be obtained as a function of temperature. This allows the local partition function to be calculated as a function of HAB using the temperature profiles reported elsewhere in this thesis. Besides the rotational partition function, another important contribution in this work is vibrational partition function.

The vibrational partition function of a molecule can be calculated by substituting the measured vibrational energy levels into the exponentials appearing in the definition of Q_v, and summing them numerically. The overall vibrational partition function is the

product of the individual partition functions, and we can write $Q_v(T) = Q_v(1)\ Q_v(2)\ Q_v(3)\ldots$, where where $Q_v(K)$ is the partition function for the Kth normal mode and is calculated by direct summation of the observed spectroscopic levels.

If the vibrational excitation is not too great, the harmonic approximation may be made, and the vibrational energy levels written as

$$E_v = \left(v + \frac{1}{2}\right) hc\tilde{V} \quad v = 0, 1, 2, \ldots \tag{5.12}$$

where v is the vibriational quantum number and $\tilde{V}$ is the vibrational frequency.

If, as usual, we measure energies from the zero-point level, then the permitted values are $\varepsilon_v = vhc\tilde{V}$ and the partition function is

$$Q_v(T) = \sum_v \exp\left(-\frac{vhc}{kT}\tilde{V}\right) = \frac{1}{1-e^{-\frac{vhc}{kT}\tilde{V}}} \tag{5.13}$$

As for $^1CH_2$ in this work, the spectroscopic constants have been given (Comeau et al., 1989a) as v_1 = 2787 cm^{-1}, v_2 = 1351 cm^{-1}, and v_3 = 2839 cm^{-1} and a harmonic oscillator approximation while v_1 = 2488 cm^{-1}, v_2 = 1080.7 cm^{-1}, and v_3 = 1861 cm^{-1} for HCO (Serrano-Andres et al., 1998). Therefore, vibrational partition function for both $^1CH_2$

and HCO can be obtained as a function of temperature which has been measured by OH LIF. So the absorption cross-section can be finally calculated as a function of temperature and laser wavenumbers by:

$$\sigma(v_0,T)=\frac{B_{ik}hv_0 2\sqrt{ln\,2}}{\sqrt{\pi}\delta v}\frac{g_i exp\,(\frac{-E_i}{kT})}{\frac{1}{\sigma}\left(\frac{kT}{hc}\right)^{\frac{3}{2}}(\frac{\pi}{ABC})^{\frac{1}{2}}\times\sum_v exp\,(-\frac{hc}{kT}\tilde{V})} \tag{5.14}$$

Recalling the CRDS principle in Chapter 2, $\sigma(v,T)C=\alpha(v,T)$, so the total density of a molecule can be calculated from the losses per pass values by

$$N=\frac{\alpha(v,T)\sqrt{\pi}\delta v\frac{1}{\sigma}\left(\frac{kT}{hc}\right)^{\frac{3}{2}}(\frac{\pi}{ABC})^{\frac{1}{2}}\times\sum_v exp\,(-\frac{hc}{kT}\tilde{V})}{B_{ik}hv_0 2\sqrt{ln\,2}g_i exp\,(\frac{-E_i}{kT})} \tag{5.15}$$

5.2 $^1CH_2$ CRDS Measurement

Spectroscopically, $^1CH_2$ has a special character of two different low-lying electronic states (Herzberg and Johns, 1966b). It has a triplet ground state ($^3\sum_g^-$) as well as a metastable singlet state ($\tilde{a}^1A_1$). In most reaction kinetics, both of the electronic states are considered as different chemical species. The reason relies on the different reaction

speeds. Generally, reactions of the singlet radical are two orders of magnitude more than the triplet one (McIlroy, 1998, Prada and Miller, 1998). Molecular beam mass spectrometry techniques are regarded as useless for specific detection of $^1CH_2$ due to its identical mass and similar ionization potential to $^3CH_2$. Herzberg and Johns (Herzberg and Johns, 1966a) firstly reported and characterized the transitions of methylene radical. The triplet state to the excited state transitions ($^3\sum_u^- \leftarrow {}^3\sum_g^-$) can be found from the vacuum UV around 150 nm, while the singlet state to its excited transitions ($\tilde{b}^1B_1 \leftarrow \tilde{a}^1A_1$) were discovered in the red region. However, after many extensive studies about the transitions (García-Moreno and Moore, 1993), most of transitions in the red region are still unassigned due to both its complex spectroscopy and overlapping with lines from the triplet ground state. As for combustion diagnostics, Sappey et al (Sappey et al., 1990) employed LIF to detect it. However, is was found to be of extreme difficulty due to the low concentration as well as fast collisional quenching of the excited state even in low pressure flames. In contrast, intracavity laser absorption spectroscopy was successfully employed to detect qualitative $^1CH_2$ concentration profile by Cheskis et al (Cheskis et al., 1997). Several subsequent studies have focused on the $^1CH_2$ measurement by absorption techniques such as CRDS. Absolute absorption cross sections of $^1CH_2$ were recorded by Derzy et al (Derzy et al., 1999). And then, CRDS was firstly applied in McIlroy's work (McIlroy, 1999a, McIlroy, 1998) to quantitatively detect

$^1CH_2$ concentration profile in low pressure flames. Later on, Evertsen et al (Evertsen et al., 2003a) utilized the absorption cross sections from Derzy et al (Derzy et al., 1999) to obtain the quantitative concentration profiles in atmospheric flames by CRDS as well. More recently, Schocker et al (Schocker et al., 2005) made a further step to probe $^1CH_2$ successfully in rich flames. However, there appears to be no study of singlet methylene concentration profiles in sooting flame reported to date.

A $^1CH_2$ radical spectrum was obtained by CRDS in the range between 622.1 nm and 622.8 nm. Figure 5.1 is an experimental spectrum recorded at 1.3 mm above the burner in a C_2H_4-air flame with fuel equivalence ratio of 2.15. The $^rQ_{0,7}$ excitation line was selected for the experiments described below due to the isolation and known cross-section (Derzy et al., 1999).

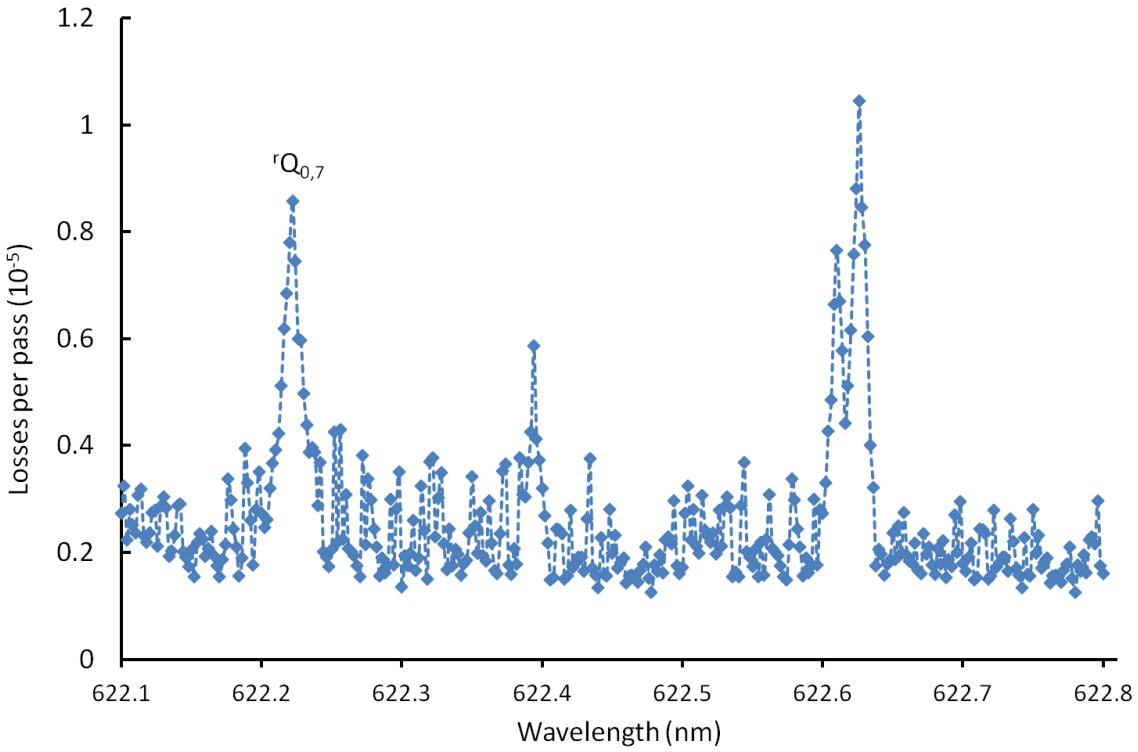

Figure 5.1: Experimental CRDS spectrum of the $\tilde{b}^1B_1(0,13,0) \leftarrow \tilde{a}^1A_1(0,0,0)$ *transition of* $^1CH_2$ *at 0.75 mm above the burner surface and fuel equivalence ratio = 2.15.*

By applying the calibration method described in the Section 5.1, Figure 5.2 represents the dependence of the losses of the cavity on the height above the burner surface with different fuel equivalence ratios. After subtraction of the off-resonance measurements, the calculation procedure for absolute concentration of $^1CH_2$ followed the method described in Section 5.1, and partition functions were calculated by using the temperature values from OH LIF thermometry, and the essential spectroscopic

parameters from Petek et al (Petek et al., 1987a, Petek et al., 1987b) , Comeau et al (Comeau et al., 1989b), Herzberg (Herzberg and Johns, 1966b) (Herzberg) and Bernath (Bernath, 2005). The resulting absolute concentration profiles of $^1CH_2$ are shown in Figure 5.3. The $^1CH_2$ is located in a thin layer close to the burner surface, which is the reaction zone of the laminar flame. The net $^1CH_2$ concentration decreases significantly with increasing stoichiometry. The error bars shown in the Figure 5.3 represent the precision (reproducibility) of the measurements. The uncertainty of the Einstein *B* coefficient used to determine the absorption cross-section of $^1CH_2$ is thought to be roughly 30% (Evertsen et al., 2003a). This is the dominant source of potential systematic error in the evaluated concentrations. The $^1CH_2$ is located in a thin layer close to the burner surface, near the reaction zone of the laminar flame. The $^1CH_2$ zone becomes narrower with increasing fuel equivalence ratio. The positions of maximum concentrations appear to stay the same positions in the flame. This is consistent with expectations since they suggest more C_3H_3 formation from $^1CH_2$ with the increasing of the fuel equivalence ratio in the sooting flames according to the studies of Wang and Frenklach (Wang and Frenklach, 1997a) and ABF (Appel et al., 2000). The recombination of two C_3H_3 is believed to be of particular importance in reactions of benzene formation which is the key step to form higher PAHs (Pope and Miller, 2000). However, the previous studies (McIlroy, 1998, McIlroy, 1999a, Evertsen et al., 2003a, Derzy et al.,

1999, Cheskis et al., 1997) of $^1CH_2$ concentration profiles in non-sooting flames indicate that the $^1CH_2$ concentration increases with increasing equivalent ratio. More recently Schocker et al (Schocker et al., 2005) reported $^1CH_2$ concentration profile in low pressure rich flames near the soot formation limit. In this study, the $^1CH_2$ concentration increases from the fuel equivalence ratio =1.5 to 2.1, however, there is a significant reduction from fuel equivalence ratio =2.1 to 2.3 where the soot formation limit is. Thus, this trend of $^1CH_2$ concentration profiles in sooting flame can be thought that more consumption than formation of $^1CH_2$ in highly rich flames especially in sooting flames. This also can indicate and highlight the importance of the pathway of $^1CH_2$ to C_3H_3 which may promote unsaturated hydrocarbons to form higher hydrocarbons in the sooting flames.

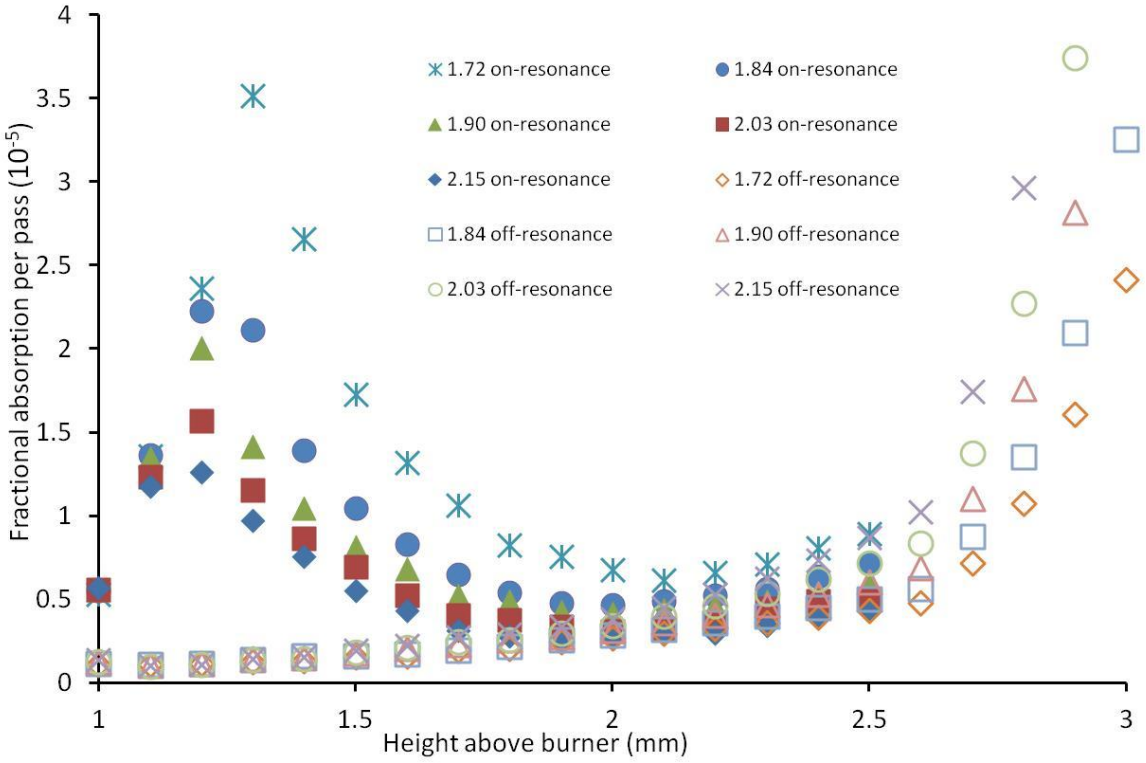

Figure 5.2: Experimental $^1CH_2$ on-resonance and off-resonance profiles of the losses per pass vs height above the burner surface and fuel equivalence ratios.

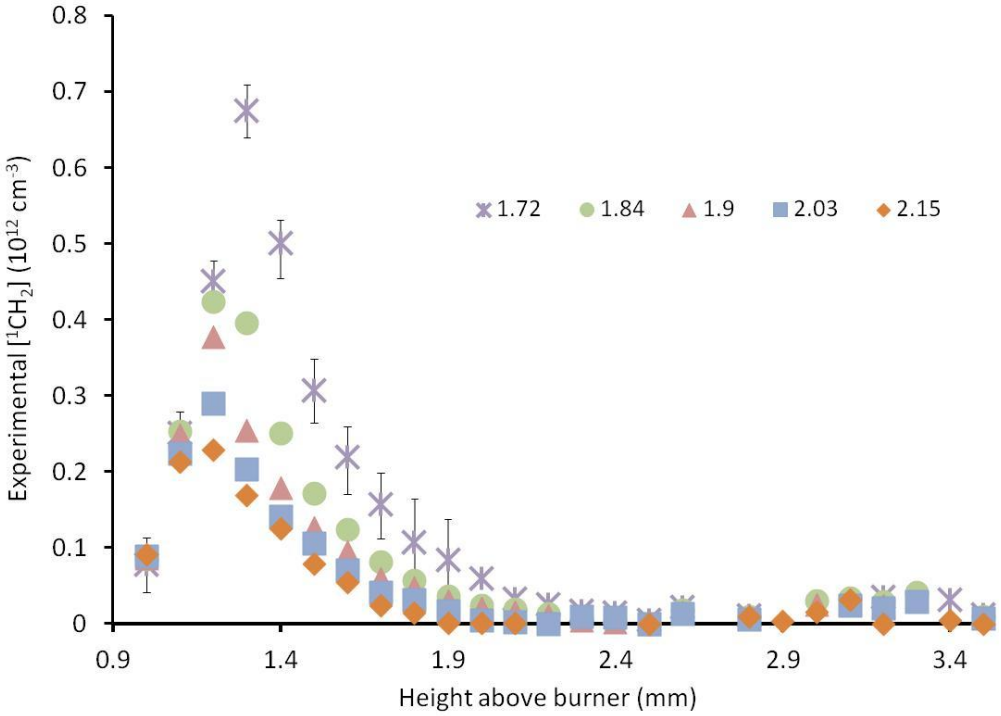

Figure 5.3: Resulting $^1CH_2$ concentration profiles vs height above the burner surface and fuel equivalence ratios.

5.3 HCO CRDS Measurement

Spectroscopically, two major electronic transitions have been discovered in ethylene flame bands in the near UV ($B^2A^{"} \leftarrow X^2A^{'}$) and the red bands ($\tilde{A}^2A^{"} \leftarrow \tilde{X}^2A^{'}$). These two ethylene bands were firstly reported by Vaidya (Vaidya, 1934). Later on, many researchers (Herzberg and Ramsay, 1955, Johns et al., 1963, Brown and Ramsay, 1975)

have continued on systematic investigations of both of transitions to provide a solid spectroscopic database. As for combustion diagnostics, on the one hand, LIF was firstly used for spatially-resolved detect ion of HCO in a low-pressure flame at the band of $\tilde{B}(0,0,2) \leftarrow \tilde{X}(0,0,0)$ around 244 nm by Jeffries et al (Jeffries et al., 1991). However, it was considered to be difficult to obtain quantitative results due to the unknown quantum yield coefficients. And then, the same research group (Diau et al., 1998) continued the study under similar conditions around 258 nm. They concluded that LIF detection of HCO is not recommended due to the strongly predissociative $\tilde{A}$ state of HCO. On the other hand, absorption techniques were successfully achieved to obtain absolute concentration of HCO in flames. Cheskis (Cheskis, 1995) firstly published the study about qualitative detection by employing intracavity laser absorption spectroscopy at the red band of $\tilde{A}^2A^{"} \leftarrow \tilde{X}^2A^{'}$. More studies (Lozovsky et al., 1997, Lozovsky et al., 1998b, Scherer and Rakestraw, 1997) were performed in low and atmospheric pressure methane/oxygen flames. More recently, Schocker et al (Schocker et al., 2005) have reported HCO detection in higher hydrocarbon fuel and rich flames under low pressure conditions. However, there is no measurement of HCO at sooting flames. Our work is focusing on HCO absolute concentration profiles at atmospheric laminar sooting flames in order to predict combustion behaviour in conjunction with simulations.

By following the same experimental procedure as $^1CH_2$ CRDS measurement, a HCO radical spectrum was also obtained by CRDS in the range between 615.6 nm and 616.5 nm. Figure 5.4 is an experimental spectrum recorded at 1.3 mm above the burner in a C_2H_4-air flame with fuel equivalence ratio of 1.72. The P(9) excitation line was selected for the experiments described below due to known absorption coefficient (Lozovsky et al., 1997).

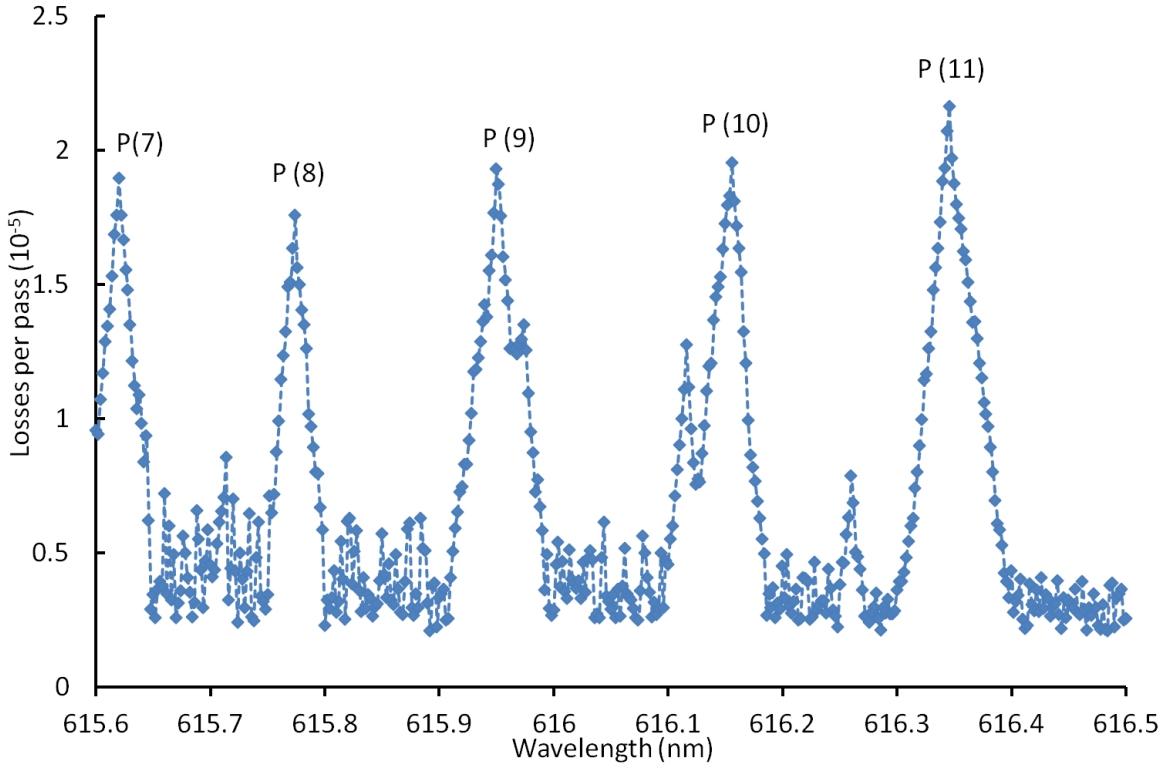

Figure 5.4: Experimental CRDS spectrum of the $\tilde{A}^2A'(0,9,0) - \tilde{X}^2A''(0,0,0)$ *transition of HCO at 1.3 mm above the burner surface and fuel equivalence ratio = 1.7.*

Figure 5.5 represents the dependence of the losses of the cavity on the height above the burner surface with different fuel equivalence ratios. The same method described above was used in the calculation of absolute concentrations of HCO from the CRDS data. Figure 5.6 shows the dependence of the resulting concentration of HCO on the height above the burner surface with different fuel equivalence ratios. The uncertainties of the absorption cross-section in the order of 60% (Lozovsky et al., 1998a)

are not included in the error bars shown in Figure 5.6 which represent the reproducibility of the measurements. The HCO is also located in a thin layer close to the burner surface, comprising the reaction zone of the laminar flame. The positions of maximum concentrations appear to be shifted slightly upwards in the flame with increasing equivalence ratio.

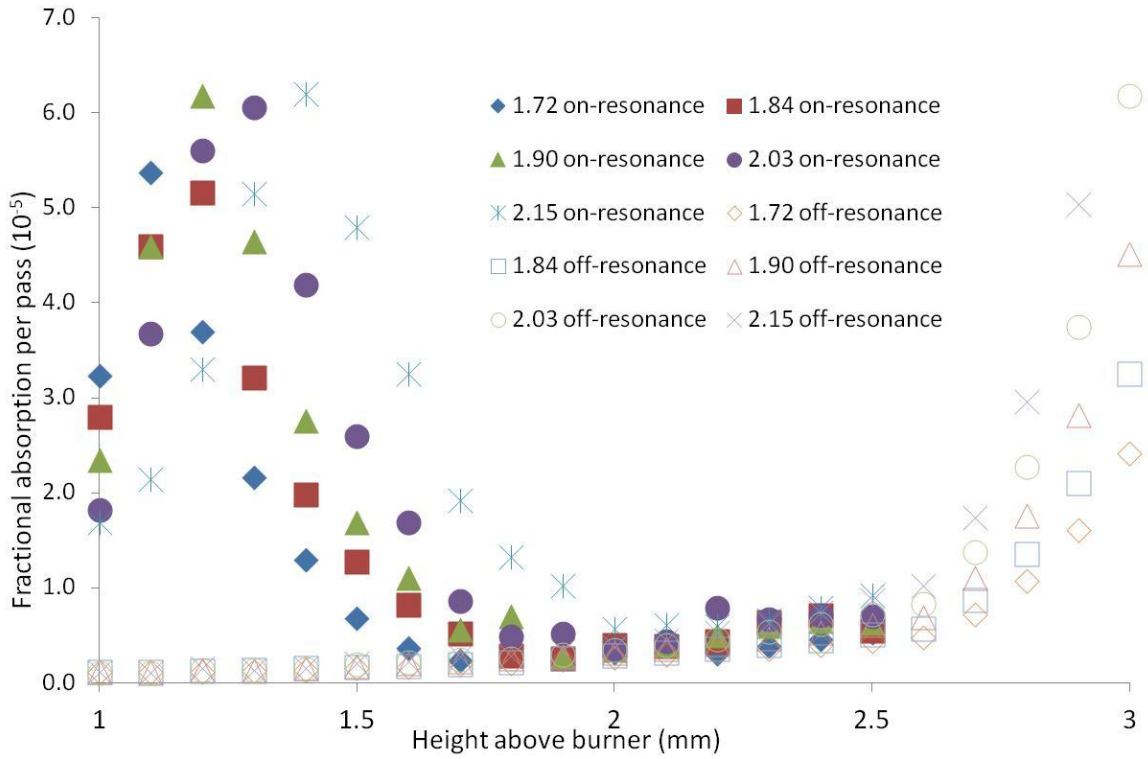

Figure 5.5: Experimental HCO at-resonance and off-resonance profiles of the losses per pass vs height above the burner surface and fuel equivalence ratios.

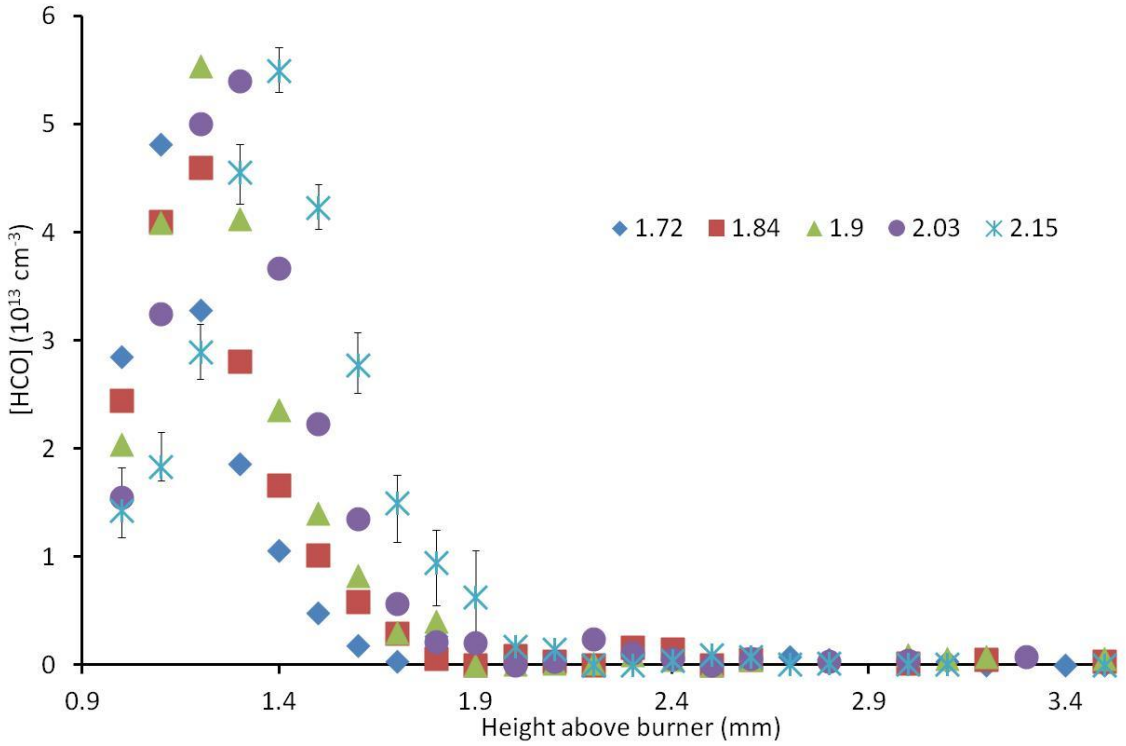

Figure 5.6: Resulting HCO concentration profiles vs height above the burner surface and fuel equivalence ratios.

In the preceding section we discussed measurements made off-resonance from the narrow absorption lines being studied. The main purpose of this was to subtract the contribution of broad-band absorption so that the concentration of the $^1CH_2$ and HCO radicals was not overestimated. Nevertheless, these off-resonance signals may also provide useful information. The fractional losses per pass measured off-resonance are plotted as a function of height above burner in Figure 5.7. The temperature downstream of the flame-front reaches a plateau so losses due to thermal effects are

not expected to change much with height above burner. It is know from other measurements not shown here that the onset of soot formation in this burner is further downstream at about 5 or 6 mm above the burner. Significant losses are observed with increasing height above burner and these are greatest for the richest flames. These results seem to be consistent with the presence of large PAH molecules relatively close to the burner surface. This highlights the potential of cavity-ring down measurements for the study of broad-band absorbers in flames as well as small radicals.

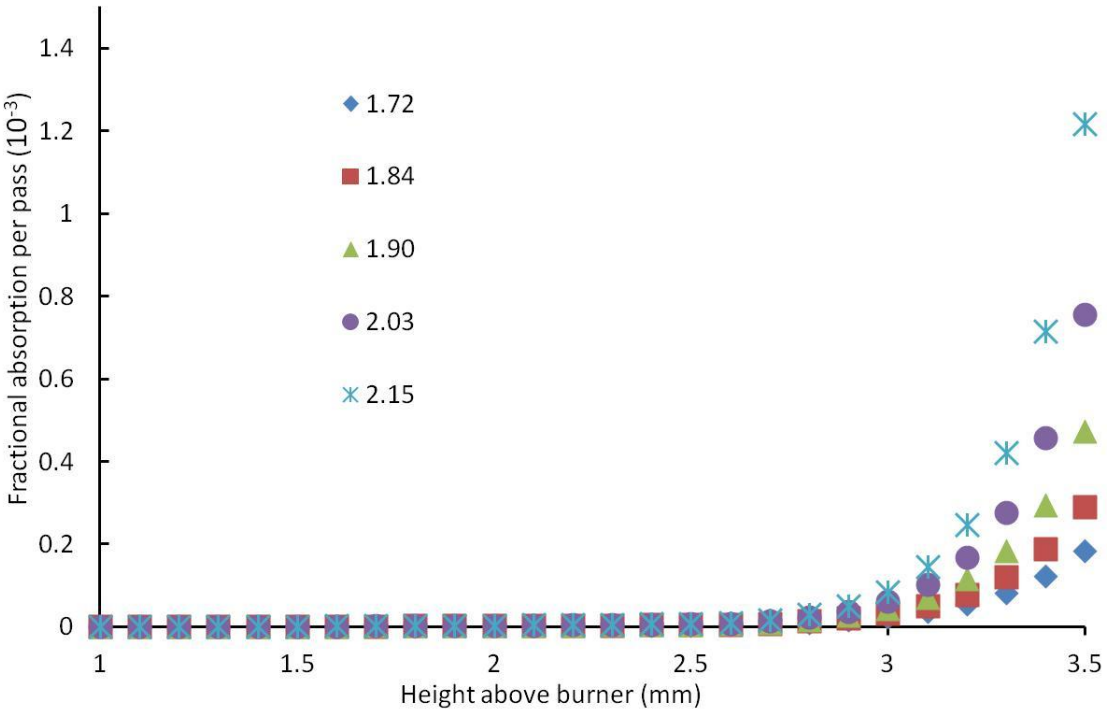

Figure 5.7: Absorbance for off-resonance excitation line VS height above the burner surface and fuel equivalence ratios.

5.4 OH CRDS Measurement

When CRDS was applied in the OH concentration measurement, many studies focused on the discussion of the multi-exponential behaviours. This phenomenon is due to the large population of OH in the flames chosen for those work. Attention then shifted to the S_{21} branch, which has a smaller absorption coefficient and has been used in the past to reduce laser trapping in atmospheric pressure flames (Barlow et al., 1989). A study (Jongma et al., 1995) indicates that multi-exponential behaviour was seen in the ringdown curves when tuned to the centre of the $S_{21}(12)$ and $S_{21}(11)$ CRDS profiles in the $A^2\sum(v^{'}=0) \leftarrow X^2\prod(v^{''}=0)$ band region. Multi-exponential ringdown curves were observed in that study when probing $A^2\sum(v^{'}=0) \leftarrow X^2\prod(v^{''}=0)$ absorption in a heated oven at atmospheric pressure and were attributed to the laser spectral width in their work being greater than the absorption line width. Hodges et al. (Hodges et al., 1996) also investigated the effects of laser bandwidth using a multi-mode dye laser with a line width broader than the absorption lines and also found multi-exponential behaviour. While Thoman and McIlroy (Thoman and McIlroy, 2000) observed multi-exponential behaviour when probing CH in a low pressure flame with a multi-mode dye laser. For quantitative measurements, Zalicki and Zare (Zalicki and Zare, 1995) have described this effect using a mathematical model and indeed predict multi-exponential

behaviour when the laser spectral width is broader than the absorption profile. This effect occurs because absorption is greater at linecentre than in the wings of the broadened absorption line, thus line centre frequencies have a smaller ringdown time than the wings. Absorption coefficient, absorption pathlength, mirror reflectivty, cavity length, and exponential fitting window play a part in the appearance of multi-exponential behaviour along with absorption line shape and laser line shape. Mercier et al. (Mercier et al., 2001) reported that even though ring-down decays may exhibit multi-exponential behaviour, a model similar to that reported by Zalicki and Zare (Zalicki and Zare, 1995) can be used to fit measured ringdown curves and extract absolute absorber concentrations. While one can formulate a model to extract absorber population from multi-exponential lines, and have some success, the added level of complexity is likely to increase experimental in the measurements. Hodges et al. (Hodges et al., 1996) make a similar argument against fitting of multi-exponential ringdown curves.

In this work, the very weakly $S_{21}(6)$ absorbing line of OH was selected in order to reduce sample absorption, thus the CRDS signals of OH did not display multi-exponential behaviour. The exponential behaviours of the OH CRDS detected signals were checked by using a least-squares fitting algorithm. Under these weak absorption conditions,

decay times were found to be identical. Therefore, as stated in Zalicki and Zare report (Zalicki and Zare, 1995), the ringdown signal $S(t+nt_r)$ recorded after n round trips of duration of t_r in the cavity can be expressed by

$$S(t + nt_r) = \sum_m S(t, \omega_m)\exp(-nL(\omega_m)) \quad (5.16)$$

where the contribution of the different cavity modes are summed. Under weak absorption conditions, they show that this expression can be approximated by

$$S(t + nt_r) = S(t)\exp(-2n((1 - R) + \propto_{eff} l_s)) \quad (5.17)$$

where $\alpha_{eff}(\omega_{lc})$ is an effective absorption coefficient measured with the laser tuned on the linecentre frequency. Thus the inverse of the ringdown time varies linearly with the absorption coefficient. Again, this OH CRDS study was performed in sooting flames which have many non-negligible interferes, such as PAH absorption and soot extinction. In order to deduce the absolute concentration of a radical from this chemical-complex environment, the total losses of the cavity should be examined both on-resonance and off-resonance as the same procedures as HCO and $^1CH_2$ CRDS measurements above.

By applying the calibration method described above, Figure 5.8 represents the dependence of the losses of the cavity on the height above the burner surface with different fuel equivalence ratios. After subtraction of the losses of cavity profiles, the calculation procedure for absolute concentration of OH followed the method described

in Section 5.1, and partition functions were calculated by using the temperature values from OH LIF thermometry, and the essential spectroscopic parameters from LIFBASE (Luque and Crosley, 1999). The main advantages of fluorescence detection are the high sensitivity and favourable spatial resolution achievable. However, the main problem is on the determination of the fluorescence quantum yield. The fluorescence intensity and spectral distribution are affected by collision processes when excited with a pulsed laser. In addition, the local collision efficiency that affects the fluorescence quantum yield is influenced by pressure, temperature and chemical composition at the observation volume. Therefore, the fluorescence quantum yield varies significantly with position, and it thus makes quantitative LIF measurements difficult in such environments. However, there are several strategies proposed to render LIF quantitative if the quantum yield is not precisely known. The most widely application is absorption calibration measurement (CRDS in this case) under the same conditions. Thus, the OH CRDS measurement is used to quantify the profiles obtained from OH LIF measurements, and all of the absolute concentration values are calibrated by the peak value at 1 mm and the fuel equivalence ratio of 1.72 from OH CRDS. The reason that two measurement points at each flame condition were recorded is that there is a large statistical scatter in the OH concentrations shown in Figure 5.9.

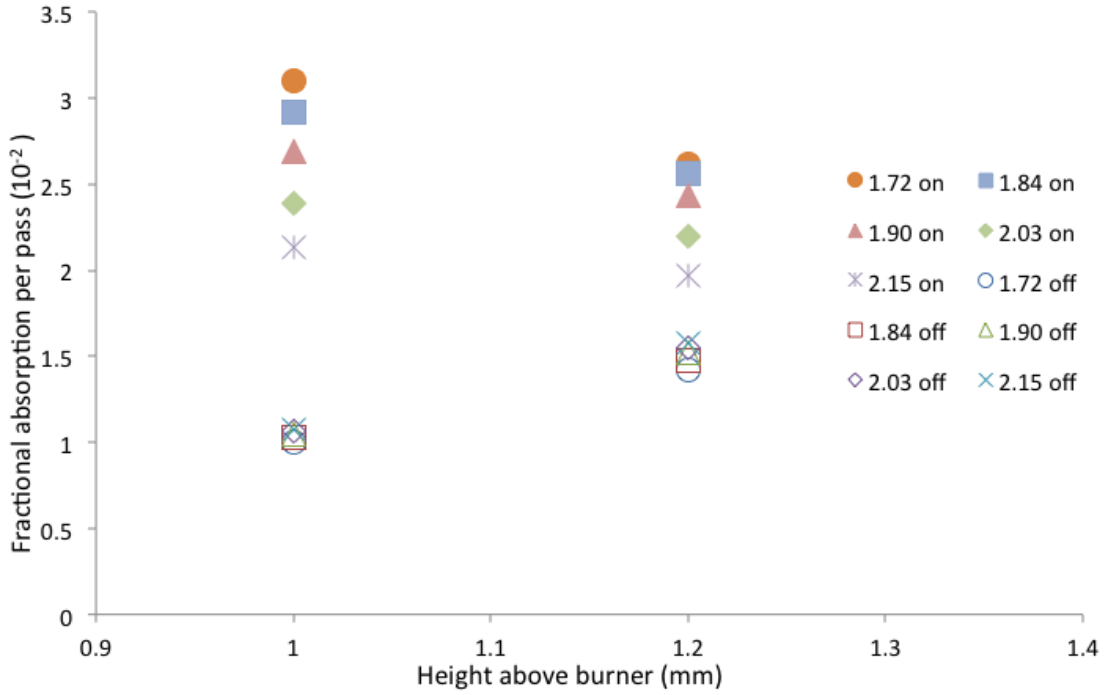

Figure 5.8: CRDS experimental OH on-resonance and off-resonance profiles of the losses per pass vs height above the burner surface and fuel equivalence ratios.

The resulting absolute concentration profiles of OH are shown in Figure 5.9. As seen in the figure, although OH LIF concentration values are calibrated at 1 mm and the fuel equivalence ratio of 1.72 from OH CRDS, the other CRDS values still reasonably match the calibrated points even in these low OH concentration and high background interferences environments.

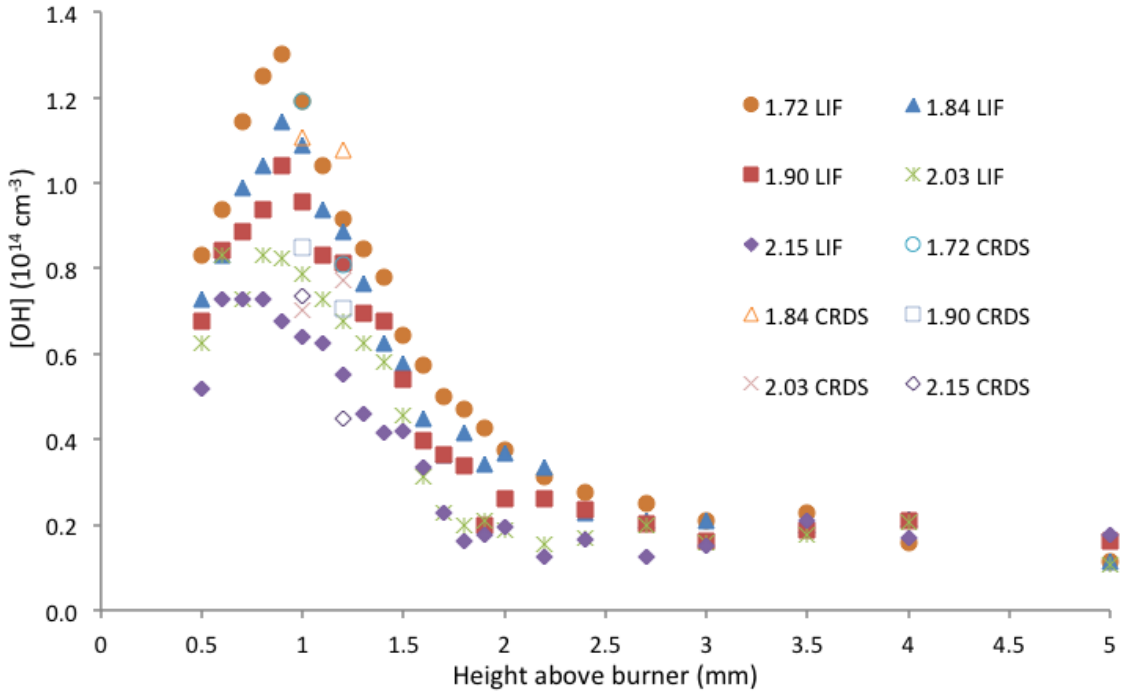

Figure 5.9: OH concentration profiles obtained by CRDS and LIF. CRDS results obtained by exciting $S_{21}(6)$ transition. The LIF profile is normalized to CRDS profile at 1 mm above the burner surface and fuel equivalence ratio of 1.72.

CHAPTER 6: MODEL VALIDATION AND DISCUSSION

6.1 Overview

Intermediate radicals are molecular fragments usually having one or more unpaired electrons. These radicals must undergo recombination reactions to convert into stable species. Importantly, the formation and interaction of these radicals are fundamental to the flame structure and have a significant influence on the global properties of the flame. As for ethylene/air combustion, the intermediates concentration profiles of OH, HCO, $^{1}CH_2$ and temperature profiles have already been measured by experiments as described in the preceding chapter. In this chapter, these experimental results are compared with simulated results in order to test the predictions of a well-known reaction mechanism from the literature. Prior to these comparisons, it is very useful to understand the relevant fundamental knowledge of how the combustion simulation works as well as the combustion chemical background of OH, HCO and $^{1}CH_2$. Also, the reasons why the Appel-Bockhorn-Frenklach chemical reaction mechanism (Appel et al., 2000) are selected for these comparisons will be discussed in detailed.

6.2 Numerical modelling of premixed laminar flames

By considering the conservation of the overall mass of the mixture, the conservation of the mass of each species, conservation of the enthalpy of the mixture and the diffusion of heat and mass, laminar flat premixed flames (Warnatz, 1978a, Warnatz, 1978b) can be described by a set of differential equations that can be solved numerically. The simulation involves solving for the mole fraction of each species, as well as temperature, as a function of height above the burner surface. The pressure is assumed to be constant and equal to the surrounding pressure. The velocity can be calculated at each point in flames by the conservation equation of the overall mass of the mixture due to the assumption of ideal gas behaviour. The temperature can be calculated from the conservation equation of energy. So the description can be written as

The continuity equation:

$$M = \rho v A \tag{6.1}$$

where *M* the mass flow rate, *v* the linear gas velocity, *ρ* the mass density, and *A* the cross-sectional area of the stream encompassing flame.

The energy conservation equation:

$$M\frac{dT}{dx}-\frac{1}{c_p}\frac{d}{dx}\left(\lambda A\frac{dT}{dx}\right)+\frac{A}{c_p}\sum_{k=1}^{k}\rho Y_k V_k c_{pk}\frac{dT}{dx}+\frac{A}{c_p}\sum_{k=1}^{k}\omega_k h_k W_k=0 \quad (6.2)$$

where x denotes the coordinate of flame, T the temperature, Y_k the mass fraction of the k'th species (a total of K species), P the pressure, W_k the molecular weight of the k'th species, W the mean molecular weight of the mixture, R the universal gas constant, λ the thermal conductivity, c_p the constant-pressure heat capacity of the mixture, c_{pk} the constant pressure heat capacity of the k'th species, ω the molar rate of production by chemical reactions of the k'th species per unit volume, h_k the specific enthalpy of formation of the k'th species, V_k the diffusion velocity of the k'th species.

The species conservation equation:

$$M\frac{dY_k}{dx}+\frac{d}{dx}(\rho A Y_k V_k)-A\omega_k W_k=0 \quad (6.3)$$

The equation of state

$$\rho=\frac{WP}{RT} \quad (6.4)$$

The types of important reactions in combustion include unimolecular decomposition reactions, bimolecular exchange and dissociation reactions, and the three-body recombination reactions. For a system containing *N* species undergoing a set of *M* elementary chemical reactions, the general *i*'th reaction can be expressed (Glassman and Yetter, 2008, Kuo, 2005)as

$$\sum_{k=1}^{N} v_{k,i}^{'} S_k = \sum_{k=1}^{N} v_{k,i}^{''} S_k \ , i = 1, \cdots, M \tag{6.5}$$

The rate of production of the *k*'th species due to the *i*'th reaction is given by

$$\omega_{i,k} = \left(v_{k,i}^{''} - v_{k,i}^{'}\right)\left(k_{f,i} \prod_{j=1}^{N} (C_j)^{v_{k,i}^{'}} - k_{b,i} \prod_{j=1}^{N} (C_j)^{v_{k,i}^{''}}\right), k = 1, \cdots, N, i = 1, \cdots, M \tag{6.6}$$

And the total rate of production of the *k*'th species is obtained by using

$$\omega_{i,k} = \sum_{i=1}^{M} \omega_{i,k} \, , k = 1, \cdots, N \tag{6.7}$$

The constant $k_{f,i}$ and $k_{b,i}$ are the forward and reverse reaction rates. Each $k_{f,i}$ is a function of temperature, usually given by the Arrhenius expression

$$k_{f,i} = A_i T^{n_i} \exp\left(\frac{E_i}{RT}\right), i = 1, \cdots, M \quad (6.8)$$

The reverse reaction rate constant $k_{b,i}$ is calculated from $k_{f,i}$, and the equilibrium constant in concentration units $K_{c,i}$, by the law of microscopic reversibility:

$$k_{b,i} = \frac{k_{f,i}}{K_{c,i}}, i = 1, \cdots, M \quad (6.9)$$

The chemical production term is determined from the law of mass action. The forward reaction rates are obtained from an Arrhenius expression, whereas the backward reaction rates are calculated from the forward rate and the appropriate equilibrium constant. The combination of the calculation model of conservation equations and the chemical reaction mechanism forms a complete mathematical description of the combustion phenomena in laminar premixed flat flames. As discussed with the aid of these equations above, the model is able to predict temperature and species profiles for two laminar premixed flame configurations by given a reaction mechanism. The first is a burner stabilized flame with fired temperature profile which requires an input of the mass flow rate; the temperature and mass flux fractions are specified at the cold boundary, and vanishing gradients are imposed at the hot boundary. With this

particular flame configuration, the burner code is capable of predicting species concentration profiles without solving the energy conservation equation. However, this requires an experimental temperature profile to be an input. In second configuration is solved from the energy conservation equation.

However, the correctness of a reaction mechanism is very challenging and needs to be validated by experimental measurements. The detailed discussion of the mechanism selection is essential for this work. In this study, the experimental results are compared to simulated concentration profiles generated using the Appel-Bockhorn-Frenklach mechanism (Appel et al., 2000). The reasons of this are provided in the following subsection. Temperature profile obtained using OH LIF thermometry is used in interpreting the CRDS data and as input for flame simulation. In this work, we used a piece of software called Cantera, which contains a model of 1D premixed flame according to the principles described above. Several key data must be supplied to Cantera including a chemical mechanism, kinetic parameters, thermochemical data, and transport properties.

6.3 Chemical reaction kinetics/mechanism of ethylene/air flame

As discussed in Section 6.2, a complete combustion simulation consists of transport and thermo-chemical property data and a chemical reaction mechanism with kinetic parameters. Generally, there are two types of reactions (global and elementary) involved in combustion processes. The global reaction represents an overall reaction of the fuel and oxidiser to form burnt products, while the elementary reaction consists of breaking or formation of possible intermediate species during the combustion process. The accumulation of these elementary reactions finally forms the global reaction expression. The combustion of hydrocarbon fuels consists primarily of sequential fragmentation of the initial fuel molecule into smaller intermediate species which are then converted into final products, predominantly H_2O and CO_2 (Westbrook and Dryer, 1984). In many cases, these intermediate species can be fuel themselves. For example, ethylene is an intermediate in the combustion of propane and higher hydrocarbons.

In this work, premixed ethylene and air are supplied to a flat flame burner at atmospheric pressure; the global reaction can be expressed as

$$C_2H_4 + 3(O_2 + 3.76N_2) \rightarrow 2CO_2 + 2H_2O + 11.28N_2 \quad (6.10)$$

Although the global reaction expression looks very straightforward, even early studies (Westbrook et al., 1983) estimated that there are at least 93 elementary reactions as well as 26 chemical species within laminar ethylene and air flames. After that, a number of studies contributed proposed mechanisms for ethylene-air listed in the Table 6.1. These involve up to 100 chemical species and 542 elementary reactions (Wang and Frenklach, 1997b), (Appel et al., 2000) and (Mehta et al., 2009). These modifications were estimated to provide a better description of atmospheric ethylene-air flames in both lean and rich conditions. In addition, the A-B-F mechanism (Appel et al., 2000) also includes a description of soot formation in rich flames.

Mechanism name	Number of species	Number of elementary reactions	Reference and notes
W-F 99	99	533	(Wang, 2011, Wang and Frenklach, 1997a)
A-B-F 100	100	542	(Appel et al., 2000)
Q-L-Y 70	70	463	(Qin et al., 2000)
Q-L-Y 33	33	205	(Qin et al., 2000) reduced by Law (LAW, 2005)
W-I 46	46	235	The San Diego Mechanism (UCSD)
A-B-F 31	31	179	Retain species common to A-B-F 100 and Q-L-Y 33
L-V-W 19	19	36	(Li et al., 2001)

Table 6.1: Gas phase reaction mechanisms for ethylene-air flames.

A comprehensive flame mechanism in sooting flame consists of two principal sub-models. The first one is gas phase chemistry which mainly describes the preheating and reaction zones, and determines the flame structure. The other one is soot particle dynamics which describes the evolution of the soot particle ensemble. The A-B-F mechanism has been widely applied in many systems to predict both gas phase profiles and the soot volume fraction and number density. The prediction of gas phase profiles extends to PAHs formation while the particle dynamics is based on the average properties of a soot ensemble, aggregate structure of a soot particle, and fully resolved

soot particle size distribution. Applications of the ABF mechanism are summarised in Table 6.2.

Gas phase		Particle dynamics	
Combustion type	Reference	Research focus	Reference
Heptane combustion in engine	(Babushok and Tsang, 2004)	Average properties of a soot ensemble	(Kazakov et al., 1995), (Appel et al., 2000, Appel et al., 2001)
Nonpremixed methane flames	(D'Anna and Kent, 2003)	Aggregate structure of a soot particle	(Balthasar and Frenklach, 2005a, Balthasar and Frenklach, 2005b)
Diffusion flames	(Violi et al., 2003)	Fully resolved soot particle size distribution	(Balthasar and Kraft, 2003, Singh et al., 2006)
Laminar premixed flames	(Appel et al., 2001)		

Table 6.2: Summary of ABF mechanism validation in experiments.

The gas phase chemistry component of the ABF mechanism is based on an extension of the GRI-Mech 1.2 mechanism (Smith et al., 1999), which is regarded as one of the most

reliable chemical mechanisms of C_1 chemistry in combustion processes, to describe the smaller hydrocarbon reactions in the mechanism. In addition, the gas phase chemical mechanism of the W-F mechanism (Wang and Frenklach, 1997b) for PAHs formation in C_2 hydrocarbon flames is the basis of ABF mechanism. First of all, the pyrolysis and oxidation of C_1 and C_2 species and the formation of higher species are in present in this mechanism. Moreover, it also consists of the formation and oxidation of larger molecules such as linear hydrocarbons up to C_6 species, the formation of benzene and further reactions leading to pyrene, and the oxidation pathways of the aromatic species. More specifically, the reactions of C_4H_x species and acetylene, C_6H_x species cyclization, and propargyl radicals combination are integrated together to describe the formation of benzene and phenyl (Adkins et al., 2013, Apicella et al., 2007). Propargyl is also important involving in the $^1CH_2$ reaction pathways. This formation is believed as the first step of the PAHs formation, while PAHs are regards as the first step of a particle inception (Wang et al., 2013). In order to better illustrate the combustion processes, Figure 6.1 (Glassman and Yetter, 2008) provides a schematic description of a laminar premixed flames including the gas phase and soot dynamics mechanisms. This description starts from the burner surface. Firstly, the preheat and reaction zones consist of oxidation reaction as well as the formation of smaller PAHs. This is followed by the inception of soot particles and soot aggregation. Please note that the size of

larger PAHs and soot particles represented by black dots are not to scale and are for schematic purpose only.

The ABF mechanism is the most comprehensive of the scheme listed in Table 6.1 and has therefore been chosen for comparison with the experimental results presented in this thesis. Although the measurements performed some radical intermediates and not large PAH molecules or soot particles, the model prediction will also be available for comparison with experimental measurements performed in the same flame by other group members.

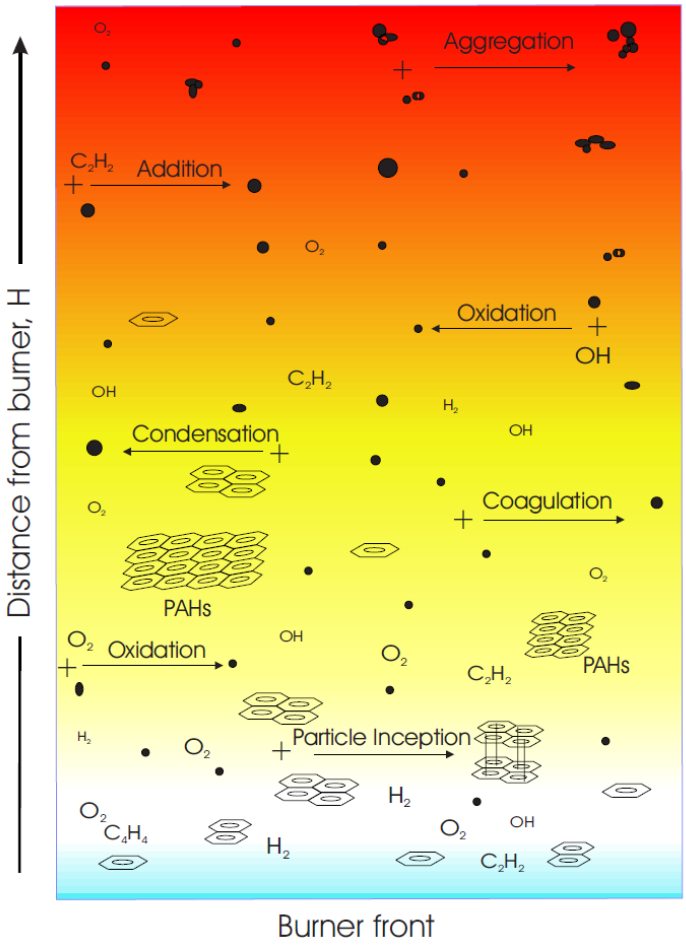

Figure 6.1: Schematic description of a laminar premixed flat flame with the processes in the ABF soot model highlighted.

It is stated by both Wang and Frenklach (Wang and Frenklach, 1997a) and Appel et al (Appel et al., 2000) that the accuracy of the species profiles provided by gas phase chemical mechanism plays a key role to obtain correct outputs from the particle dynamics mechanism. For instance, some factors involving the gas phase mechanism

can affect the soot particle nucleation and surface growth rates. Intermediate species are of importance to the correctness and reliability of the mechanisms and models. Highly resolved experimental data are required to test reaction mechanisms/models and the effects of their assumptions on the authenticity of the computations. These properties of the flame include temperature and intermediate species concentration profiles.

6.4 Temperature profiles comparison

In this work, the flame simulations were performed with the Cantera flame code (Goodwin). The Cantera program provides many different one-dimensional calculations of systems including one of a laminar, premixed flat-flame stabilized at a stagnation point (for simulating the stabilization plate in this experimental setup). The burner surface temperature and molar species flow rates are specified at the burner boundary, and a finite difference procedure is used to solve the species continuity equations. The stagnation point was set to 800 K. The burner surface temperature was at 350 K. The fuel-air mixture conditions were inputted from Table 3.1. The function “prune grid refinement” in the Cantera program was selected, which allows grid points to be

removed if they are no longer required to resolve the solution. This is important here, since the flamefront moves as the mass flowrate is increased. Without using 'prune', a large number of grid points would be concentrated upsteam of the flame, where the flamefront had been previously. Therefore, it also helps to generate adequate grid size according to the local gradient and curvature of the temperature and species concentration, making the simulation more accurate in the reaction zone. Comparison of a published reaction mechanism (ABF) with our experimental results will be presented here. The modelling involved two different phases:

1: For each of the flame conditions studied, the model was run with the solution of the energy equations included.

2: For each of the flame conditions, the model was run with temperature fixed condition. This temperature profile was obtained from the OH LIF thermometry in Section 4.3 for the input. The OH LIF measured temperature profiles at different flame conditions was close less than ± 150 K shown in Figure 4.16, so an average temperature profile was used for all 5 flame conditions in the modelling.

Since our work is focused on sooting flames of C_2H_4 and air, many mechanisms including GRI 3.0 are not suitable in that environment. However, the ABF mechanism (Appel et al., 2000) concentrates on laminar premixed flames of C_2 hydrocarbons, and includes the detailed developments in gas-phase reactions, aromatic chemistry and soot formation. It has been optimized for C_2H_4 as fuel over a broad range of temperatures, pressures, and equivalence ratios for premixed oxidation reaction systems. In this research, the ABF mechanism was used as the basis of the chemical kinetic input in the flame simulations. The ABF mechanism is at present the mechanism best suited to describe the flames in this work.

The first important comparison with the ABF simulated results in these flames is temperature profiles in the flames shown in Figure 6.2. Generally, a good agreement of temperature profiles behaviour can be observed between experiments and ABF simulation. The simulated temperature is slightly higher than experimental one. However, the full temperature profile cannot be obtained due to low OH concentration at lower and higher positions of the reaction zone. The lacking part of experimental temperature profile can be predicted by this comparison. The average temperature can be found at 1550 K in the plateau region in experimental results, while the average simulated temperature is 1680 K in that region. In order to predicate the lacking part of

experimental temperature profile, we assumed the ratio of the average temperature difference over the average simulated temperature in the plateau region is the same at the lacking positions. In the mathematical expression, (1680 K – 1550 K) / 1680 K = (T_{sim} - T_{pre}) / T_{sim}. The resulting full profile shown in Figure 6.3 was used as an input to Cantera software to generate the modified ABF simulation results.

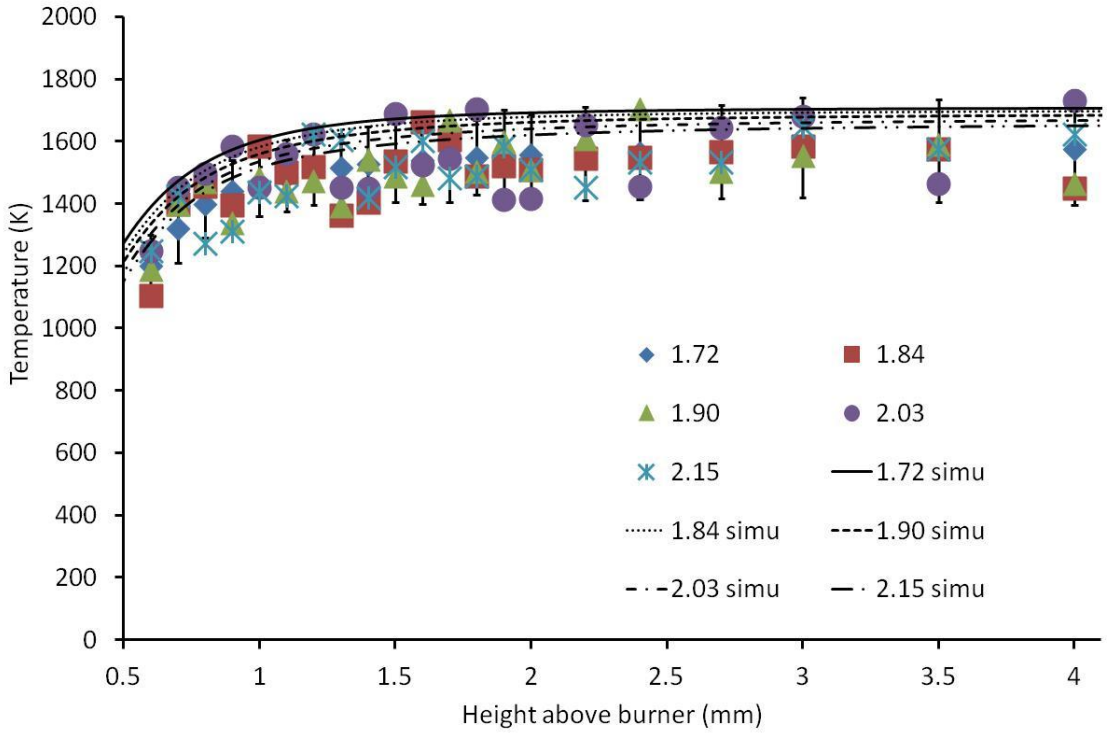

Figure 6.2: Comparison of experimental OH LIF thermometry profiles and ABF-simulations vs height above the burner surface and fuel equivalence ratios.

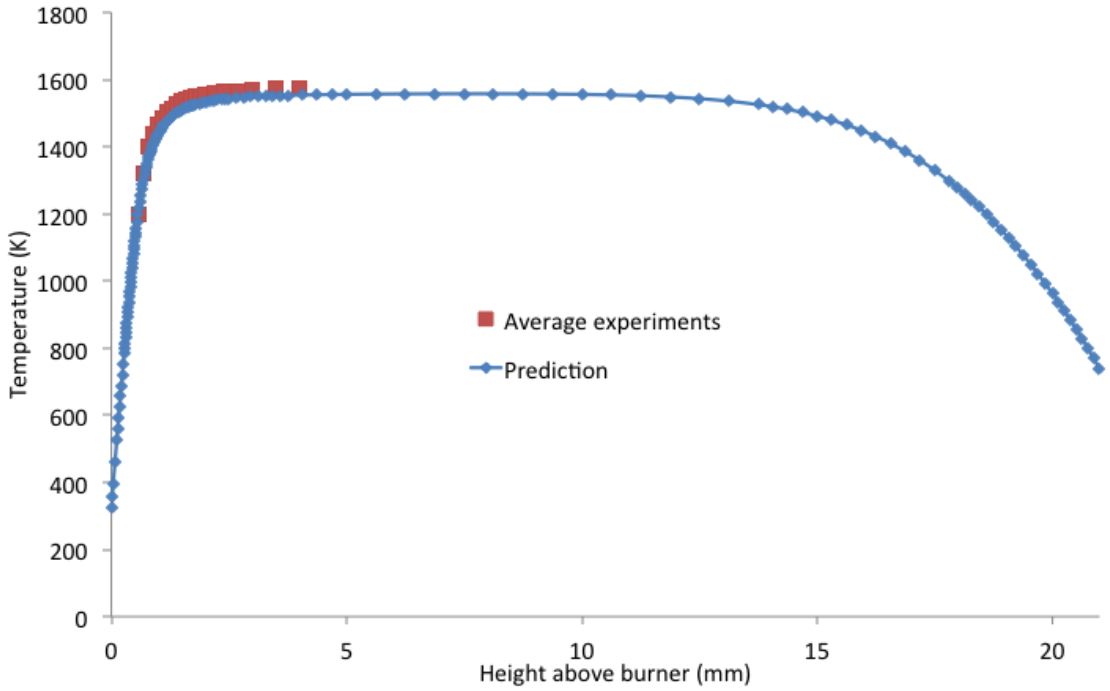

Figure 6.3: Predicted temperature and average experimental profiles vs height above the burner surface.

6.5 Sensitivity analysis

As shown in thermometry part above, net OH LIF results have relatively high errors due to the intense luminosity, soot incandescence and PAH fluorescence, low OH concentration, attenuation of the incident beam and signal trapping. In addition, the

temperature profiles were deduced from these results, and also have high errors (+/-150K). Therefore, the next stage focuses on the sensitivity analysis of the mechanism by varying temperature profiles in order to check how significant the temperature influents the resulting species concentration profiles. Keeping all input parameters in the simulation, and just adding/reducing artificial 100K to the originally program-calculated temperature profiles in the plateau region. And then by using the artificial temperature profiles as input to the program, the concentration profiles of $^1CH_2$ and HCO can be obtained and compared in Figure 6.4 and Figure 6.5. There is no significant difference observed in these Figures. Both absolute values are less than 10% different as the original results while both positions have the difference of less than 0.04 mm. These analyses can show that the experimental temperature errors in the simulation settings lead to small deviations for $^1CH_2$ and HCO concentration profiles. Although small difference shown in these Figures, they also represent that the maximum concentration values of both $^1CH_2$ and HCO decrease slightly with the increasing of temperature while the profiles shift towards to the burner surface slightly with the increasing of temperature.

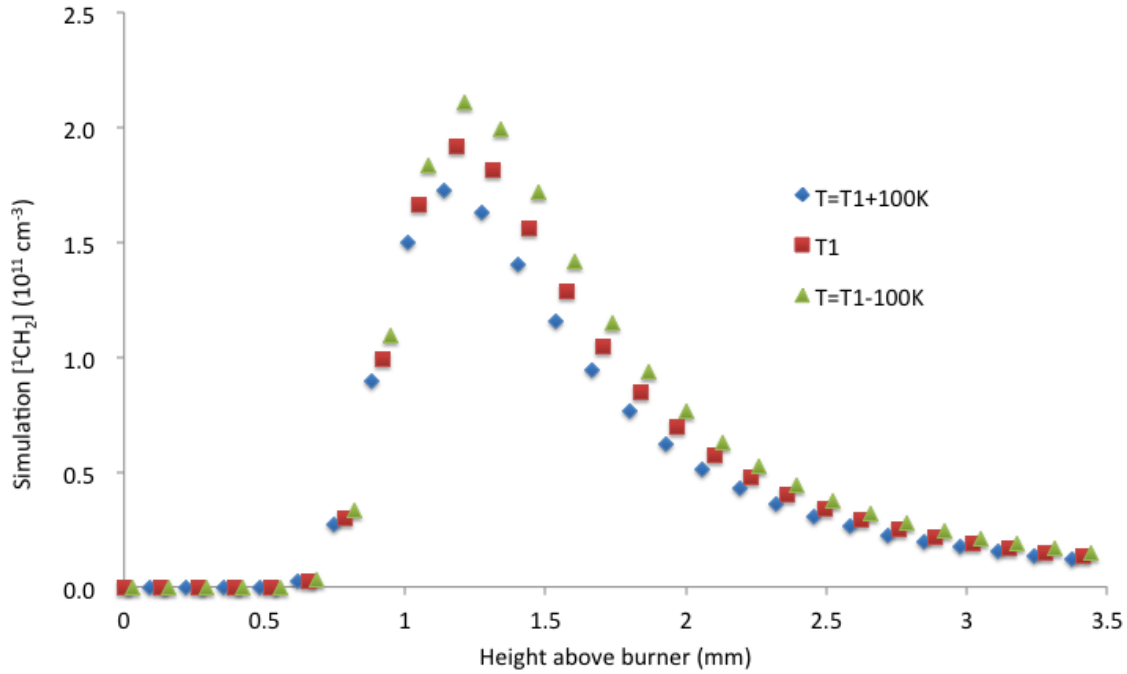

Figure 6.4: Sensitivity analysis of simulated $^1CH_2$ concentration profiles at fuel equivalent ratio = 2.1 vs height above the burner surface.

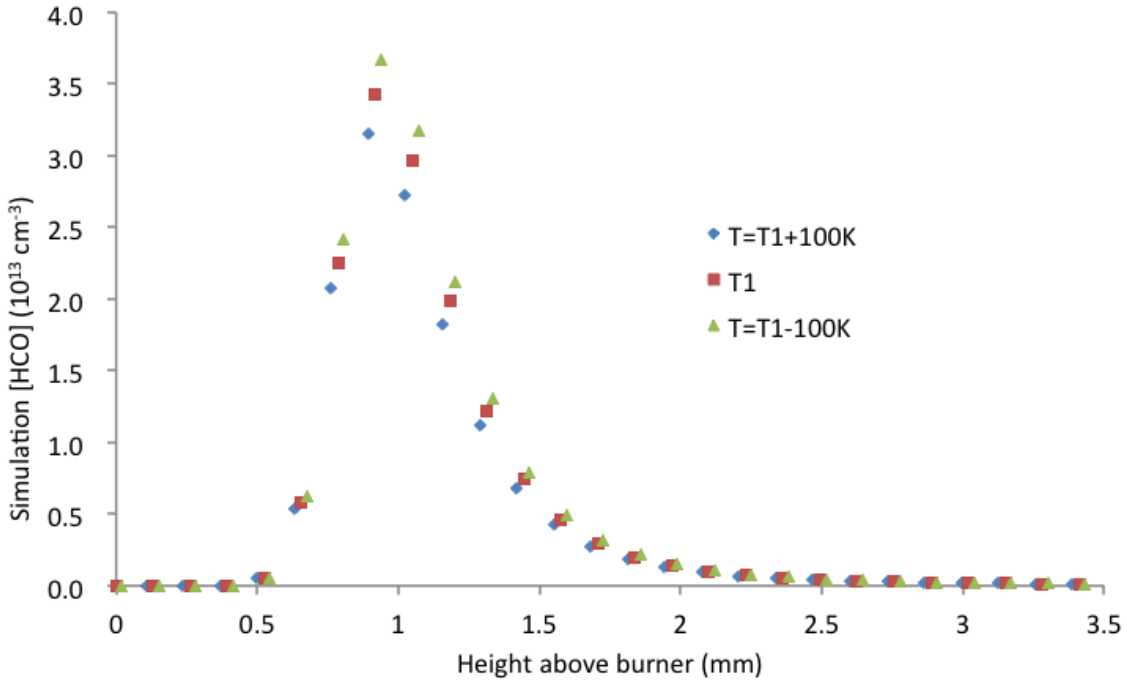

Figure 6.5: Sensitivity analysis of simulated HCO concentration profiles at fuel equivalent ratio = 2.1 vs height above the burner surface.

6.6 OH profiles comparison

Hydroxyl (OH) radical is regarded as an important precursor towards combustion chain chemistry. Due to its importance to both physical and chemical combustion, therefore numerous studies (Cattolica and Schefer, 1983, Chan and Daily, 1980, Schocker et al., 2005, Kohse-Höinghaus, 1990, Kohse-Höinghaus, 1994, Kohse-Höinghaus et al., 1989) into OH radicals have been carried out. As known from the chemical reaction research

in combustion, it is apparent that H_2-O_2 sub-mechanism, among which OH radicals are mainly evolved, is the essential route for any hydrocarbon fuel oxidation. OH radicals are also believed as one of the main contributors towards the chemiluminescence effect observed in hydrocarbon flames (Fristrom and Westenberg, 1965). In addition, although OH radicals are usually observed near burner surface within reaction zone, their reactive nature has been discovered to oxidize soot in excess (Millikan, 1962). The elementary reactions for hydrogen oxidation as well as their rates have been extensively studied and documented (Wang and Frenklach, 1997a, Smith et al., 1999). These reactions follow the chain-branching and terminating steps listed below (Appel et al., 2000) which results in the evolution of OH radicals.

Chain-branching reactions:

$$H + O_2 \rightleftharpoons O + OH \tag{6.11}$$

$$O + H_2 \rightleftharpoons H + OH \tag{6.12}$$

$$OH + H_2 \rightleftharpoons H + H_2O \tag{6.13}$$

$$OH + OH \rightleftharpoons O + H_2O \tag{6.14}$$

$$CO + OH \rightleftharpoons CO_2 + H \tag{6.15}$$

Chain-terminating reactions:

$$H + H + M \rightleftarrows H_2 + M \quad (6.16)$$

$$H + OH + M \rightleftarrows H_2O + M \quad (6.17)$$

$$O + H + M \rightleftarrows OH + M \quad (6.18)$$

$$O + O + M \rightleftarrows O_2 + M \quad (6.19)$$

where *M* refers to any available third body species. The hydroxyl radical participates in many abstraction reactions so that it is frequently used as marker for hot zones in combustion processes, especially as a powerful temperature measurement tool as described in the previous chapter.

By running the Cantera with the flame temperature profile fixed to the one obtained by extrapolation from experimental results, the absolute concentration profiles of OH shown in Figure 6.6 were obtained. Overall, these OH profiles show good agreement between experiment and simulation. The position of maximum concentrations match well. The positions of maximum concentrations observed experimentally appear to be slightly closer to the burner surface than the model predictions. Likewise, the experimental maximum concentrations are slightly higher than the simulated ones. This discrepancy is considerably greater that could be explained by the high OH LIF/CRDS

signal to background ratios. The positions of maximum concentrations observed experimentally appear to be shifted very slightly towards the burner surface with increasing equivalence ratio. This is consistent with expectations since the cold gas velocity has been held constant. However, it does not appear in the simulated profiles. Moreover, the simulated profiles are considerably boarder than the experimental ones, indicating that the rates of some reactions consuming OH may be underestimated. What's more, the OH concentration profiles increases to its maximum at around 1.1 mm and then decreases to a stable value with the height increases in both experimental and simulated graphs. Such behaviour would be expected, as there are thousands of reactions in a flame while these reactions take place in different zones in a flame front. From this experiment, we can explain that the more OH radical is formed than decomposed in the zone between 0 mm and 1.1 mm while less OH radical is formed than decomposed in the zone after 1.1 mm, and the highest OH concentration in sooting flames is at about 1.1 mm above the burner surface. Moreover, more explanations can be contributed to OH radical more likely formed in lean flames or non-sooting regions.

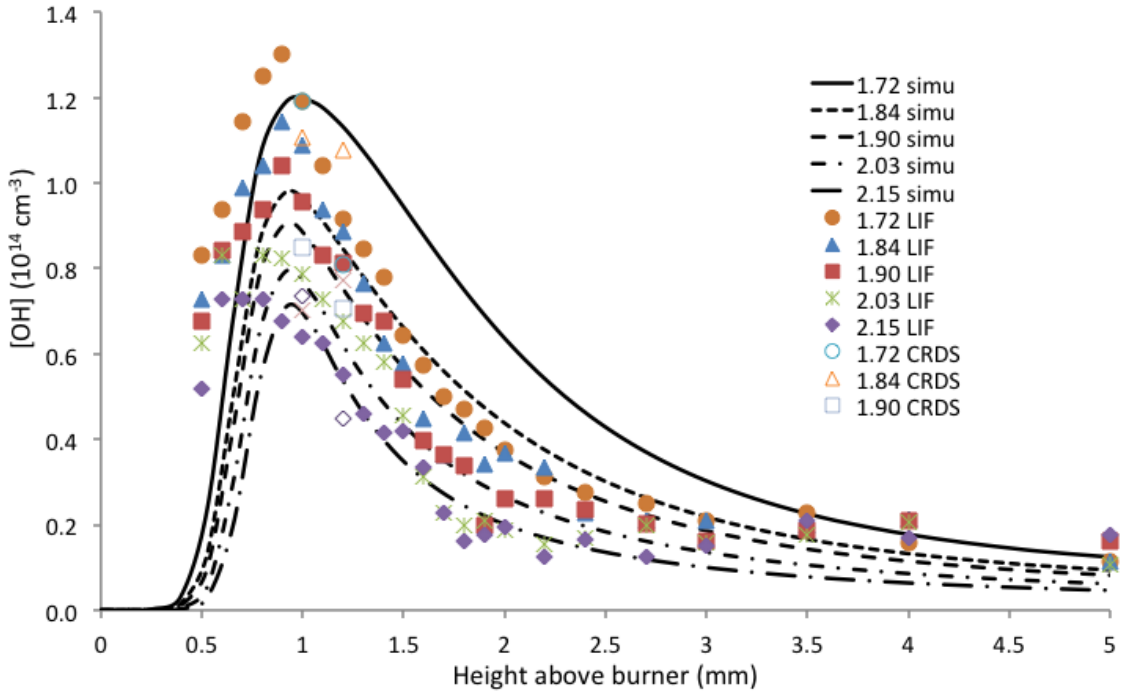

Figure 6.6: Comparison of experimental OH concentration profiles and ABF-simulations vs height above the burner surface and fuel equivalence ratios.

6.7 $^1CH_2$ profiles comparison

The singlet methylene radical ($^1CH_2$) is known as a key radical in the formation and reduction of nitrogen oxides. Research (Schocker et al., 2005) reveal its ability of insertion reactions with C-H bonds or addition reactions with alkenes in hydrocarbon combustion processes, especially in fuel rich flames. This ability may promote unsaturated hydrocarbons to form higher hydrocarbons, such as PAHs, and ultimately

to form soot. The reaction was considered to be important for the formation of propargyl radicals (C_3H_3) in flames (Pope and Miller, 2000). The recombination of two C_3H_3 is believed to be of particular importance in reactions of benzene formation which is the key step to form higher PAHs. The key reactions related to $^1CH_2$ are listed for better understanding the pathway.

$$^1CH_2 + NO \rightleftarrows HCN + OH \quad (6.20)$$

$$CH_3 + OH \rightleftarrows {}^1CH_2 + H_2O \quad (6.21)$$

$$^1CH_2 + H_2 \rightleftarrows CH_3 + H \quad (6.22)$$

$$^1CH_2 + O_2 \rightleftarrows CO + OH + H \quad (6.23)$$

$$^1CH_2 + C_2H_4 \rightleftarrows C_3H_6 \quad (6.24)$$

$$^1CH_2 + CH_3 \rightleftarrows C_2H_4 + H \quad (6.25)$$

$$^1CH_2 + C_2H_2 \rightleftarrows C_3H_3 + H \quad (6.26)$$

$$C_3H_3 + C_3H_3 \rightleftarrows C_6H_5 + H \quad (6.27)$$

$$C_3H_3 + C_3H_3 \rightleftarrows fulvene \quad (6.28)$$

Pope and Miller (Pope and Miller, 2000) reported a new mechanism of benzene and phenyl radical formation in three different flames and highlighted the importance of the pathway of $^1CH_2$ to C_3H_3 in all flames. Figure 6.7 represents the major predicted pathways for C_3 radical formation from the fuel for the three flames reported in Pope and Millers study. As known from the figure, the pathway of the formation C_3H_3 and benzene for sooting premixed laminar flat ethylene/air must undergo $^1CH_2$ radicals. Therefore, $^1CH_2$ radicals as the important intermediate species for PAHs formation need to be measured and tested in sooting flames in order to validate the mechanism.

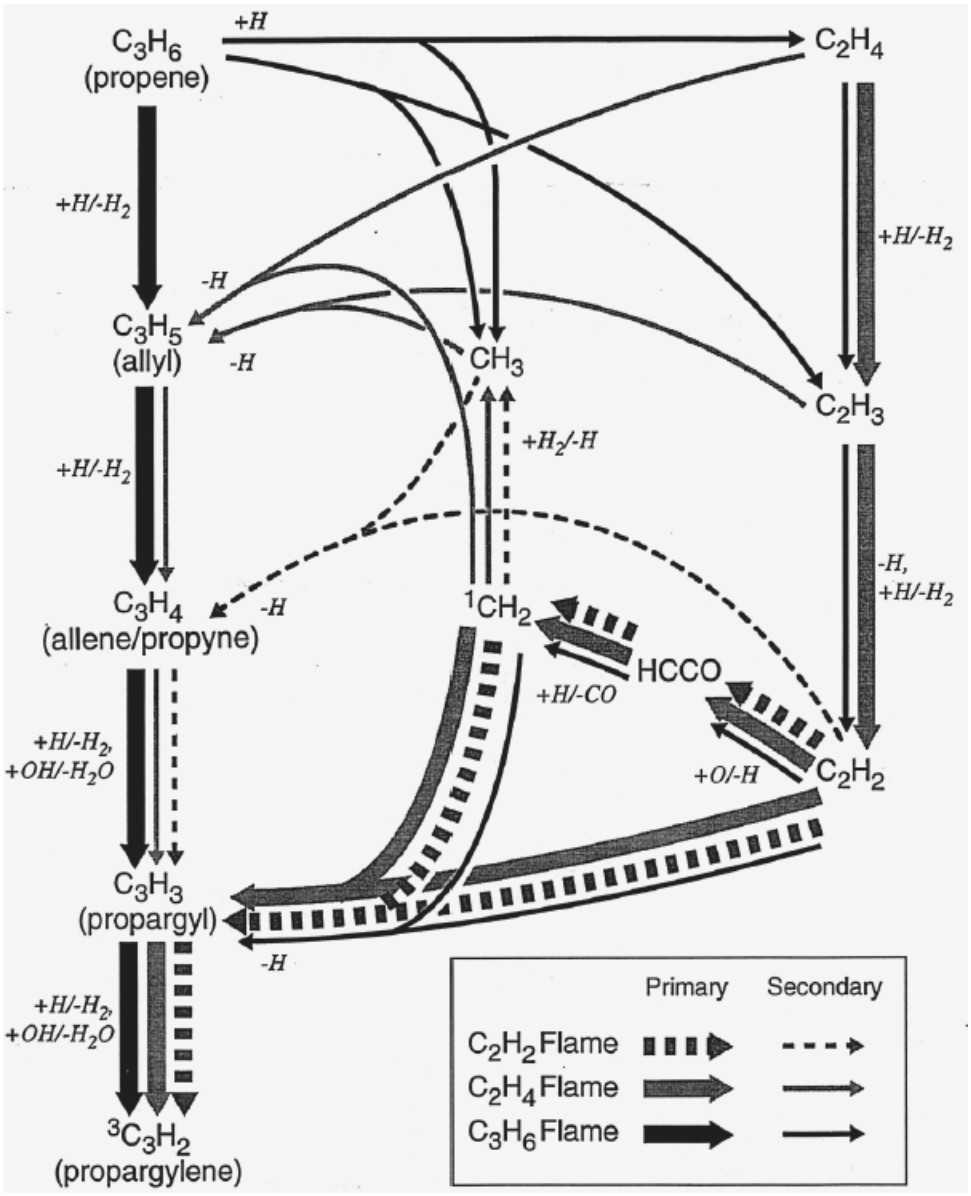

Figure 6.7: Predicted primary and secondary formation pathways of C3 radicals from the mechanism described by Pope and Miller *(This figure has been copied from (Pope and Miller, 2000)).*

Results of simulations for $^1CH_2$ radical are shown together with experimental data in Figure 6.8. Generally, there is good agreement between experiment and simulation. The positions of maximum concentrations from CRDS experiments appear to stay the same positions in the flame as well as the simulated values. Moreover, the simulated profiles are considerably boarder than the experimental ones, indicating that the rates of some reactions consuming $^1CH_2$ may be underestimated. With the increasing of the fuel equivalence ratio, the concentration of $^1CH_2$ decreases. What's more, the $^1CH_2$ concentration profiles increases to its maximum at around 1.2 mm and then decreases to a stable value with the height increases in both experimental and simulated graphs. These are consistent with expectations and the simulation results, since the mechanism (Wang and Frenklach, 1997a, Appel et al., 2000) suggests more C_3H_3 formation from $^1CH_2$ with the increasing of the fuel equivalence ratio in the sooting flames. And then, the recombination of two C_3H_3 is believed to be of particular importance in reactions of benzene formation which is the key step to form higher PAHs (Pope and Miller, 2000). However, the previous studies (McIlroy, 1998, McIlroy, 1999a, Evertsen et al., 2003a, Derzy et al., 1999, Cheskis et al., 1997) of $^1CH_2$ concentration profiles in non-sooting flames indicate that the $^1CH_2$ concentration increases with increasing stoichiometry. More recently Schocker et al (Schocker et al., 2005) reported $^1CH_2$ concentration profile in low pressure rich flames near the soot formation limit. In this study, the $^1CH_2$

concentration increases with increasing stoichiometry from the fuel equivalence ratio =1.5 to 2.1, however, there is a significant reduction from fuel equivalence ratio =2.1 to 2.3 where the soot formation limit is. Thus, this trend of $^1CH_2$ concentration profiles in sooting flame can be thought that more consumption than formation of $^1CH_2$ in highly rich flames especially in sooting flames. This also can indicate and highlight the importance of the pathway of $^1CH_2$ to C_3H_3 that may promote unsaturated hydrocarbons to form higher hydrocarbons in the sooting flames. We can also explain that the more $^1CH_2$ radical is formed than decomposed in the zone between 0 mm and 1.2 mm while less $^1CH_2$ radical is formed than decomposed in the zone after 1.2 mm, and the highest $^1CH_2$ concentration in sooting flames is at about 1.2 mm above the burner surface. As for the maximal concentration value, a factor of 2 is found between the experiment and simulation using the ABF mechanism. This discrepancy is considerably greater than could be explained by the uncertainty in the absorption cross-section.

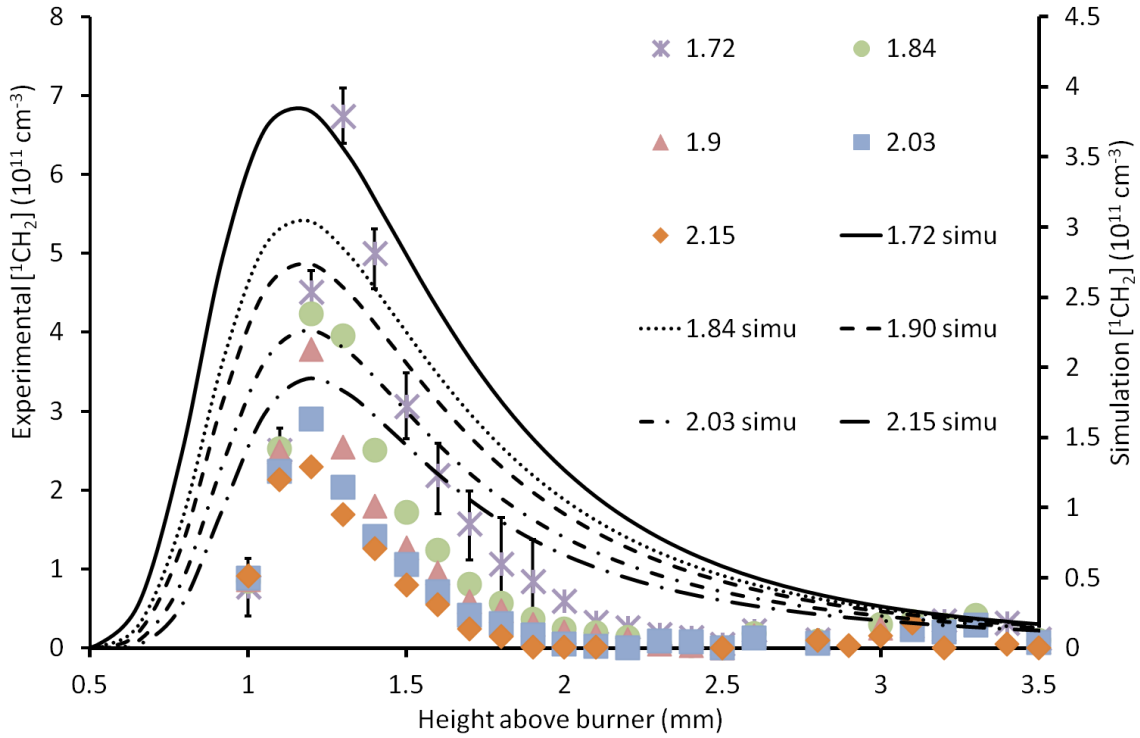

Figure 6.8: Comparison of experimental $^1CH_2$ concentration profiles and ABF-simulations vs height above the burner surface and fuel equivalence ratios.

6.8 HCO profiles comparison

The formyl radical (HCO) plays a key role in hydrocarbon combustion process. Decomposition and abstraction reactions of CH_2O primarily determine its density. HO_2 which is formed by the reaction of HCO and O_2 in early combustion process is believed to inhibit ignition and slow the flame (Najm et al., 1998, Jeffries et al., 1991). Moreover,

it may play a key role to reduce the radical pool as well as the flame speed by chain-terminating reacting with H, CH_3, and OH (Schocker et al., 2005). The main reactions are listed below for illustration.

$$HCO + M \rightleftarrows CO + H + M \quad (6.29)$$

$$HCO + H \rightleftarrows CO + H_2 \quad (6.30)$$

$$HCO + O \rightleftarrows CO + OH \quad (6.31)$$

$$HCO + O \rightleftarrows CO_2 + H \quad (6.32)$$

$$HCO + OH \rightleftarrows CO + H_2O \quad (6.33)$$

$$HCO + O_2 \rightleftarrows CO + HO_2 \quad (6.34)$$

$$HCO + HCO \rightleftarrows CH_2O + CO \quad (6.35)$$

Temporal and spatial correlations were reported between the distribution of HCO, the overall burning rate and the total heat release in a hydrocarbon combustion process (Najm et al., 1998).

As for the HCO concentration profiles, these profiles were also shifted by 0.3 mm to compensate for a slight offset in height scale for the CRDS measurements for better demonstration in the same figure. Thus, the simulation profiles are shown in the same figure (Figure 6.9) for comparison. There is good agreement between the experiment and simulation regarding the shapes of the HCO concentration profiles in different flame conditions. However, the simulation values seem to be deviated by a factor of 1.5 by which the simulations underestimate the experimental data. And experimental and simulated positions of the maximal HCO concentration differ by 0.3 mm in the flames. The positions of maximum concentrations appear to be shifted slightly upwards in the flame with increasing equivalence ratio both in the experimental and simulation results. The positions of the maximum concentrations observed experimentally are slightly more sensitive to equivalence ration than is shown in the simulation result. In addition, the half-width of the zone in which HCO is detectable seems to be the same as the simulations. Moreover, both of results indicate that the maximal absolute concentrations of HCO remain the same with the increasing of the fuel equivalence ratio.

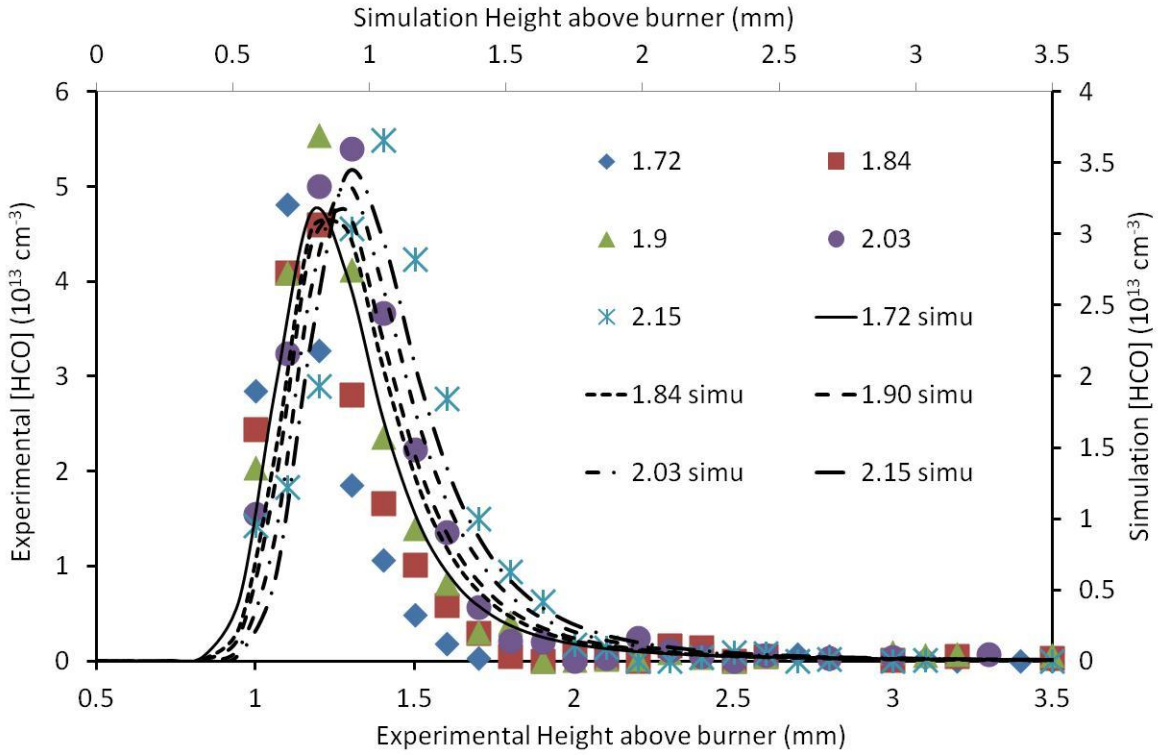

Figure 6.9: Comparison of experimental HCO concentration profiles and ABF-simulations vs height above the burner surface and fuel equivalence ratios.

CHAPTER 7: CONCLUSIONS AND FUTURE WORKS

7.1 Conclusions

7.1.1 Overall Conclusion

Although there has been considerable study of hydrocarbon combustion, the data of kinetics are still insufficient to describe the reliable reaction mechanism especially for sooting flames. Many attempts to describe sooting flame reaction mechanisms have been based on limited experimental data. This thesis presents the results of temperature profiles measured by laser induced fluorescence; quantitative measurements of singlet methylene ($^1CH_2$) and formyl (HCO) by cavity-ring down spectroscopy; and hydroxyl radical (OH) data by both laser induced fluorescence and cavity-ring down spectroscopy in laminar, premixed, sooting flames stabilised porous-plug burner. These results compared with the simulated profiles generated by using ABF reaction mechanism (Appel et al., 2000) in this study and can be important data for further modelling construction and validation. Generally, there is good quantitative agreement for the OH, HCO and $^1CH_2$concentration profiles. This discrepancy is greater than could be explained by the estimated measurement error resulting from uncertainty in the transition line strength data. The ABF mechanism is widely used as a

basis for soot formation studies. In the region downstream of the reaction zone weak absorption was observed due by CRDS, which rises with increasing height above burner and with increasing equivalence ratio. This broadband absorption was observed upstream of the onset of soot formation and may be attributable to large PAH molecules or nano-scale clusters. The detailed conclusion and suggestion for future work are discussed below.

7.1.2 OH LIF

Suitable experimental flame conditions were chosen to produce laminar premixed sooting flames. In each flame, the velocity of the C_2H_4/air mixture at the exit of the burner was at the same value, corresponding to the chosen equivalence ratio ($\Phi = 1.72 - 2.15$). Experimental and theoretical studies of the correlation between OH fluorescence and its concentration as well as the flame temperature were conducted in the flat flame.

At first, OH LIF linear regime has been confirmed to ensure all of the LIF experimental work not saturated. And then, spectra have been obtained by excitating both

$A^2\sum(v^{'}=0) \leftarrow X^2\prod(v^{''}=0)$ and $A^2\sum(v^{'}=1) \leftarrow X^2\prod(v^{''}=0)$ bands in the ranges 282.8 -- 284 nm and 302.5 -- 304.5 nm respectively. $A^2\sum(v^{'}=0) \leftarrow X^2\prod(v^{''}=0)$ band was selected for the further OH LIF thermometry and concentration measurement after careful comparison due to its well-isolated rotational lines and the flexibility and compatibility for 622 nm CRDS measurements of HCO and $^1CH_2$.

Low OH concentration, attenuation of the incident beam and signal trapping, various interferences were occurring in sooting flames when employing laser diagnostics. Because there is much more intense luminosity, and broadband soot incandescence and PAH fluorescence signals when soot present in flames. Spatially-resolved profiles of OH LIF were obtained by exciting both the $S_{21}(5)$ and $Q_1(6)$ resonance lines. In sooting flames, quantitative laser measurements of OH is made difficult by the presence of soot particles and PAHs, which can also absorb or scatter the broadband incident laser light. Therefore, reference measurements have been performed in order to compensate for these interferences. The resulting OH net LIF intensity by excitating $S_{21}(5)$ increases to its maximum at 1.1 mm and then decreases to a stable value with the height increases. These qualitative results will be calibrated to the absolute values by CRDS below. Moreover, efforts have been made to get a detailed flame horizontal profile in order to check how flat the flames are. By using the same on- and off- measurement procedures,

the flame horizontal region has been proved to be about 16 mm radius up to 2.1 mm above the burner surface which agrees with our burner surface dimensions.

7.1.3 Temperature

The profile of the temperature distribution is of importance in the simulation of the combustion process by numerical modelling and for comparison of experimental data with the modelling predictions. Accurate, highly resolved measurement of temperature is one of the essential tasks in combustion diagnostics. The principle of OH LIF thermometry by Boltzmann plotting method has already discussed firstly. The OH spectrum was measured by scanning a dye laser along rotational transitions. I_{LIF} are the relative OH fluorescence signals collected by at each peak line of S_{21} (*N = 5, 6, 7, 8, 9, 10, 11*). In order to obtain detailed temperature profiles in these sooting flames, the on- and off- resonance measurement procedure was followed. The net OH LIF profiles in sooting flames were thus obtained by subtracting reference (off-resonance) measurements from the on-resonance ones. The temperature profiles from the fluorescence signals were determined as the inverse proportion of the slopes at each flame condition and position. No significant difference of the temperature profiles was observed between different sooting flame conditions within the detectable range. The

average temperature can be found at around 1600 K at the flat-curve stage. The error increases with increasing of the height above burner surface. The net OH fluorescence intensity increases to its maximum at 1.1 mm and then decreases to a stable value with the height increases. However, the background noise signals increase continually with the height above burner in sooting flames. This temperature profiles were used in the experiments and calibration of CRDS measurement. By comparing with the profiles generated by ABF mechanism, a good agreement of temperature profiles behaviour can be observed. The simulated temperature is slightly higher than experimental one.

7.1.4 $^1CH_2$

In the CRDS experiment section, CRDS calibration and quantitative calculation methods have been reviewed at first, and then summarised into a four-step experimental procedure and an equation to calculate the total density of a molecule. The total losses of the cavity were examined both at-resonance and off-resonance in order to obtain the absolute concentration of a radical from this chemical-complex environment which have many non-negligible interferes, such as PAH absorption and soot extinction. $^1CH_2$ has been spectroscopically reviewed and the spectrum was obtained by CRDS in the range between 622.1 nm and 622.8 nm. The $^rQ_{0,7}$ excitation line was selected for the

concentration measurements due to the isolation and known cross-section (Derzy et al., 1999). The resulting absolute concentration profiles of $^1CH_2$ were obtained in sooting flame. The $^1CH_2$ is located in a thin layer close to the burner surface, near the reaction zone of the laminar flame. The $^1CH_2$ zone is narrowing with the increasing of fuel equivalence ratio. Results of simulations for $^1CH_2$ radical were compared with the experimental profile. Generally, these behaviours have been found good agreement between experiment and simulation. The simulated profiles are considerably boarder than the experimental ones, indicating that the rates of some reactions consuming $^1CH_2$ may be underestimated. The positions of maximum concentrations appear to stay the same positions in the flame while the maximum concentration decreases with increasing stoichiometry in both experimental and simulated graphs. This trend of $^1CH_2$ concentration profiles in sooting flame can be thought that more consumption than formation of $^1CH_2$ in highly rich flames especially in sooting flames. This also can indicate and highlight the importance of the pathway of $^1CH_2$ to C_3H_3 that may promote unsaturated hydrocarbons to form higher hydrocarbons in the sooting flames.

7.1.5 HCO

HCO was also spectroscopically reviewed and the spectrum was achieved in the range between 615.6 nm and 616.5 nm. The resulting absolute concentration profiles of HCO were obtained in sooting flame by probing the P(9) excitation line. The HCO is also located in a thin layer close to the burner surface, comprising the reaction zone of the laminar flame. Again, there is good agreement between the experiment and simulation regarding the maximum HCO concentration in different flame conditions. However, the simulation values seem to be deviated by a factor of two by which the simulations underestimate the experimental data. And experimental and simulated positions of the maximal HCO concentration differ by 0.3 mm in the flames. The positions of maximum concentrations appear to be shifted slightly upwards in the flame with increasing equivalence ratio both in the experimental and simulation results. The positions of the maximum concentrations observed experimentally are slightly more sensitive to equivalence ration than is shown in the simulation result. In addition, the half-width of the zone in which HCO is detectable seems to be the same as the simulations. Moreover, both of results indicate that the maximal absolute concentrations of HCO remain the same with the increasing of the fuel equivalence ratio. Moreover, the fractional losses per pass measured off-resonance are plotted as a function of height above burner. Significant losses were observed with increasing height above burner and these are

greatest for the richest flames. This highlighted the potential of cavity-ring down measurements for the study of broad-band absorbers in flames as well as small radicals.

7.1.6 OH CRDS

The main advantages of fluorescence detection are the high sensitivity and favourable spatial resolution achievable. However, the main problem is on the determination of the fluorescence quantum yield. The fluorescence intensity and spectral distribution are affected by collision processes when excited with a pulsed laser. In addition, the local collision efficiency that affects the fluorescence quantum yield is influenced by pressure, temperature and chemical composition at the observation volume. Therefore, the fluorescence quantum yield varies significantly with position, and it thus makes quantitative LIF measurements difficult in such environments. OH qualitative concentration profiles have been obtained by LIF. The OH CRDS measurement here was used to quantify the profiles obtained from OH LIF measurements, and all of the absolute concentration values were calibrated by the peak value at 1 mm and the fuel equivalence ratio of 1.72 from OH CRDS. Although OH LIF concentration values are calibrated at one condition and position, the other CRDS values still reasonably match the calibrated points even in these low OH concentration and high background

interferences environments. The results were also compared with the simulated ones. Overall, these behaviours of OH profiles have been found good agreement between experiment and simulation. The position of maximal concentrations and profile behaviours match well between them. The positions of maximum concentrations for each fuel equivalence ratio observed experimentally appear to be slightly closer to the burner surface in the flame, while the experimental maximal concentrations for each fuel equivalence ratio seem to be slightly higher than the simulated ones. This discrepancy is considerably greater that could be explained by the high OH LIF/CRDS signal to background ratios. The positions of maximum concentrations observed experimentally appear to be shifted very slightly upwards in the flame with increasing equivalence ratio. This is consistent with expectations since the cold gas velocity has been held constant. However, it does not appear in the simulated profiles. Moreover, the simulated profiles are considerably boarder than the experimental ones, indicating that the rates of some reactions consuming OH may be underestimated. What's more, the OH concentration profiles increases to its maximum at around 1.1 mm and then decreases to a stable value with the height increases in both experimental and simulated graphs.

7.2 Suggestions for Further Research

No single laser technique is capable of measuring all species and temperatures simultaneously; several complementary approaches may have to be combined to characterize the medium to the extent desired. Laser spectroscopic techniques tend to be most applicable to small molecules. For large molecules, the spectroscopy is often very complicated.

In chapter 4, low OH concentration, attenuation of the incident beam and signal trapping, various interferences were occurring in sooting flames when employing LIF to detect OH fluorescence. The on- and off- resonance measurement strategy was used to obtain net OH fluorescence while get rid of the unwanted interferences. However, the off-resonance LIF measurements may be useful for PAH and soot formation studies. Although the role of PAHs in soot nucleation and growth is now well established, the crucial step from the molecular phase to nascent particles is still unknown and interested. Without a full understanding of the inception process, many kinetics models assume the first particles to be formed from coalescence of two gaseous PAHs (Bladh et al., 2014). The off-resonance LIF signals contain both soot incandescence and PAH

fluorescence signals. Laser-Induced Incandescence (LII) takes place when laser beam hit soot. As the soot is heated up by the beam, their temperature increases and the soot particles will reach incandescent temperatures (4000 K) and produce near-blackbody emission. The radiation emitted is nearly proportional to soot volume fractions (Santoro and Shaddix, 2002). However, the LII signals of PAHs may be interfered by PAHs LIF signals. When employing LII technique to determine particles size, the net LII signals may be calibrated by subtracting LIF from LII signals. Thus, the coupling use of LII and LIF may be useful to study the mechanism from nascent particles to soot particles.

In chapter 5, CRDS has been proved to be a powerful tool to detect small molecules in very low concentration even in sooting flame. However, it is very difficult to detect the radicals very closed to the burner surface due to the thermal effects and deflections of the laser beam. Also, the stabilization plate introduces more interference in this kind of burner. Therefore, more efforts may be contributed to study combustion chemistry in sooting flame from a counterflow diffusion flame burner (Lefkowitz et al., 2012, Niemann et al., 2014, Wang et al., 2013). These results may help to study PAHs formation in the oxygen-starved regions of combustors.

C_2 fuel was chosen because its mechanism is reasonably well known and is a good guide to the behaviour of other hydrocarbons. However, an attempt to model comprehensively the combustion of complex practical fuels is still a difficult and frequently controversial task. Propane is an important practical fuel widely used throughout the world. It is generally accepted that propane is the simplest hydrocarbon that has reaction characteristics representative of many technical fuels, including jet fuels. Therefore, from a modelling perspective, a propane combustion mechanism that has been assembled and evaluated against experimental data would be a valuable research tool for analyzing and interpreting any other combustion experiments involving typical hydrocarbon fuels. This mechanism would be especially valuable in connection with experiments in which propane is used as a surrogate hydrocarbon fuel. However, the intermediate species are much more difficult to be detected in higher hydrocarbon fuels due to more complex environments than simple hydrocarbons, especially in sooting flames. Thus, it is interesting to use propane in premixed flat burner and/or counterflow diffusion flame burner to study the intermediate species in order to contribute the practical fuel combustion mechanism construction and validation.

REFERENCE

ADKINS, E. M., HERDMAN, J. A. & MILLER, J. H. 2013. Experimental and computational determinations of optical band gaps for PAH and soot in N2-diluted, ethylene/air non-premixed flames.

ALDÉN, M., BOOD, J., LI, Z. & RICHTER, M. 2011. Visualization and understanding of combustion processes using spatially and temporally resolved laser diagnostic techniques. Proceedings of the Combustion Institute, 33, 69-97.

ANDRESEN, P., BATH, A., GRÖGER, W., LÜLF, H., MEIJER, G. & MEULEN, J. J. 1988. Laser-induced fluorescence with tunable excimer lasers as a possible method for instantaneous temperature field measurements at high pressures: checks with an atmospheric flame. Applied Optics, 27, 365-378.

APICELLA, B., CARPENTIERI, A., ALFÈ, M., BARBELLA, R., TREGROSSI, A., PUCCI, P. & CIAJOLO, A. 2007. Mass spectrometric analysis of large PAH in a fuel-rich ethylene flame. Proceedings of the Combustion Institute, 31, 547-553.

APPEL, J., BOCKHORN, H. & FRENKLACH, M. 2000. Kinetic modeling of soot formation with detailed chemistry and physics: laminar premixed flames of C< sub> 2</sub> hydrocarbons. Combustion and Flame, 121, 122-136.

APPEL, J., BOCKHORN, H. & WULKOW, M. 2001. A detailed numerical study of the evolution of soot particle size distributions in laminar premixed flames. Chemosphere, 42, 635-645.

ATAKAN, B., LAMPRECHT, A. & KOHSE-HOINGHAUS, K. 2003. An experimental study of fuel-rich 1,3-pentadiene and acetylene/propene flames. Combustion and Flame, 133, 431-440.

ATKINS, P. & DE PAULA, J. 2010. Atkins' Physical Chemistry, OUP Oxford.

BABUSHOK, V. & TSANG, W. 2004. Kinetic modeling of heptane combustion and PAH formation. Journal of propulsion and power, 20, 403-414.

BADRA, J., MASRI, A. R., ZHOU, C. & HAYNES, B. S. 2013. An experimental and numerical study of surface chemical interactions in the combustion of propylene over platinum. Combustion and Flame, 160, 473-485.

BALTHASAR, M. & FRENKLACH, M. 2005a. Detailed kinetic modeling of soot aggregate formation in laminar premixed flames. Combustion and Flame, 140, 130-145.

BALTHASAR, M. & FRENKLACH, M. 2005b. Monte-Carlo simulation of soot particle coagulation and aggregation: the effect of a realistic size distribution. Proceedings of the Combustion Institute, 30, 1467-1475.

BALTHASAR, M. & KRAFT, M. 2003. A stochastic approach to calculate the particle size distribution function of soot particles in laminar premixed flames. Combustion and Flame, 133, 289-298.

BARLOW, R., DIBBLE, R. & LUCHT, R. P. 1989. Simultaneous measurement of Raman scattering and laser-induced OH fluorescence in nonpremixed turbulent jet flames. Optics Letters, 14, 263-265.

BASILE, G., ROLANDO, A., D'ALESSIO, A., D'ANNA, A. & MINUTOLO, P. 2002. Coagulation and carbonization processes in slightly sooting premixed flames. Proceedings of the Combustion Institute, 29, 2391-2397.

BEJAOUI, S., MERCIER, X., DESGROUX, P. & THERSSEN, E. 2014. Laser induced fluorescence spectroscopy of aromatic species produced in atmospheric sooting flames using UV and visible excitation wavelengths. Combustion and Flame.

BERDEN, G. & ENGELN, R. 2009. Cavity Ring-Down Spectroscopy: Techniques and Applications, Wiley.

BERDEN, G., PEETERS, R. & MEIJER, G. 2000. Cavity ring-down spectroscopy: Experimental schemes and applications. International Reviews in Physical Chemistry, 19, 565-607.

BERG, P. A., HILL, D. A., NOBLE, A. R., SMITH, G. P., JEFFRIES, J. B. & CROSLEY, D. R. 2000. Absolute CH concentration measurements in low-pressure methane flames: Comparisons with model results. Combustion and Flame, 121, 223-235.

BERGMANN, V., MEIER, W., WOLFF, D. & STRICKER, W. 1998. Application of spontaneous Raman and Rayleigh scattering and 2D LIF for the characterization of a turbulent CH4/H2/N2 jet diffusion flame. Applied Physics B, 66, 489-502.

BERNATH, P. F. 2005. Spectra of atoms and molecules, Oxford University Press.

BLADH, H., JOHNSSON, J. & BENGTSSON, P. E. 2009. Influence of spatial laser energy distribution on evaluated soot particle sizes using two-colour laser-induced incandescence in a flat premixed ethylene/air flame. Applied Physics B: Lasers and Optics, 96, 645-656.

BLADH, H., OLOFSSON, N.-E., MOUTON, T., SIMONSSON, J., MERCIER, X., FACCINETTO, A., BENGTSSON, P.-E. & DESGROUX, P. 2014. Probing the smallest soot particles in low-sooting premixed flames using laser-induced incandescence. Proceedings of the Combustion Institute.

BLEVINS, L. G., FLETCHER, R. A., BENNER JR, B. A., STEEL, E. B. & MULHOLLAND, G. W. 2002. The existence of young soot in the exhaust of inverse diffusion flames. Proceedings of the Combustion Institute, 29, 2325-2333.

BORMAN, G. L. & RAGLAND, K. W. 1998. Combustion Engineering, McGraw-Hill.

BOUVIER, Y., MIHESAN, C., ZISKIND, M., THERSSEN, E., FOCSA, C., PAUWELS, J. & DESGROUX, P. 2007. Molecular species adsorbed on soot particles issued from low sooting methane and acetylene laminar flames: A laser-based experiment. Proceedings of the Combustion Institute, 31, 841-849.

BROWN, J. & RAMSAY, D. 1975. Axis Switching in the Transition of HCO: Determination of Molecular Geometry. Canadian Journal of Physics, 53, 2232-2241.

BURCAT, A. & MCBRIDE, B. J. 1993. 1994 Ideal Gas Thermodynamic Data for Combustion and Air Pollution Use, Technion-IIT, Faculty of Aerospace Engineering.

BURNS, I. S., MERCIER, X., WARTEL, M., CHRYSTIE, R. S., HULT, J. & KAMINSKI, C. F. 2011. A method for performing high accuracy temperature measurements in low-pressure sooting flames using two-line atomic fluorescence. Proceedings of the Combustion Institute, 33, 799-806.

CATTOLICA, R. 1981. OH rotational temperature from two-line laser-excited fluorescence. Applied Optics, 20, 1156-1166.

CATTOLICA, R. & SCHEFER, R. 1983. Laser Fluorescence Measurements of the OH Concentration in a Combustion Boundary Layer†. Combustion Science and Technology, 30, 205-212.

CHAN, C. & DAILY, J. W. 1980. Measurement of temperature in flames using laser induced fluorescence spectroscopy of OH. Applied Optics, 19, 1963-1968.

CHAN, Q. N., MEDWELL, P. R., ALWAHABI, Z. T., DALLY, B. B. & NATHAN, G. J. 2011. Assessment of interferences to nonlinear two-line atomic fluorescence (NTLAF) in sooty flames. Applied Physics B, 104, 189-198.

CHESKIS, S. 1995. INTRACAVITY LASER-ABSORPTION SPECTROSCOPY DETECTION OF HCO RADICALS IN ATMOSPHERIC-PRESSURE HYDROCARBON FLAMES. Journal of Chemical Physics, 102, 1851-1854.

CHESKIS, S., DERZY, I., LOZOVSKY, V. A., KACHANOV, A. & STOECKEL, F. 1997. Intracavity laser absorption spectroscopy detection of singlet CH2 radicals in hydrocarbon flames. Chemical Physics Letters, 277, 423-429.

CHESKIS, S. & GOLDMAN, A. 2009. Laser diagnostics of trace species in low-pressure flat flame. Progress in Energy and Combustion Science, 35, 365-382.

CHIGIER, N. 1991. Combustion measurements, CRC Press.

CIAJOLO, A., BARBELLA, R., TREGROSSI, A. & BONFANTI, L. Year. Spectroscopic and compositional signatures of PAH-loaded mixtures in the soot inception region of a premixed ethylene flame. In: Symposium (International) on Combustion, 1998. Elsevier, 1481-1487.

COMEAU, D. C., SHAVITT, I., JENSEN, P. & BUNKER, P. R. 1989a. An ab initio determination of the potential‐energy surfaces and rotation‐vibration energy levels of methylene in the lowest triplet and singlet states and the singlet‐triplet splitting. The Journal of Chemical Physics, 90, 6491.

COMEAU, D. C., SHAVITT, I., JENSEN, P. & BUNKER, P. R. 1989b. AN ABINITIO DETERMINATION OF THE POTENTIAL-ENERGY SURFACES AND ROTATION VIBRATION ENERGY-LEVELS OF METHYLENE IN THE LOWEST TRIPLET AND SINGLET-STATES AND THE SINGLET TRIPLET SPLITTING. Journal of Chemical Physics, 90, 6491-6500.

CROSLEY, D. R. & CHEMISTRY, A. C. S. D. O. P. 1980. Laser probes for combustion chemistry, The Society.

D'ANNA, A. & KENT, J. 2003. Aromatic formation pathways in non-premixed methane flames. Combustion and Flame, 132, 715-722.

DAILY, J. W. 1976. Pulsed resonance spectroscopy applied to turbulent combustion flows. Applied Optics, 15, 955-960.

DAILY, J. W. 1997. Laser induced fluorescence spectroscopy in flames. Progress in Energy and Combustion Science, 23, 133-199.

DERZY, I., LOZOVSKY, V. A. & CHESKIS, S. 1999. Absorption cross-sections and absolute concentration of singlet methylene in methane/air flames. Chemical Physics Letters, 313, 121-128.

DESGROUX, P., MERCIER, X., LEFORT, B., LEMAIRE, R., THERSSEN, E. & PAUWELS, J. 2008. Soot volume fraction measurement in low-pressure methane flames by combining laser-induced incandescence and cavity ring-down spectroscopy: Effect of pressure on soot formation. Combustion and Flame, 155, 289-301.

DESGROUX, P., MERCIER, X. & THOMSON, K. A. 2013. Study of the formation of soot and its precursors in flames using optical diagnostics. Proceedings of the Combustion Institute, 34, 1713-1738.

DIAU, E. W.-G., SMITH, G. P., JEFFRIES, J. B. & CROSLEY, D. R. Year. HCO concentration in flames via quantitative laser-induced fluorescence. In: Symposium (International) on Combustion, 1998. Elsevier, 453-460.

DIEKE, G. & CROSSWHITE, H. 1962. The ultraviolet bands of OH fundamental data. Journal of Quantitative Spectroscopy and Radiative Transfer, 2, 97-199.

DIXON-LEWIS, G. 1967. Flame structure and flame reaction kinetics. I. Solution of conservation equations and application to rich hydrogen-oxygen flames. Proceedings of the Royal Society of London. Series A. Mathematical and Physical Sciences, 298, 495-513.

DIXON-LEWIS, G. 1970. Flame structure and flame reaction kinetics. V. Investigation of reaction mechanism in a rich hydrogen+ nitrogen+ oxygen flame by solution of conservation equations. Proceedings of the Royal Society of London. A. Mathematical and Physical Sciences, 317, 235-263.

DREYER, C. B., SPULER, S. M. & LINNE, M. 2001. Calibration of laser induced fluorescence of the OH radical by cavity ringdown spectroscopy in premixed atmospheric pressure flames. Combustion Science and Technology, 171, 163-190.

ECKBRETH, A. C. 1996. Laser diagnostics for combustion temperature and species, CRC Press.

EMELIANOV, A., EREMIN, A., JANDER, H., WAGNER, H. & BORCHERS, C. 2002. Spectral and structural properties of carbon nanoparticle forming in C< sub>

3</sub> O< sub> 2</sub> and C< sub> 2</sub> H< sub> 2</sub> pyrolysis behind shock waves. Proceedings of the Combustion Institute, 29, 2351-2357.

ENGELN, R., VON HELDEN, G., BERDEN, G. & MEIJER, G. 1996. Phase shift cavity ring down absorption spectroscopy. Chemical Physics Letters, 262, 105-109.

EVERTSEN, R., STOLK, R. L. & TER MEULEN, J. J. 1999. Investigations of Cavity Ring Down Spectroscopy applied to the detection of CH in atmospheric flames. Combustion Science and Technology, 149, 19-34.

EVERTSEN, R., VAN OIJEN, J., HERMANNS, R., DE GOEY, L. & TER MEULEN, J. 2003a. Measurements of the absolute concentrations of HCO and 1CH2 in a premixed atmospheric flat flame by cavity ring-down spectroscopy. Combustion and Flame, 135, 57-64.

EVERTSEN, R., VAN OIJEN, J. A., HERMANNS, R. T. E., DE GOEY, L. P. H. & TER MEULEN, J. J. 2003b. Measurements of absolute concentrations of CH in a premixed atmospheric flat flame by cavity ring-down spectroscopy. Combustion and Flame, 132, 34-42.

EWART, P. & O'LEARY, S. 1986. Detection of OH in a flame by degenerate four-wave mixing. Optics Letters, 11, 279-281.

FOGLER, H. S. 2006. Elements of Chemical Reaction Engineering, Prentice Hall PTR.

FRENKLACH, M. 2002. Reaction mechanism of soot formation in flames. Physical Chemistry Chemical Physics, 4, 2028-2037.

FRENKLACH, M., WANG, H., YU, C., GOLDENBERG, M., BOWMAN, C., HANSON, R., DAVIDSON, D., CHANG, E., SMITH, G. & GOLDEN, D. 1995. Gri-mech 1.2-an optimized detailed chemical reaction mechanism for methane combustion. GRI Tech. Report GRI-95/0058.

FRISTROM, R. M. & WESTENBERG, A. A. 1965. Flame structure, McGraw-Hill.

FURUYA, Y., YAMAMOTO, M. & TAKUBO, Y. 1985. Rotational Energy Transfer in A2Σv'= 0 State of OH in Flame: On the Use of Laser-Induced Fluorescence Spectrum for Flame Temperature Measurement. Japanese Journal of Applied Physics, 24, 455.

GARCÍA-MORENO, I. & MOORE, C. B. 1993. Spectroscopy of methylene: Einstein coefficients for CH2 (b̃ 1B1–ã 1A1) transitions. The Journal of Chemical Physics, 99, 6429-6435.

GASNOT, L., DESGROUX, P., PAUWELS, J. & SOCHET, L. 1999. Detailed analysis of low-pressure premixed flames of CH< sub> 4</sub>+ O< sub> 2</sub>+ N< sub> 2</sub>: a study of prompt-NO. Combustion and Flame, 117, 291-306.

GLASSMAN, I. & YETTER, R. 2008. Combustion, Elsevier Science.

GOODWIN, D. An open-source, extensible software suite for CVD process simulation.

GRIESHEIMER, J. & HOMANN, K.-H. Year. Large molecules, radicals ions, and small soot particles in fuel-rich hydrocarbon flames: Part II. Aromatic radicals and

intermediate PAHs in a premixed low-pressure naphthalene/oxygen/argon flame. In: Symposium (International) on Combustion, 1998. Elsevier, 1753-1759.

HANSON, R. K. 1977. SHOCK-TUBE SPECTROSCOPY - ADVANCED INSTRUMENTATION WITH A TUNABLE DIODE-LASER. Applied Optics, 16, 1479-1481.

HANSON, R. K. Year. Combustion diagnostics: planar imaging techniques. In: Symposium (International) on Combustion, 1988. Elsevier, 1677-1691.

HARTLIEB, A. T., ATAKAN, B. & KOHSE-HOINGHAUS, K. 2000a. Effects of a sampling quartz nozzle on the flame structure of a fuel-rich low-pressure propene flame. Combustion and Flame, 121, 610-624.

HARTLIEB, A. T., ATAKAN, B. & KOHSE-HÖINGHAUS, K. 2000b. Effects of a sampling quartz nozzle on the flame structure of a fuel-rich low-pressure propene flame. Combustion and Flame, 121, 610-624.

HERZBERG, G. Molecular spectra and molecular structure, Vol. 1.

HERZBERG, G. 1971. The spectra and structures of simple free radicals: an introduction to molecular spectroscopy, Courier Dover Publications.

HERZBERG, G. & JOHNS, J. 1966a. The Spectrum and Structure of Singlet CH $ _2$. Proceedings of the Royal Society of London. Series A. Mathematical and Physical Sciences, 295, 107-128.

HERZBERG, G. & JOHNS, J. W. C. 1966b. SPECTRUM AND STRUCTURE OF SINGLET CH2. Proceedings of the Royal Society of London Series a-Mathematical and Physical Sciences, 295, 107-&.

HERZBERG, G. & RAMSAY, D. 1955. The 7500 to 4500 angstrom Absorption System of the Free HCO Radical. Proceedings of the Royal Society of London. Series A. Mathematical and Physical Sciences, 233, 34-54.

HILBORN, R. C. 2002. Einstein coefficients, cross sections, f values, dipole moments, and all that. Arxiv preprint physics/0202029.

HIRSCHFELDER, J., CURTISS, C. & CAMPBELL, D. E. 1953. The theory of flame propagation. IV. The Journal of Physical Chemistry, 57, 403-414.

HIRSCHFELDER, J. O., CURTISS, C. F., BIRD, R. B. & LABORATORY, U. O. W. T. C. 1954. Molecular theory of gases and liquids, Wiley.

HODGES, J. T., LOONEY, J. P. & VAN ZEE, R. D. 1996. Laser bandwidth effects in quantitative cavity ring-down spectroscopy. Applied Optics, 35, 4112-4116.

HOLLAS, J. M. Year. High resolution spectroscopy. In: High resolution spectroscopy/J. Michael Hollas. Chichester; New York: J. Wiley, c1998., 1998.

HOYERMANN, K., MAUSS, F. & ZEUCH, T. 2004. A detailed chemical reaction mechanism for the oxidation of hydrocarbons and its application to the analysis of benzene formation in fuel-rich premixed laminar acetylene and propene flames. Physical Chemistry Chemical Physics, 6, 3824-3835.

JEFFRIES, J. B., CROSLEY, D. R., WYSONG, I. J. & SMITH, G. P. Year. Laser-induced fluorescence detection of HCO in a low-pressure flame. In: Symposium (International) on Combustion, 1991. Elsevier, 1847-1854.

JOHNS, J., PRIDDLE, S. & RAMSAY, D. 1963. Electronic absorption spectra of HCO and DCO radicals. Discussions of the Faraday Society, 35, 90-104.

JONGMA, R. T., BOOGAARTS, M. G., HOLLEMAN, I. & MEIJER, G. 1995. Trace gas detection with cavity ring down spectroscopy. Review of Scientific Instruments, 66, 2821-2828.

JUCHMANN, W., LATZEL, H., SHIN, D., PEITER, G., DREIER, T., VOLPP, H.-R., WOLFRUM, J., LINDSTEDT, R. & LEUNG, K. Year. Absolute radical concentration measurements and modeling of low-pressure CH< sub> 4</sub>/O< sub> 2</sub>/NO flames. In: Symposium (International) on Combustion, 1998. Elsevier, 469-476.

KADOWAKI, S. & HASEGAWA, T. 2005. Numerical simulation of dynamics of premixed flames: flame instability and vortex–flame interaction. Progress in Energy and Combustion Science, 31, 193-241.

KAMPHUS, M., LIU, N.-N., ATAKAN, B., QI, F. & MCILROY, A. 2002. REMPI temperature measurement in molecular beam sampled low-pressure flames. Proceedings of the Combustion Institute, 29, 2627-2633.

KAZAKOV, A., WANG, H. & FRENKLACH, M. 1995. Detailed modeling of soot formation in laminar premixed ethylene flames at a pressure of 10 bar. Combustion and Flame, 100, 111-120.

KEE, R., RUPLEY, F. & MILLER, J. 1989. Technical Report SAND89-8009 (CHEMKIN-II). Sandia National Laboratories, Livermore, CA.

KEE, R. J., GRCAR, J. F., SMOOKE, M. & MILLER, J. 1985. PREMIX: a Fortran program for modeling steady laminar one-dimensional premixed flames. Sandia National Laboratories Report.

KEE, R. J., MILLER, J. A. & JEFFERSON, T. H. 1980. CHEMKIN: A general-purpose, problem-independent, transportable, FORTRAN chemical kinetics code package, Sandia Laboratories.

KELLER, A., KOVACS, R. & HOMANN, K.-H. 2000. Large molecules, ions, radicals and small soot particles in fuel-rich hydrocarbon flames. Part IV. Large polycyclic aromatic hydrocarbons and their radicals in a fuel-rich benzene–oxygen flame. Physical Chemistry Chemical Physics, 2, 1667-1675.

KETTERLE, W., SCHÄFER, M., ARNOLD, A. & WOLFRUM, J. 1992. 2D single-shot imaging of OH radicals using tunable excimer lasers. Applied Physics B: Lasers and Optics, 54, 109-112.

KIRAN, D. & MISHRA, D. 2007. Experimental studies of flame stability and emission characteristics of simple LPG jet diffusion flame. Fuel, 86, 1545-1551.

KOHSE-HÖINGHAUS, K. 1990. Quantitative laser-induced fluorescence: Some recent developments in combustion diagnostics. Applied Physics B, 50, 455-461.

KOHSE-HÖINGHAUS, K. 1994. Laser techniques for the quantitative detection of reactive intermediates in combustion systems. Progress in Energy and Combustion Science, 20, 203-279.

KOHSE-HÖINGHAUS, K. 2002. Applied Combustion Diagnostics, Taylor & Francis.

KOHSE-HÖINGHAUS, K., BARLOW, R. S., ALDÉN, M. & WOLFRUM, J. 2005. Combustion at the focus: laser diagnostics and control. Proceedings of the Combustion Institute, 30, 89-123.

KOHSE-HÖINGHAUS, K., JEFFRIES, J. B., COPELAND, R. A., SMITH, G. P. & CROSLEY, D. R. Year. The quantitative LIF determination of OH concentrations in low-pressure flames. In, 1989. Elsevier, 1857-1866.

KOHSE-HOINGHAUS, K., SCHOCKER, A., KASPER, T., KAMPHUS, M. & BROCKHINKE, A. 2005. Combination of laser- and mass-spectroscopic techniques for the investigation of fuel-rich flames. Zeitschrift Fur Physikalische Chemie-International Journal of Research in Physical Chemistry & Chemical Physics, 219, 583-599.

KUO, K. K. 2005. Principles of combustion, John Wiley.

LACKNER, M., PALOTÁS, Á. & WINTER, F. 2013. Combustion: From Basics to Applications, Wiley.

LACKNER, M., WINTER, F. & AGARWAL, A. K. 2010. Handbook of Combustion, Wiley.

LAURENDEAU, N. M. 1988. Temperature measurements by light-scattering methods. Progress in Energy and Combustion Science, 14, 147-170.

LAW, C. K. 2005. Comprehensive description of chemistry in combustion modeling. Combustion Science and Technology, 177, 845-870.

LEFKOWITZ, J. K., HEYNE, J. S., WON, S. H., DOOLEY, S., KIM, H. H., HAAS, F. M., JAHANGIRIAN, S., DRYER, F. L. & JU, Y. 2012. A chemical kinetic study of< i> tertiary</i>-butanol in a flow reactor and a counterflow diffusion flame. Combustion and Flame, 159, 968-978.

LI, S., VARATHARAJAN, B. & WILLIAMS, F. 2001. Chemistry of JP-10 ignition. AIAA journal, 39, 2351-2356.

LINDSTEDT, P. Year. Modeling of the chemical complexities of flames. In: Symposium (International) on Combustion, 1998. Elsevier, 269-285.

LINDSTEDT, R. & RIZOS, K.-A. 2002. The formation and oxidation of aromatics in cyclopentene and methyl-cyclopentadiene mixtures. Proceedings of the Combustion Institute, 29, 2291-2298.

LONG, D. A. & LONG, D. 1977. Raman spectroscopy, McGraw-Hill New York.

LOZOVSKY, V. A., CHESKIS, S., KACHANOV, A. & STOECKEL, F. 1997. Absolute HCO concentration measurements in methane/air flame using intracavity laser spectroscopy. Journal of Chemical Physics, 106, 8384-8391.

LOZOVSKY, V. A., DERZY, I. & CHESKIS, S. Year. Radical concentration profiles in a low-pressure methane-air flame measured by intracavity laser absorption and cavity ring-down spectroscopy. In: Symposium (International) on Combustion, 1998a. Elsevier, 445-452.

LOZOVSKY, V. A., DERZY, I. & CHESKIS, S. 1998b. Radical concentration profiles in a low-pressure methane-air flame measured by intracavity laser absorption and cavity ring-down spectroscopy.

LUQUE, J. & CROSLEY, D. 1999. LIFBASE: Database and spectral simulation program (Version 1.5). SRI international report MP, 99.

LUQUE, J., KLEIN-DOUWEL, R., JEFFRIES, J., SMITH, G. & CROSLEY, D. 2002. Quantitative laser-induced fluorescence of CH in atmospheric pressure flames. Applied Physics B: Lasers and Optics, 75, 779-790.

MCILROY, A. 1998. Direct measurement of (CH2)-C-1 in flames by cavity ringdown laser absorption spectroscopy. Chemical Physics Letters, 296, 151-158.

MCILROY, A. 1999a. Laser studies of small radicals in rich methane flames: OH, HCO, and 1CH2. Israel Journal of Chemistry, 39, 55-62.

MCILROY, A. 1999b. Laser studies of small radicals in rich methane flames: OH, HCO, and (CH2)-C-1. Israel Journal of Chemistry, 39, 55-62.

MEHTA, R., HAWORTH, D. & MODEST, M. 2009. An assessment of gas-phase reaction mechanisms and soot models for laminar atmospheric-pressure ethylene–air flames. Proceedings of the Combustion Institute, 32, 1327-1334.

MERCIER, X., JAMETTE, P., PAUWELS, J. & DESGROUX, P. 1999a. Absolute CH concentration measurements by cavity ring-down spectroscopy in an atmospheric diffusion flame. Chemical Physics Letters, 305, 334-342.

MERCIER, X., PILLIER, L., EL BAKALI, A., CARLIER, M., PAUWELS, J.-F. & DESGROUX, P. 2002. NO reburning study based on species quantification obtained by coupling LIF and cavity ring-down spectroscopy. Faraday discussions, 119, 305-319.

MERCIER, X., THERSSEN, E., PAUWELS, J. & DESGROUX, P. 2001. Quantitative features and sensitivity of cavity ring-down measurements of species concentrations in flames. Combustion and Flame, 124, 656-667.

MERCIER, X., THERSSEN, E., PAUWELS, J. & DESGROUX, P. 2005. Measurements of absolute concentration profiles of C< sub> 2</sub> in non-sooting and sooting diffusion flames by coupling cavity ring-down spectroscopy and laser induced fluorescence. Proceedings of the Combustion Institute, 30, 1655-1663.

MERCIER, X., THERSSEN, E., PAUWELS, J. F. & DESGROUX, P. 1999b. Cavity ring-down measurements of OH radical in atmospheric premixed and diffusion flames. A comparison with laser-induced fluorescence and direct laser absorption. Chemical Physics Letters, 299, 75-83.

MILLER, J. A., PILLING, M. J. & TROE, J. 2005. Unravelling combustion mechanisms through a quantitative understanding of elementary reactions. Proceedings of the Combustion Institute, 30, 43-88.

MILLIKAN, R. C. 1962. Non-equilibrium soot formation in premixed flames. The Journal of Physical Chemistry, 66, 794-799.

MOREAU, C., THERSSEN, E., DESGROUX, P., PAUWELS, J. F., CHAPPUT, A. & BARJ, M. 2003. Quantitative measurements of the CH radical in sooting diffusion flames at atmospheric pressure. Applied Physics B-Lasers and Optics, 76, 597-602.

MOREAU, C. S., THERSSEN, E., MERCIER, X., PAUWELS, J. & DESGROUX, P. 2004. Two-color laser-induced incandescence and cavity ring-down spectroscopy for sensitive and quantitative imaging of soot and PAHs in flames. Applied Physics B, 78, 485-492.

MOSKALEVA, L. & LIN, M. 2002. Computational study of the kinetics and mechanisms for the reaction of H atoms with< i> c</i>-C< sub> 5</sub> H< sub> 6</sub>. Proceedings of the Combustion Institute, 29, 1319-1327.

NAIK, S. V. & LAURENDEAU, N. M. 2004. Measurements of absolute CH concentrations by cavity ring-down spectroscopy and linear laser-induced fluorescence in laminar, counterflow partially premixed and nonpremixed flames at atmospheric pressure. Applied Optics, 43, 5116-5125.

NAJM, H. N., PAUL, P. H., MUELLER, C. J. & WYCKOFF, P. S. 1998. On the adequacy of certain experimental observables as measurements of flame burning rate. Combustion and Flame, 113, 312-332.

NIEMANN, U., SESHADRI, K. & WILLIAMS, F. A. 2014. Methane, ethane, and ethylene laminar counterflow diffusion flames at elevated pressures: Experimental and computational investigations up to 2.0 MPa. Combustion and Flame, 161, 138-146.

NYGREN, J., ENGSTRÖM, J., WALEWSKI, J., KAMINSKI, C. & ALDÉN, M. 2001. Applications and evaluation of two-line atomic LIF thermometry in sooting combustion environments. Measurement Science and Technology, 12, 1294.

NYHOLM, K., FRITZON, R. & ALDÉN, M. 1993. Two-dimensional imaging of OH in flames by use of polarization spectroscopy. Optics Letters, 18, 1672-1674.

OKEEFE, A. & DEACON, D. A. G. 1988. CAVITY RING-DOWN OPTICAL SPECTROMETER FOR ABSORPTION-MEASUREMENTS USING PULSED LASER SOURCES. Review of Scientific Instruments, 59, 2544-2551.

PAKHOMYCHEVA, L., SVIRIDENKOV, E., SUCHKOV, A., TITOVA, L. & CHURILOV, S. 1970. Line structure of generation spectra of lasers with inhomogeneous broadening of the amplification line. JETP Lett, 12, 43-45.

PALDUS, B., HARRIS JR, J., MARTIN, J., XIE, J. & ZARE, R. 1997. Laser diode cavity ring-down spectroscopy using acousto-optic modulator stabilization. Journal of applied physics, 82, 3199-3204.

PEETERS, R., BERDEN, G. & MEIJER, G. 2001. Near-infrared cavity enhanced absorption spectroscopy of hot water and OH in an oven and in flames. Applied Physics B, 73, 65-70.

PETEK, H., NESBITT, D. J., DARWIN, D. C. & MOORE, C. B. 1987a. Visible absorption and magnetic ‐rotation spectroscopy of CH: The analysis of the b B state. The Journal of Chemical Physics, 86, 1172.

PETEK, H., NESBITT, D. J., MOORE, C. B., BIRSS, F. & RAMSAY, D. 1987b. Visible absorption and magnetic ‐rotation spectroscopy of 1CH2: Analysis of the 1A1 state and the 1A1 ‐3B1 coupling. The Journal of Chemical Physics, 86, 1189-1205.

PETERS, N. & WARNATZ, J. 1982. Numerical methods in laminar flame propagation: A GAMM-Workshop, Informatica International, Inc.

POINSOT, T. & VEYNANTE, D. 2001. Theoretical and Numerical Combustion, Edwards.

POPE, C. J. & MILLER, J. A. 2000. Exploring old and new benzene formation pathways in low-pressure premixed flames of aliphatic fuels. Proceedings of the Combustion Institute, 28, 1519-1527.

PRADA, L. & MILLER, J. 1998. Reburning using several hydrocarbon fuels: a kinetic modeling study. Combustion Science and Technology, 132, 225-250.

PRUCKER, S., MEIER, W. & STRICKER, W. 1994. A flat flame burner as calibration source for combustion research: Temperatures and species concentrations of premixed H2/air flames. Review of Scientific Instruments, 65, 2908-2911.

QIN, Z., LISSIANSKI, V. V., YANG, H., GARDINER, W. C., DAVIS, S. G. & WANG, H. 2000. Combustion chemistry of propane: a case study of detailed reaction mechanism optimization. Proceedings of the Combustion Institute, 28, 1663-1669.

RAHINOV, I., FOMIN, A., POLIAK, M. & CHESKIS, S. 2014. Absorption electronic spectrum of gaseous FeO: in situ detection with intracavity laser absorption spectroscopy in a nanoparticle-generating flame reactor. Applied Physics B, 1-7.

RICHTER, H. & HOWARD, J. 2000. Formation of polycyclic aromatic hydrocarbons and their growth to soot—a review of chemical reaction pathways. Progress in Energy and Combustion Science, 26, 565-608.

ROESLER, J., MARTINOT, S., MCENALLY, C., PFEFFERLE, L., DELFAU, J.-L. & VOVELLE, C. 2003. Investigating the role of methane on the growth of aromatic hydrocarbons and soot in fundamental combustion processes. Combustion and Flame, 134, 249-260.

ROMANINI, D., KACHANOV, A., SADEGHI, N. & STOECKEL, F. 1997a. CW cavity ring down spectroscopy. Chemical Physics Letters, 264, 316-322.

ROMANINI, D., KACHANOV, A. & STOECKEL, F. 1997b. Diode laser cavity ring down spectroscopy. Chemical Physics Letters, 270, 538-545.

ROTHE, E. W. & ANDRESEN, P. 1997. Application of tunable excimer lasers to combustion diagnostics: a review. Applied Optics, 36, 3971-4033.

SANTORO, R. J. & SHADDIX, C. R. 2002. Laser-induced incandescence. Applied combustion diagnostics, 252-286.

SAPPEY, A. D., CROSLEY, D. R. & COPELAND, R. A. 1990. Laser-induced fluorescence detection of singlet CH2 in low-pressure methane/oxygen flames. Applied Physics B, 50, 463-472.

SCHADEE, A. 1978. Unique definitions for the band strength and the electronic-vibrational dipole moment of diatomic molecular radiative transitions. Journal of Quantitative Spectroscopy and Radiative Transfer, 19, 451-453.

SCHERER, J. J., PAUL, J. B., OKEEFE, A. & SAYKALLY, R. J. 1997. Cavity ringdown laser absorption spectroscopy: History, development, and application to pulsed molecular beams. Chemical Reviews, 97, 25-51.

SCHERER, J. J. & RAKESTRAW, D. J. 1997. Cavity ringdown laser absorption spectroscopy detection of formyl (HCO) radical in a low pressure name. Chemical Physics Letters, 265, 169-176.

SCHOCKER, A., BROCKHINKE, A., BULTITUDE, K. & EWART, P. 2003. Cavity ring-down measurements in flames using a single-mode tunable laser system. Applied Physics B-Lasers and Optics, 77, 101-108.

SCHOCKER, A., KOHSE-HÖINGHAUS, K. & BROCKHINKE, A. 2005. Quantitative determination of combustion intermediates with cavity ring-down spectroscopy: systematic study in propene flames near the soot-formation limit. Applied Optics, 44, 6660-6672.

SEPMAN, A., VAN ESSEN, V., MOKHOV, A. & LEVINSKY, H. 2003. Cavity ring-down measurements of seeded NO in premixed atmospheric-pressure H2/air and CH4/air flames. Applied Physics B, 77, 109-117.

SERRANO-ANDRES, L., FORSBERG, N. & MALMQVIST, P. A. 1998. Vibronic structure in triatomic molecules: The hydrocarbon flame bands of the formyl radical (HCO). A theoretical study. Journal of Chemical Physics, 108, 7202-7216.

SINGH, J., PATTERSON, R. I., KRAFT, M. & WANG, H. 2006. Numerical simulation and sensitivity analysis of detailed soot particle size distribution in laminar premixed ethylene flames. Combustion and Flame, 145, 117-127.

SMITH, G. P., GOLDEN, D. M., FRENKLACH, M., MORIARTY, N. W., EITENEER, B., GOLDENBERG, M., BOWMAN, C. T., HANSON, R. K., SONG, S. & GARDINER JR, W. C. 1999. GRI-Mech 3.0. URL: http://www. me. berkeley. edu/gri_mech, 51, 55.

SPALDING, D. B. 1956. The theory of flame phenomena with a chain reaction. Philosophical Transactions of the Royal Society of London. Series A, Mathematical and Physical Sciences, 249, 1-25.

STEELE, R. C., MALTE, P. C., NICOL, D. G. & KRAMLICH, J. C. 1995. NO< sub> x</sub> and N< sub> 2</sub> O in lean-premixed jet-stirred flames. Combustion and Flame, 100, 440-449.

THERSSEN, E., BOUVIER, Y., SCHOEMAECKER-MOREAU, C., MERCIER, X., DESGROUX, P., ZISKIND, M. & FOCSA, C. 2007. Determination of the ratio of soot refractive index function E (m) at the two wavelengths 532 and 1064 nm by laser induced incandescence. Applied Physics B, 89, 417-427.

THOMAN, J. W. & MCILROY, A. 2000. Absolute CH Radical Concentrations in Rich Low-Pressure Methane-Oxygen-Argon Flames via Cavity Ringdown Spectroscopy of the A2Δ-X2Π Transition. The Journal of Physical Chemistry A, 104, 4953-4961.

TOLLES, W. M., NIBLER, J., MCDONALD, J. & HARVEY, A. 1977. A review of the theory and application of coherent anti-Stokes Raman spectroscopy (CARS). Applied Spectroscopy, 31, 253-271.

TURNS, S. R. 1995. Understanding NO< sub> x</sub> formation in nonpremixed flames: Experiments and modeling. Progress in Energy and Combustion Science, 21, 361-385.

TURNS, S. R. 1996. An introduction to combustion: concepts and applications, McGraw-Hill.

UCSD Chemical-Kinetic Mechanisms for Combustion Applications. In: PAGE, S. D. M. W. (ed.).

VAIDYA, W. 1934. Spectrum of the Flame of Ethylene. Proceedings of the Royal Society of London. Series A-Mathematical and Physical Sciences, 147, 513-521.

VANMAAREN, A., THUNG, D. S. & DEGOEY, L. P. H. 1994. MEASUREMENT OF FLAME TEMPERATURE AND ADIABATIC BURNING VELOCITY OF METHANE/AIR MIXTURES. Combustion Science and Technology, 96, 327-344.

VEYNANTE, D. & VERVISCH, L. 2002. Turbulent combustion modeling. Progress in Energy and Combustion Science, 28, 193-266.

VINCENTI, W. G. & KRUGER, C. H. 1967. Introduction to physical gas dynamics, Krieger.

VIOLI, A. 2004. Modeling of soot particle inception in aromatic and aliphatic premixed flames. Combustion and Flame, 139, 279-287.

VIOLI, A., D'ANNA, A., D'ALESSIO, A. & SAROFIM, A. F. 2003. Modeling aerosol formation in opposed-flow diffusion flames. Chemosphere, 51, 1047-1054.

VIOLI, A., KUBOTA, A., TRUONG, T., PITZ, W., WESTBROOK, C. & SAROFIM, A. 2002. A fully integrated kinetic monte carlo/molecular dynamics approach for

the simulation of soot precursor growth. Proceedings of the Combustion Institute, 29, 2343-2349.

VIOLI, A., VOTH, G. A. & SAROFIM, A. F. 2005. The relative roles of acetylene and aromatic precursors during soot particle inception. Proceedings of the Combustion Institute, 30, 1343-1351.

WANG, H. 2011. Formation of nascent soot and other condensed-phase materials in flames. Proceedings of the Combustion Institute, 33, 41-67.

WANG, H. & FRENKLACH, M. 1997a. A detailed kinetic modeling study of aromatics formation in laminar premixed acetylene and ethylene flames. Combustion and Flame, 110, 173-221.

WANG, H. & FRENKLACH, M. 1997b. A detailed kinetic modeling study of aromatics formation in laminar premixed acetylene and ethylene flames. Combustion and Flame, 110, 173-221.

WANG, Y., RAJ, A. & CHUNG, S. H. 2013. A PAH growth mechanism and synergistic effect on PAH formation in counterflow diffusion flames. Combustion and Flame, 160, 1667-1676.

WARNATZ, J. 1978a. Calculation of the structure of laminar flat flames I: Flame velocity of freely propagating ozone decomposition flames. Berichte der Bunsengesellschaft für physikalische Chemie, 82, 193-200.

WARNATZ, J. 1978b. Calculation of the Structure of Laminar Flat Flames II: Flame Velocity and Structure of Freely Propagating Hydrogen‐Oxygen and Hydrogen‐Air‐Flames. Berichte der Bunsengesellschaft für physikalische Chemie, 82, 643-649.

WARNATZ, J. 1984. Rate coefficients in the C/H/O system. Combustion chemistry. Springer.

WARNATZ, J., MAAS, U. & DIBBLE, R. W. 2006. Combustion: physical and chemical fundamentals, modeling and simulation, experiments, pollutant formation, Springer.

WESTBROOK, C. K. & DRYER, F. L. 1984. Chemical kinetic modeling of hydrocarbon combustion. Progress in Energy and Combustion Science, 10, 1-57.

WESTBROOK, C. K., DRYER, F. L. & SCHUG, K. P. 1983. Numerical modeling of ethylene oxidation in laminar flames. Combustion and Flame, 52, 299-313.

WILLIAMS, S., ZARE, R. N., RAHN, L. A., PAUL, P. H. & FORSMAN, J. W. 1994. Laser-induced thermal grating effects in flames. Optics Letters, 19, 1681-1683.

WOLFRUM, J. Year. Lasers in combustion: from basic theory to practical devices. In: Symposium (International) on Combustion, 1998. Elsevier, 1-41.

WORKMAN, J. & SPRINGSTEEN, A. 1998. Applied Spectroscopy: A Compact Reference for Practitioners, Elsevier Science.

XIE, J., PALDUS, B., WAHL, E., MARTIN, J., OWANO, T., KRUGER, C., HARRIS, J. & ZARE, R. 1998. Near-infrared cavity ringdown spectroscopy of water vapor in an atmospheric flame. Chemical Physics Letters, 284, 387-395.

YANG, B., LI, Y., WEI, L., HUANG, C., WANG, J., TIAN, Z., YANG, R., SHENG, L., ZHANG, Y. & QI, F. 2007. An experimental study of the premixed benzene/oxygen/argon flame with tunable synchrotron photoionization. Proceedings of the Combustion Institute, 31, 555-563.

YARIV, A. 1967. Quantum electronics, Wiley.

YOUNG, A. T. 1982. Rayleigh scattering. Physics Today, 35, 42-48.

ZALICKI, P. & ZARE, R. N. 1995. CAVITY RING-DOWN SPECTROSCOPY FOR QUANTITATIVE ABSORPTION-MEASUREMENTS. Journal of Chemical Physics, 102, 2708-2717.

ZHU, J., CHOI, M. Y., MULHOLLAND, G. W., MANZELLO, S. L., GRITZO, L. A. & SUO-ANTTILA, J. 2002. Measurement of visible and near-IR optical properties of soot produced from laminar flames. Proceedings of the Combustion Institute, 29, 2367-2374.